Design of a Cone and Plate Co-culture Device to Investigate the Effects of Fluid Shear Stress and Free Fatty Acids on Endothelial Nitric Oxide Production

A Thesis

Submitted to the Faculty

Of

Drexel University

By

Nicholas W. Houriet

In partial fulfillment of the

Requirements for the degree

Master of Science in Biomedical Engineering

June 2016

ACKNOWLEDGEMENTS

I would foremost like to thank Dr. Alisa Morss Clyne for her dedication as an advisor, mentor, and role model throughout my research. I am grateful to her for hiring a mechanical engineer to work in a cell biology laboratory, but even more so for her believing in me and my work. Under her guidance I was able to learn and perform far beyond what I had thought myself capable of.

I had an excellent experience working in the Vascular Kinetics Lab, thanks to the help and support of my fellow lab members Sarah Baseshore, Jason Sedlak, Olivia Ngo, Swathi Swaminathan, Christina Furia, Becky Urbano, Adam Canver, and Mahmoud Hallak. You all helped me every day (and many nights) to understand the intricacies of cell culture, Western blotting, writing, and statistics. And thank you especially for your patience when my machines and lab inventions don't *quite* work the way they were intended. Special thanks as well to the staff and the Drexel University Machine Shop, including Mark Shiber, Scott Eichmann, Nick Catucci, and Richard Carratura for helping me turn my engineering ideas into reality.

Finally, I would like to thank my friends and family for their support throughout my time at Drexel, especially during my research. Thank you all for understanding my unpredictable work hours and your encouragement. A huge thank you to my wonderful parents for working so hard to help me attend Drexel and pursue my dreams. Thank you for your unwavering encouragement and support for all these years.

CONTENTS

LIST OF TABLES

LIST OF FIGURES

Abstract

Design of a Cone and Plate Co-culture Device to Investigate the Effects of Fluid Shear Stress and Free Fatty Acids on Endothelial Nitric Oxide Production

Nicholas Houriet

Alisa Morss Clyne, PhD.

Metabolic syndrome and obesity in particular are significant cardiovascular disease risk factors. Excessive central adipose tissue is strongly linked to insulin resistance, which may contribute to systemic and adipose tissue vascular inflammation. Insulin resistant and obese individuals have increased levels of circulating free fatty acids, which inhibit insulin-induced production of atheroprotective nitric oxide by endothelial cells *in vitro*. Decreased endothelial nitric oxide can further lead to chronic inflammation of the vasculature and adipose tissue. Furthermore, insulin resistant and obese individuals display reduced adipose tissue blood flow. Thus the FFA-induced reduction in endothelial nitric oxide production may further decrease shear stress-induced endothelial nitric oxide production and exacerbate adipose tissue inflammation and metabolic disease.

The objective of this thesis is to elucidate the effects of FFAs on endothelial cell response to fluid shear stress. I hypothesize that shear stress leads to endothelial nitric oxide synthase phosphorylation in the presence of FFAs. If proved true, this would suggest that restoring adipose tissue blood flow may abrogate adipose tissue inflammation and metabolic syndrome.

Since existing *in vitro* fluid shear stress testing devices cannot test the effects of shear stress on endothelial cells in a 3D co-culture system with adipocytes, this thesis first presents a new cone and plate flow device with a 3D hydrogel co-culture component. The cone and plate flow system successfully created laminar fluid shear stress in both acute (5 minute) and chronic

(24 hour) bovine aortic endothelial cells, demonstrated by increased endothelial nitric oxide synthase phosphorylation and cell alignment, respectively. This thesis then presents a method to incorporate a gelatin co-culture component; however the gelatin gel requires further study since it is not adequately flat nor have cells been incorporated. FFAs were demonstrated to inhibit insulin-induced endothelial nitric oxide synthase phosphorylation in static culture. Finally, preliminary data demonstrated that 5 minutes of flow at 20 dynes/cm^2 was able to increase eNOS phosphorylation in samples treated with FFA incubation in 2 of 3 sample groups tested.

This thesis has provided design of a new *in vitro* flow system that could allow testing of co-cultures previously not possible. The results presented here support further examination of the role of shear stress and FFAs in vascular disease. Future work will include the improvement of gelatin molding techniques with finer tolerance features, as well as developing methods to suspend the cells with the gel. Additional experiments should be conducted with FFAs in flow. Furthermore, the cone and plate device offers opportunities for work with other cell types and co-cultures including endothelial, adipocyte, smooth muscle, and macrophages.

Chapter 1: Introduction

1.1 - Clinical relevance: Metabolic syndrome and Obesity

Metabolic syndrome is the name for a cluster of five cardiovascular risk factors: 1) central obesity; 2) elevated triglycerides, 3) diminished high density lipoprotein; 4) systemic hypertension; 5) and elevated fasting glucose (Grundy, Brewer, Cleeman, Smith, & Lenfant, 2004; Mottillo et al., 2010). Metabolic syndrome results in dysfunctions of energy utilization and storage, characterized by chronic low-level "meta-inflammation" of the visceral fat (Scalia, 2013). Individuals with symptoms of metabolic syndrome are 2.9 times as likely to die of coronary heart disease and 3.3 times as likely to die of cardiovascular disease (Lakka et al., 2002).

Central obesity is thought to be a significant factor in metabolic syndrome and insulin resistance. Central obesity is defined as an excessive and unhealthy accumulation of white adipose tissue and visceral fat in the abdomen ("Defining Adult Overweight and Obesity," 2012; Scalia, 2013). Obesity is considered a world-wide epidemic, since prevalence has more than doubled since 1980. According to the World Health Organization, in 2014 there were more than 1.9 billion overweight adults, 600 million of whom were obese. In the United States, more than 33% of adults and 17% of youth are classified as obese (Ogden, Carroll, Kit, & Flegal, 2014). A majority of the world's population live in countries where overweight related deaths outnumber underweight related deaths (Hebebrand & Hinney, 2015). The sharp increase of obesity is attributed to changing lifestyle and diet. In recent years, high-fat processed foods have grown in availability and consumption compared to healthy alternatives (Cutler, Glaeser, & Shapiro, 2003; E. a. Finkelstein & Strombotne, 2010). While obesity is considered a preventable disease that

can be controlled by nutrition and physical activity (E. a. Finkelstein & Strombotne, 2010), the increase in obesity prevalence has a direct impact on healthcare costs. According to a study of inpatient, non-inpatient, and prescription drug spending obese individuals necessitate 41.5% more healthcare costs than non-obese individuals. Furthermore, between 1998 and 2006 there was an 80.4% increase on spending for prescription drugs attributable to obesity and the total medical burden increased from 6.5% to 9.1% of annual medical spending. These costs are attributed to increased prevalence of obesity and not to cost per capita (E. A. Finkelstein, Trogdon, Cohen, & Dietz, 2009).

1.2 - Adipose Tissue and Free fatty acids

Adipose tissue is the body's largest energy storage site and is crucial for providing fuel to the body, especially during periods of fasting. The adipose tissue contains 95% of the stored lipids within the body, and is the primary source of stored energy (Coppack, Jensen, & Miles, 1994; Large, Peroni, Letexier, Ray, & Beylot, 2004). Adipose tissue is comprised of adipocytes, various immune cells, and the microvasculature which delivers blood (Lafontan, 2014). Adipose tissue is classified by the body location, including central (subcutaneous upper abdominal and visceral) and peripheral (hip, gluteal, and femoral) fat. Accumulation of central white adipose tissue has been linked to increased risk of cardiovascular disease, while peripheral fat has been shown to have metabolically protective affects (Manolopoulos, Karpe, & Frayn, 2010).

Free fatty acids (FFAs) are lipids that circulate within the blood plasma and may originate from dietary intake or from mobilization of stored triacylglycerol (TAG) molecules from within the adipose tissue. FFAs are either oxidized as an energy source or re-esterified into TAGs and stored in the adipose tissue. Lipid metabolism, defined as movement of FFA/TAG into and out of the adipose tissue, is tightly controlled by insulin, fatty acids, and adipokines such as leptin, adiponectin, retinol-binding protein 4 and apelin under various conditions of feeding,

fasting, and exercise (Ballard, 1978; Lafontan, 2014). Among the metabolic syndrome risk factors, obesity in particular has been linked to excessive FFA levels (Guenther Boden, 2008).

Excess FFAs cause adipocytes to become pro-inflammatory and release inflammatory cytokines. Specifically, high FFA levels instigate a metabolically induced inflammatory response in adipocytes via the pro-inflammatory receptor Toll Like Receptor 4 (Shi et al., 2006; Song, Kim, Yoon, & Kim, 2006)(Guenther Boden, 2008). This inflammation is marked by increased adipocyte production and release of TNF-α and IL-6. In 3T3-L1 adipocytes, 1-6 hours of 0.3-1.0 mM FFA treatment resulted in increased IKK-β phosphorylation and increased TNF-α secretion (Song et al., 2006). In a separate study of lean and obese mice, TNF-α expression was elevated 5 to 10 fold in the adipose tissue of obese mice compared to healthy subjects, indicating increased pro-inflammatory cytokines in the obese adipose tissue (Hotamisligil, Shargill, & Spiegelman, 1993).

Insulin is a hormone responsible for regulating carbohydrate and fat metabolism as well as managing glucose uptake from the blood stream. In healthy insulin sensitive individuals, insulin also causes vasodilation through nitric oxide production (Steinberg et al., 1997). In a study of 60 obese individuals, insulin resistance was correlated with a two-fold increase in visceral fat, three-fold increase in macrophage infiltration, and 1.5 fold increases in adipocyte size. Additionally, these individuals displayed a threefold increase in resting plasma insulin and twofold increase in circulating FFA, suggesting a link among obesity, adipose tissue inflammation, FFA concentration, and insulin resistance (Klöting et al., 2010). Increased FFAs are attributed to increased adipocyte number and volume, since these adipocytes both secrete excess FFAs and have a reduced ability to clear FFAs from the blood (Guenther Boden, 2008). In another study, insulin resistance was demonstrated by infusing FFAs via lipid emulsions, resulting in reduced glucose uptake in humans for 2 to 4 hours until FFA levels normalized (G Boden, Chen, Ruiz, White, & Rossetti, 1994).

1.3 - Adipose tissue interactions with the microvasculature

The adipose tissue is highly vascularized, and therefore adipocyte and FFA interactions with the microvasculature may play an important role in adipose tissue inflammation and metabolic syndrome (Ballard, 1978; Sotornik et al., 2012). Capillaries and sinusoids consist of an endothelial layer, basal lamina, and pericytes (Alberts, Johnson, & Lewis, 2002). Endothelial cells are particularly important since they act as mediators of vascular homeostasis by controlling permeability, thrombosis, vascular tone, angiogenesis, and inflammation (Michiels, 2003). The endothelium regulates permeability, the exchange of molecules between the blood and tissue, through three types of intercellular connections: tight junctions, adherens junctions, and gap junctions (Dejana, 1996; Schnittler, 1998). The endothelial luminal surface is antithrombotic and anticoagulant, as endothelial cells release agents such as prostacyclin and nitric oxide. Exposing the endothelium to an inflammatory stimulus can create a thrombotic and coagulant state (Pearson, 1999). Vascular tone is regulated through the endothelium derived relaxing factor nitric oxide, a free radical gas which signals vasodilation by relaxation of the vascular smooth muscle tissue (Moncada, Palmer, & Higgs, 1991). Endothelial cells are responsible for angiogenesis during growth, wound healing, and tumor growth. After the degradation of the basement membrane, endothelial cells migrate beyond the blood vessel into the interstitial space where they proliferate and mature into blood vessels (Carmeliet, 2000). Finally, endothelial cells play a role in inflammation by releasing cytokines and displaying adhesion molecules to signal circulating leukocytes, leading to attachment and migration across the endothelial monolayer and into the site of injury or infection (Muller, 2002).

The microvascular endothelium regulates interactions between the blood and the adipose tissue, including nutrient transport to and from the surrounding tissue during

metabolism (Pohl, Ring, Ehehalt, Herrmann, & Stremmel, 2004; Stremmel, Pohl, Ring, & Herrmann, 2001). After a meal, lipids leave the digestive system and are transported via the bloodstream to adipose tissue, where they are stored within adipocytes. To serve as energy, these lipids are mobilized from the adipose tissue and must again pass through the endothelial barrier to be oxidized in the muscles or liver (Ballard, 1978; Kiess et al., 2008). As FFAs are mobilized from or stored in the adipose tissue, they interact with the endothelium to cause an acute immune response characterized by increased endothelial permeability. This inflammatory response, which in normal conditions protects the tissue from penetration by circulating toxins or bacteria, then subsides after FFA transport has ceased (Scalia, 2013). In conditions of excess circulating FFAs as a result of high fat diet and obesity, the normal cycle of acute inflammation is replaced by a chronic inflammatory state (Lafontan, 2014; Scalia, 2013).

Adipose tissue blood flow (ATBF) is dynamically regulated by metabolic factors. ATBF is measured during the pre-prandial (fasting, before meal) and post-prandial (after meal) stages. ATBF increases two to three-fold after non-obese individuals ingest a meal controlled for fat, protein, and carbohydrate content. In 190 measurements of 38 subjects, ATBF was reduced with increasing body mass index, implying that obese subjects display inhibited ATBF compared to non-obese individuals (Summers, Samra, & Frayn, 1999). In a separate study, ATBF was measured using xenon washout in human subjects orally ingesting 75 grams of glucose. Individuals were characterized into distinct groups of responders and non-responders, where responders displayed both high post-prandial ATBF increase and high insulin sensitivity. While this study did not examine obese subjects, it suggests that ATBF is strongly linked to insulin resistance and may be predictive of metabolic syndrome (Karpe et al., 2002; Sotornik et al., 2012). Furthermore, a study comparing healthy individuals to first-degree relatives with known insulin resistance examined ATBF changes after a controlled meal using the xenon washout

method. ATBF was inhibited in insulin resistant subjects 120 minutes after the meal. Additionally, post-prandial circulating FFAs were greater in insulin resistant individuals, suggesting that FFAs may play a role in the mechanisms underlying insulin sensitivity and ATBF. (Dimitriadis et al., 2007; Jansson, Larsson, & Lönnroth, 1998; Steinberg et al., 1997).

1.4 - Nitric Oxide Production in Endothelial Cells

Endothelial cells produce nitric oxide (NO) in response to fluid shear stress from blood flow (Kabirian, Amoabediny, Haghighipour, Salehi-Nik, & Zandieh-Doulabi, 2014; Noris et al., 1995). Endothelial NO causes vasodilation, increased blood flow, lowered blood pressure, inhibition of platelet/leukocyte adhesion, and reduced smooth muscle cell proliferation (Albrecht, Stegeman, Heeringa, Henning, & van Goor, 2003; Ignarro, Buga, Wood, Byrns, & Chaudhuri, 1987; Moncada et al., 1991; Palmer, Ferrige, & Moncada, 1987). Inhibition of endothelial NO synthesis presents a significant risk factor for atherosclerosis and metabolic syndrome (Moncada et al., 1991; Scalia, 2013; Sotornik et al., 2012).

Endothelial cells in humans are subjected to shear stress due to viscous fluid friction from blood flow on the luminal surface, which manifests as a shear stress of 5-40 dynes/cm^2 in uniform regions, but may include transient values of 0 to 100 dynes/cm^2 as a result of pulsatile flow (Davies, 2015). This force is transmitted via the cytoskeleton to specific sites within the cell where the force is converted into chemical signals in a process known as mechanotransduction (Davies, 2015). Several mechanisms and pathways have been proposed to describe mechanotransduction due to fluid shear stress including: ion channels, growth factor receptors, G proteins, caveolae, adhesion proteins, the cytoskeleton, the glycocalyx, and the primary cilia (J. Ando & Yamamoto, 2009). Within one minute after applied flow, endothelial cells exhibit

potassium ion channel activation, intracellular calcium increase, and cGMP increase coinciding with the endothelial NO production (Davies, 2015; Kemeny, Figueroa, & Clyne, 2013). Ca^{2+} permeable channels are known to open in response to shear stress, causing a dose dependent influx of Ca^{2+} through the cell membrane (T. Ando, Komatsuda, & Kamiya, 2016). Tyrosine kinase receptor VEGFR2 is activated by fluid shear stress in ECs. VEGFR2 interacts with VE-cadherin and PECAM-1 at the adherens junction to transduce shear stress signals (Osawa, Masuda, Kusano, & Fujiwara, 2002; Shay-Salit et al., 2002; Tzima et al., 2005). VEGFR2 activates intracellular signals via phosphatidylinositol 3-kinase (PI3K), leading to Akt phosphorylation, endothelial nitric oxide synthase (eNOS) phosphorylation, and ultimately NO production (Dimmeler et al., 1999; Kemeny et al., 2013).

Excess FFAs inhibit the endothelial cells' ability to produce atheroprotective NO (Guenther Boden, 2008; Klöting et al., 2010; Scalia, 2013). In an *in vivo* study of the effects of FFA on vasodilation, subjects were given the endothelium-dependent vasodilator methacholine chloride, or the endothelium-independent vasodilator nitroprusside. Additional subjects were given somatostatin to induce insulinopenia similar to that found in insulin resistance, a condition commonly found in patients with metabolic syndrome. Subjects were then given emulsions of Intralipid, an FFA, to increase plasma FFA concentrations 3 to 9 times greater than their basal value. Leg blood flow measurements were then taken to quantify vessel dilation during a 2 hour treatment. Individuals with elevated FFA levels displayed ~20% lower blood flow than the control group in response to methacholine chloride, indicating that FFAs impair endothelium-dependent vasodilation and reduce blood flow. Elevated FFAs did not impair endothelium-independent vasodilation via nitroprusside. Additionally, patients with induced insulinopenia saw a two-fold increase in circulating FFAs without Intralipid emulsion and also experienced a ~20% reduction in endothelium-dependent vasodilation via methacholine chloride. This study

suggests that elevated circulating FFAs impair vasodilation, and therefore flow (Steinberg et al., 1997). Furthermore, *in vitro* effects of FFAs on bovine aortic endothelial cells (BAEC) were demonstrated in static culture. Three hour incubation with 100 µmol/L palmitic acid followed by 5 minute insulin stimulation resulted in a decreased insulin mediated phosphorylation of IRS-1, Akt, and eNOS compared to control samples with no FFA exposure. In control samples, 100 µmol/L insulin resulted in a 3 fold increase in NO production, while FFA pretreatment caused a 90% reduction of this value (Kim et al., 2005).

The effect of FFAs on endothelial cell NO production in response to shear stress has not yet been studied *in vitro,* nor have flow-mediated interactions between endothelial cells and adipocytes. Increased post-prandial blood flow could increase shear stress induced NO production and may help restore adipocyte and endothelial function during periods of elevated FFAs, thereby decreasing the chronic endothelial and adipose inflammation prevalent in metabolic syndrome.

1.5 - Existing *in vitro* Vascular Flow Devices

Devices for applying fluid shear stress (FSS) to cells have been used since the 1970s to create controlled flow conditions for endothelial layers (Davis et al., 2015). Several variants are used, including the parallel plate flow chamber, the microfluidic device, and cone and plate devices (Blackman, Barbee, & Thibault, 2000). All of these methods allow control of fluid viscosity, flow rate, and channel geometry to create the desired shear stress profile over the cell layer.

Parallel Plate Flow Chamber:

The parallel plate flow chamber (PPFC) uses cells seeded onto a rectangular glass slide, which is then subjected to pressure-driven or gravity driven flow (Davis et al., 2015). The small gap height between the cells and the top plate creates a laminar flow regime which can be controlled by manipulating the fluid properties or chamber geometry. Equation 1 describes the shear stress created on the top and bottom planes of the chamber. *Q* represents the volumetric flow rate, μ represents the fluid dynamic viscosity, *w* is the channel width, and *h* is the channel height. Increasing the flow rate or fluid viscosity will increase the FSS, as will decreasing the channel dimensions (Munson, Okiishi, Huebsch, & Rothmayer, 2013).

Equation 1: Fluid shear stress of parallel plate flow chamber

$$\tau = \frac{6\mu Q}{wh^2}$$

Figure 1 displays the basic parallel plate flow theory, where fluid is pumped between two plates shown at the top and bottom. The fluid friction against the channel walls or cells exerts a shear stress. The fluid velocity is shown as the first arrow profile in Figure 1, creating a parabolic distribution. The velocity is greatest at the channel center and reduces toward the edges as a result of friction. At the wall, the fluid reaches zero velocity as a result of the no-slip condition. The second arrow profile in Figure 1 shows the shear stress profile exerted on the cells by the fluid.

Figure 1: Pressure driven flow for parallel plate flow theory

The PPFC is well suited for mono-cultures in which a single cell type is tested. Shear stress can be controlled through the manipulation of the gap height, even allowing multiple heights within one chamber, as seen in a stepped geometry (Galie, van Oosten, Chen, & Janmey, 2015). Due to the laminar, unidirectional flow created in the chamber, this design is effective for quantifying cell alignment in both steady and reversing flow (Wang, Lu, & Schwartz, 2012). The advantages of this device include the high level of control and repeatability, as well as the ability to easily image the sample on a microscope stage. Furthermore, PPFC are commercially available, with well characterized flow regimes (Davis et al., 2015). Limitations of this system include the necessary pump and large volume of media to operate. Furthermore, the setup and use of the PPFC is complicated by the need for vacuum sealing and bubble traps, making it impractical for acute studies and high-throughput applications. While capable of steady, pulsatile, and reversing flows by use of a pump, the PPFC is not an effective platform for creating disturbed flow over cell areas large enough for protein quantification.

The PPFC has been used for co-cultures with endothelial and smooth muscle cells in the study of arterial stiffening (Scott-Drechsel et al., 2012; Ziegler, Alexander, & Nerem, 1995). This method used a synthetic membrane to separate the smooth muscle cell chamber from the endothelial cells which were subjected to flow in a PPFC. While this setup does allow interactions between the cell types, it is not a true model of interaction because the cells are separated by a membrane. PPFCs have also been adapted to include a 3D co-culture

component, such as a type I collagen matrix with smooth muscle cells combined with an endothelial monolayer (Ziegler et al., 1995). However, this method requires a complicated procedure of molding separate collagen gels for co-culture, then transferring them into a custom PPFC device.

Microfluidic Device:

This category includes a range of microfluidic devices that use a small 100-500 µm scale channel. These channels are typically square or rectangular due to the microfabrication methods used. Like the parallel plate device, the narrow gap creates laminar flow. In mono-culture, these devices can create channels as small at 100 µm to simulate capillaries (Bhatia & Ingber, 2014). Use of flexible polymer construction can even allow cyclic stretch to be applied and substrate stiffness to be varied, both of which are important factors in endothelial mechanobiology (Zheng et al., 2012). This device most closely mimics the size of small blood vessels and uses a small fluid volume to operate. However, the drawbacks include the small surface area for cell culture, which limits the use of protein quantification methods such as Western blot, as well as complicated fabrication and cell seeding processes.

Microfluidic channels have been used to study interactions between endothelial layers and leukocyte adhesion, rolling, and migration by creating flow chambers in parallel with a tissue compartment separated by a synthetic membrane (Lamberti et al., 2014). Co-culture can be achieved by lining the microchannel with an endothelial monolayer and culturing a second cell type in the surrounding tissue space, as demonstrated in blood-brain barrier models, using a membrane similar to the one discussed earlier in the PPFC (Prabhakarpandian et al., 2013). However, microfluidic channels have limited 3D co-culture options, unless a cell-compatible hydrogel is used rather than the more typical polydimethysiloxane (PDMS).

Cone and Plate Device:

A rotating cone can be used to create a constant shear stress over a circular surface. Unlike the PPFC and microfluidic systems, this flow is not pressure driven. The rotating cone creates a form of Couette flow, where the cone creates a sliding surface which moves the fluid through frictional forces (Munson et al., 2013). The angled cone geometry allows the shear stress to remain constant across the surface. When a flat disk is used rather than a cone, the disk tangential velocity increases as a function of the radius, yielding a linear velocity gradient with increasing disk radius (Figure 2, left). This phenomenon can be compensated for by introducing a tapered cone geometry that reduces distance between the cone surface and the cells at the device center (Malek, Ahlquist, Gibbons, Dzau, & Izumo, 1995). This can create the desired near-uniform velocity profile (Figure 2, right), mimicking the desired flow chamber conditions. This design is further illustrated in Figure 3, which depicts the fluid velocity (left) and shear stress (right) of a rotating cone above a substrate.

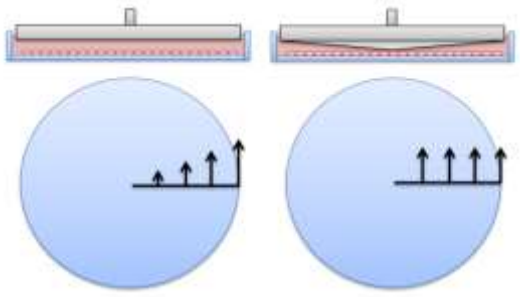

Figure 2: Fluid Velocity Gradient of Disk (left) and Cone (right) and Plate Devices, showing flow velocity can be consistent with use of cone geometry

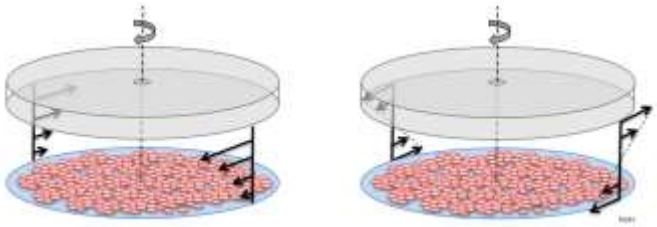

Figure 3: Fluid (left) Velocity and Shear (right) Gradients for the Cone and Plate in the vertical direction

Fluid shear stress is calculated from Equation 2, where μ is the fluid dynamic viscosity, ω is the cone angular velocity, and α is the angle between the cone surface and the substrate (for more details see section 2.5.2 - Fluid Mechanics).

Equation 2: Fluid shear stress of cone and plate device

$$\tau = \frac{\mu\omega}{\alpha}$$

Current designs use a glass or plastic plate seeded with an endothelial monolayer and a steel or Teflon cone. These designs provide both a uniform surface for cell attachment and consistent distance between the cone and cell layer (Davis et al., 2015). Since the flow is not pressure driven, the cone and plate device can provide a better model for isolating and studying the effects of shear stress in the absence of altered pressure (Davis et al., 2015).

Co-culture has been explored in cone and plate devices, however it has been limited to use of a Transwell membrane to separate an endothelial monolayer from a smooth muscle cell culture region, as proposed in a patent by Blackman and Wamhoff (Blackman & Wamhoff, 2014). A 3D hydrogel co-culture has not been explored in a cone and plate device, likely due to the difficulties in positioning the cone in relation to the varied surface of the co-culture.

1.6 - Existing methods of Adipocyte-Endothelial Co-culture

In vitro co-culture models involve seeding adipocytes and endothelial cells on scaffolds or permeable membranes for testing in a static environment. 3D mono-culture and co-culture models have been studied using fibronectin-silk scaffolds for the study of lipogenesis, lipolysis, and hyperinsulinemia in the presence of both endothelial and adipose cells. Endothelial cells in co-culture increased adipocyte triglyceride accumulation and decreased lipolysis in response to increased insulin, indicating that a co-culture can increase the physiological relevance of an *in vitro* model (Choi, Bellas, Gimble, Vunjak-Novakovic, & Kaplan, 2011; Choi, Gimble, Vunjak-Novakovic, & Kaplan, 2010). Additionally, adipocyte co-culture with macrophages has been used to study the adipose tissue inflammatory response. Macrophages and adipocytes were cultured under two conditions: in direct contact and across a trans-well membrane. Overall inflammatory adipokine expression was increased in both direct and Transwell co-culture models compared to adipocyte only controls, indicating a pro-inflammatory cross-talk between the cells. Furthermore, secreted IL-10 was only elevated in direct contact co-cultures while TNF-α was only elevated in Transwell co-cultures, indicating that the co-culture method impacts cell response (De Boer, Monk, & Robinson, 2014). These methods allowed repeatable co-culture observations but lacked physiological relevance. Specifically, the methods did not simulate the effect of flow across the endothelial cell layer and how this flow would affect endothelial cell – adipocyte interactions. My goal was therefore to create a 3D co-culture flow model of endothelial cells and adipocytes to study interactions under physiological flow conditions.

1.8 - Thesis Goal

Metabolic syndrome is linked with decreased pre- and post-prandial adipose tissue blood flow, especially in patients with insulin resistance and obesity (Goossens, 2008; Sotornik

et al., 2012; Summers et al., 1999). Reduced adipose tissue blood flow may exacerbate endothelial dysfunction in the presence of elevated circulating FFAs (Karpe et al., 2002; Toda & Okamura, 2013), reducing endothelial NO production and contributing to a sustained chronic inflammatory state (Albrecht et al., 2003; Noris et al., 1995; Scalia, 2013; Sotornik et al., 2012). FFAs inhibit endothelial NO production in response to insulin in *in vitro* static culture (Kim et al., 2005). **I hypothesize that shear stress-induced NO production is maintained in the presence of FFAs, and that this could reduce adipocyte inflammation in a co-culture model.** To investigate this hypothesis, I completed the following aims:

Aim 1: Design and validate a cone and plate apparatus to apply shear stress to endothelial cells in 3D hydrogel co-culture. A need exists for an improved co-culture platform allowing 1) control of laminar fluid shear stress applied to endothelial cells, 2) a 3D hydrogel in which a second cell type can be co-cultured, 3) simultaneous triplicate samples, and 4) sufficient cell yield for protein quantification. This system will enable study of endothelial cell interactions with the surrounding tissue under flow conditions. This device will also allow analysis of phosphorylated eNOS by Western blot, a crucial measurement in determining endothelial response to flow.

Aim 2: Quantify the effects of changes in shear stress on eNOS phosphorylation in the presence of FFAs. Decreased adipose blood flow in patients with visceral obesity may exacerbate the detrimental effects of FFAs on endothelial cells. FFAs have been shown to reduce eNOS phosphorylation in response to insulin in static culture *in vitro.* We will determine if shear stress increases eNOS phosphorylation in the presence of FFAs.

The *in vitro* cone and plate device produced during this project can be used to study the interactions of endothelial and adipose tissue cells under physiological flow conditions. This system can be adapted to other cell and tissue types, as well as greater ranges and waveforms

of shear stress. The cone and plate device will increase the capabilities of researchers to examine the effects of shear stress on endothelial cell interactions with parenchymal tissue, allowing more physiologically relevant experiments than previously possible. This research also contributes to our understanding of the role of adipose tissue blood flow in metabolic syndrome. Correcting the decrease in adipose tissue blood flow may be an effective measure to counteract endothelial and adipocyte inflammation and reduce the inflammatory interactions in the adipose tissue.

1.9 – Thesis Organization

Chapter 2: This chapter describes the cone and plate device fluid mechanics analysis, as it related to the design specifications. The design justifications and details of the prototype device are explained, followed by the live cell validation testing. Next, the final device design is explained along with details of the improvements over the prototype. This chapter also describes the live cell tests, which both validated the device and served as preliminary data for the FFA experiments.

Chapter 3: This chapter describes the design and development of a hydrogel co-culture system, which completes the first aim and design portion of the thesis.

Chapter 4: This chapter presents the experimental methods and results for eNOS phosphorylation in the presence of FFAs.

Chapter 2: Design and Validation of Cone and Plate Flow Device with 3D Co-culture

2.1 – Introduction

The study of flow induced effects on endothelial health is crucial for understanding mechanisms of cardiovascular function in health and disease. Endothelial cells line the lumen of blood vessels and respond to fluid shear stress induced by laminar blood flow by producing nitric oxide (NO), a vasodilator which acts as a protective agent against vascular diseases (Ignarro et al., 1987; Moncada et al., 1991; Pearson, 1999). Flow-induced NO is required to maintain endothelial health, and a deficiency in NO production presents a significant risk factor for atherosclerosis and metabolic syndrome (Moncada et al., 1991; Scalia, 2013; Sotornik et al., 2012).

Several *in vitro* flow systems have been developed to subject endothelial cell monolayers to controlled fluid shear stress similar to that found in blood vessels. The most commonly used flow systems include parallel plate flow chambers (PPFC), microfluidic flow devices (MFD), and cone and plate flow devices (CPFD) (Davis et al., 2015). Each flow system offers advantages and disadvantages, and the system must be selected with capabilities matching the intended application. PPFC are commercially available, with well characterized flow regimes. The shear stress calculations are simple and linearly relate volumetric flow rate to FSS (Munson et al., 2013). MFD systems create FSS using channel dimensions and geometry that simulate the microvasculature, as well as physiologically relevant time scales (Zervantonakis, Kothapalli, Chung, Sudo, & Kamm, 2011). While MFD systems use small amounts of reagents, they face limitations due the small number of cells that can be cultured in a device. CPFD systems offer similar advantages to PPFD such as well-controlled flow regime and large cell culture area, though have limitations for long term use due to small media volumes (Davis et al., 2015).

While studying a single cell type, such as an endothelial cell, *in vitro* allows isolation of the cells' activity, this simplified system has limited physiological relevance. In the human vasculature, endothelial cells interact with numerous other cell types such as smooth muscle cells, macrophages, and parenchymal tissue cells such as adipocytes (Michiels, 2003). Previously, endothelial cells were combined with other cell types in a co-culture using hydrogel spheres, hydrogel layers, scaffolds, and synthetic permeable membranes (Dahlin, Gershovich, Kasper, & Mikos, 2014; Hagyoung & Choi, 2009; Scott-Drechsel et al., 2012; Yao, Zhang, Lin, & Luan, 2013; Ziegler et al., 1995). These co-culture systems allow endothelial cells to directly interact with other cell types in a structure similar to that encountered *in vivo.* In particular, the use of three-dimensional (3D) co-culture can partially replicate a tissue structure. For example, an endothelial monolayer can be co-cultured on another cell type (ie. smooth muscle cells) embedded in a collagen scaffold to simulate the arterial wall (Ziegler et al., 1995).

Most studies of endothelial cell NO production in response to flow have been performed in monoculture. However, in many cases, interactions among multiple cell types may be important for endothelial cell response to flow. The aforementioned flow systems have been used in limited cases to study endothelial cell co-cultures. A PPFC was adapted to include a 3D co-culture component using a molded layer of type I collagen seeded with smooth muscle cells (Ziegler et al., 1995). MFD systems also were created with a co-culture component in the form of separate flow chambers separated by permeable membrane, such as the use of a MFD with parallel channels linked by microscale permeations for the study of blood-brain barriers (Prabhakarpandian et al., 2013). Finally, co-cultures were achieved in CPFD systems using Transwell membranes to separate endothelial cells from smooth muscle cells; however a 3D co-culture using a hydrogel has not been reported (K. R. Chung & Dai, 2013).

Currently, no *in vitro* flow system exists which permits high-throughput testing of endothelial cells cultured on a 3D cell-laden hydrogel under controlled shear stress while providing sufficient cell yield for protein quantification assays such as Western blot. Therefore, the goal of this project was to create a device capable of: 1) applying controlled laminar fluid shear stress on endothelial cells cultured on 2) a 3D cell-laden hydrogel. The device should enable 3) triplicate samples with 4) sufficient cell yield for protein quantification. The unique capabilities of this system will simulate the microvasculature and surrounding parenchymal tissue, allowing examination of interactions among blood flow, the endothelium, and the underlying tissue without compromising control over FSS. The following chapter will explain the design, fabrication, and validation of a CPFD system including a prototype device for proof of concept and a final system capable of simultaneous testing of triplicate samples.

2.2 - Problem Statement

An *in vitro* flow device is needed which is capable of subjecting endothelial cells to 1) controlled laminar fluid shear stress while cultured on 2) a 3D cell-laden hydrogel with 3) triplicate samples and 4) sufficient cell yield for protein quantification by Western blot.

2.3 - Concept Generation and Selection

The cone and plate design was selected based upon a survey of existing flow platforms, which were grouped into three main categories: parallel plate flow chamber, microfluidic device, and cone and plate. The selection matrix in Table 1 displays the relative capabilities of each platform compared across 7 criteria deemed critical to the project goals.

The criteria were selected based upon the total system effectiveness before, during, and after testing. *Acute* and *Chronic* testing describes flow for 0 to 30 minutes and 1 to 24 hours, respectively. *Laminar shear stress* refers to the ability to create a controlled, steady,

unidirectional fluid shear stress across the cell surface. *Throughput* is the number of samples that can be tested at the same time, as well as the relative ease of quantifying data. The *Co-culture System* criteria refers to the ability to include a 3D cell-laden hydrogel in the device. *Cell Surface Area* refers to the relative amount of cells that are available for imaging and protein quantification. *Ease of Use* includes the time, difficulty, and resources required to assemble, operate, disassemble, and clean the device. *Versatility* refers to the ability of the system parameters to be adapted for alternate flow regimes, including changes in shear stress magnitude or waveform.

Table 1: Selection matrix of flow system capabilities

	Parallel Plate Flow Chamber	**Microfluidic Flow Device**	**Cone and Plate Flow Device**
Acute Testing	●	●	●●●
Chronic Testing	●●●	●●●	●
Laminar FSS	●●●	●●●	●●●
3D Co-Culture	●●	●●	●●●
Sample Throughput	●●	●	●●●
Cell Surface Area	●●	●	●●●
Ease of Use	●	●●	●●●
Versatility	●	●	●●●

The parallel plate flow chamber (PPFC) scored highly for *Chronic Testing* as it provides a platform with ample cell culture media and can be contained within a cell culture incubator, allowing experiments lasting hours to days (Davis et al., 2015). However, this platform received

a lower score for *Acute Testing* due to the complexity of sample setup and removal, making time points below 30 minutes cumbersome. The PPFC also performs well for creating *Laminar Shear Stress* across the entire cell surface, as the fluid mechanics are well established and validated (Munson et al., 2013). The PPFC suffers in *Throughput* due to the complicated setup which requires vacuum suction, peristaltic pump, bubble traps, and media reservoirs for each sample tested. Samples also require seeding onto specific glass slides and a relatively high media volume (~50 mL) to fill the tubing loop. These support systems limit the number of samples that can be run simultaneously, as well as provide challenges for the *Ease of Use*. The PPFC also lacks the ability to easily incorporate a *Co-culture System*, as this would require a custom designed chamber that can accommodate a hydrogel layer without interfering with the vacuum sealing. While this has been validated in previous work, it is a complicated procedure and requires specialized modifications (Ziegler et al., 1995). The *Cell Surface Area* of the PPFC is limited by the size of the flow chamber wall and gasket, yielding up to 8 cm^2 of cell culture area (Davis et al., 2015). Shear stress manipulation can be achieved by changing the flow velocity, viscosity, or pressure, and reversing flow can be achieved using a peristaltic pump. However, the PPFC lacks *Versatility* as it cannot create recirculating flow waveforms as observed in flow eddies existing in the vasculature. Overall, the PPFC is a robust system for low-throughput laminar flow testing, but lacks versatility, throughput, and cell area yield to serve as an appropriate for platform.

The microfluidic device (MFD) scored well for *Chronic Testing*, as cells can be kept alive for extended periods within a cell culture incubator and provided with fresh media. However, *Acute Testing* can be unrealistic due to the resources required to build new devices for each experiment. This drawback is the primary reason limiting the system *Throughput*, along with the time required to seed and grow cell layers within microfluidic channels. The MFD performs well for creating *Laminar Shear Stress* across cells, as the known chamber size and flow rate can be

used to calculate the shear stress (Davis et al., 2015). MFD *Ease of Use* is low, as devices cannot be cleaned and reused. Combined with the need for a syringe pump and tubing, the setup is limiting for both *Throughput* and *Ease of Use. Co-culture Systems* can be incorporated into MFD devices using permeable membranes between channels and can provide a realistic approximation of a capillary vessel within a tissue (Prabhakarpandian et al., 2013). However, the *Versatility* of the MFC is limited to changes in flow rate from the pump and the complexity of channel geometries that can be fabricated. Furthermore, the *Cell Culture Area* is extremely limited due to the small channel size, making protein quantification techniques such as Western blot nearly impossible.

The cone and plate flow device (CPFD) provides the most advantages compared to the alternatives. The device can be used within a cell incubator to allow *chronic* testing of samples up to 24 hours, while the ability to remove samples quickly allows *acute* testing down to 1 minute of flow time, a crucial feature for this application. The low angled cone has been shown to create constant *Laminar Shear Stress* on the monolayer surface and has been well validated (Davis et al., 2015). Sample *Throughput* is greater for the CPFD compared to the PPFC and MFD because the device does not require tubing, pumps, or media reservoirs which can limit the number of simultaneous samples. The self-contained CPFD saves space within the incubator, allowing more devices to fit and operate simultaneously. This design further improves the *Ease of Use* of the system, which is high compared to the PPFC and MFD as the system does not require assembly or teardown of the aforementioned tubing components. The CPFD provides superior *versatility* due to the computer controlled cone rotation. Laminar, pulsatile, and reversing flow can be achieved with changes in motor programming, requiring no mechanical or geometric changes to the device. Furthermore, these programs can implement changes in flow during a testing cycle if desired. Crucially, the CPFD enables inclusion of a 3D *Co-culture System*.

While existing devices have yet to accomplish this feat, the CPFD has significant potential to combine a 3D co-culture with the other advantages previously described to create an easy to use, effective, and comprehensive flow system.

2.4 - Design Goals and Specifications

The design objective is to create a flow system capable of subjecting an endothelial monolayer seeded on a 3D cell-laden hydrogel with controlled fluid flow. The system should be simple to operate by a trained researcher and capable of higher throughput than existing devices. From these general goals, a list of design specifications was created and is shown in Table 2. This table outlines the specifications that must be achieved *in combination with a 3D co-culture.*

Table 2: Design Needs and Specifications

#	Need:	Specification:
1	Laminar flow to create FSS on endothelial monolayer	Modified Reynolds number < 1
2	Physiological range of FSS	1 to 40 dynes/cm^2
3	Control of Cone-Plate gap distance	+/- 5.0 µm
4	Uniform FSS to monolayer	> 80% cell area at target FSS
5	Yield sufficient cells for protein quantification	15 cm^2 cell flow area
6	Maintain cells at physiological conditions	37^{o}C, 5% CO_2, 80% humidity
7	Allow visualization of cells and flow	Optically clear bottom
8	Sample Throughput	Minimum 2 samples simultaneously

Primarily, the device must create steady, uniform laminar flow over the monolayer at shear stress levels found in the vasculature. The modified Reynolds number for a cone and plate flow device is a parameter experimentally established to describe rotational Couette flow (Munson et al., 2013). At values of $Re^* < 1$ the flow between the cone and plate is dominantly tangential, creating a highly uniform laminar flow. At $1 < Re^* < 4$, the flow experiences transition as centrifugal flow emerges in the radial direction. At values $Re^* > 4$, a turbulent regime appears (M. H. Buschmann, Dieterich, Adams, & Schnittler, 2005). The magnitude of shear stress exerted on the cell monolayer must range from 1 to 40 dynes/cm^2 to encompass both pathologically low, healthy, and high blood flow. The gap between the cone surface and endothelial monolayer must be controlled to within +/- 5.0 µm to preserve the desired shear stress. The sample throughput must meet or exceed 2 samples simultaneously to allow biological duplicates in similar testing conditions and reduce overall testing time. The uniform shear stress must be maintained for at least 80% of the cell surface area to allow enough cells to be exposed to flow. The device must provide sufficient surface area to culture endothelial cells for Western blot protein analysis, which is defined as a minimum 28 cm^2. The device must maintain samples at physiological conditions within a cell culture incubator at 37°C, 5% CO_2 and 80% humidity with full operational capabilities. Lastly, the device bottom must be clear or exposed to allow a microscope to focus on the cell layer to allow visual characterization of the flow regime and cell imaging.

2.5 – Development of Prototype Cone & Plate Flow Device

2.5.1 - Prototype Cone & Plate Flow Systems Overview

The prototype design was separated into 4 sub-systems: 1) Cone Geometry, 2) Cone-Plate Gap Control 3) Electrical and Motor, 4) Programming and Control. The proposed device overall layout with all systems is shown in Figure 4. The *cone geometry* sub-system includes fluid mechanics and geometry design to achieve the uniform laminar shear stress specifications, as well as the design of bearings to mount the cone. The *cone-plate gap* control sub-system includes the ability to detect and accurately position the cone relative to the substrate, whether it be a hydrogel co-culture layer or a culture dish. The *electrical and motor* subsystem involves the motor, power supply, and power transmission to the cone. The *programming and control* subsystem is concerned with the electrical systems control, as well as the integration and operation of all components. The following sections describe the design and fabrication of all parts of the prototype device, as well as validation of the aforementioned design specifications.

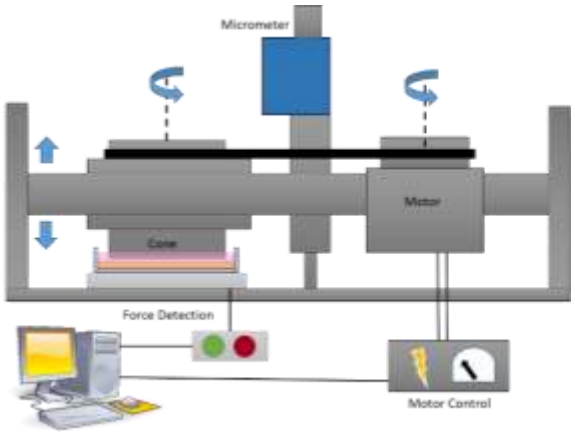

Figure 4: Overview of Prototype Cone and Plate Flow Device

2.5.2 - Fluid Mechanics

Cone and Plate flow mechanics are characterized as a form of sliding surface Couette flow where the top surface (cone) rotates and drags the underlying fluid along as a result of fluid friction (Munson et al., 2013). The desired FSS and modified Reynolds number (Re*) are the two primary parameters for the cone design (M. H. Buschmann et al., 2005; Matthias H. Buschmann, 2002; Malek et al., 1995). The modified Reynolds number characterizes the flow as a ratio of centrifugal to viscous forces and indicates the onset of laminar, transitional, and turbulent flow. Laminar flow is achieved when all flow moves tangentially to the rotating cone. Turbulent flow begins at the onset of radial flow, moving fluid from the cone center to the perimeter (Matthias H. Buschmann, 2002). At values of Re* < 1 the flow between the cone and plate is dominantly tangential and follows the cone rotation, creating a laminar flow regime. This "creeping" Couette flow is desired to create uniform laminar flow comparable to that found in the microvasculature. At 1 < Re* < 4, the flow experiences transition as centrifugal flow emerges in the radial direction. At values Re* > 4, a turbulent regime appears. Equation 3 describes the modified Reynolds number, where *r* is the radial position, α is the cone angle, ω is the angular velocity, and *v* is the fluid kinematic viscosity. It is important to note that modified Reynolds number is a local variable, meaning that multiple flow regimes can exist within the same system (M. H. Buschmann et al., 2005).

Equation 3: Modified Reynolds number for Couette flow

$$Re^* = \frac{r^2 \alpha^2 \omega}{12v}$$

The equation for FSS for Couette flow with a small angle approximation is given by Equation 4 where τ is the FSS at the substrate surface, μ is the fluid dynamic viscosity, ω is the cone angular velocity, and α is the angle between the cone and substrate. For small cone angle

values, the small angle approximation *sin(α) = z/r = α* where *z* is the gap distance between the cone and substrate, *r* is the radius of the cone, and α is the cone angle of less than 1.5°.

Equation 4: Couette flow tangential fluid shear stress with small angle approximation

$$\tau = \mu \frac{dv_\theta}{dz} = \mu \frac{v_\theta}{z} = \frac{\mu \omega r}{z} = \frac{\mu \omega}{\alpha}$$

To explore cone geometry design options, preliminary calculations were performed to visualize the effects of changing cone parameters. The shear stress was calculated and plotted as a function of cone angle and angular velocity using MATLAB (Figure 5). The horizontal dotted line indicates the target maximum shear stress of 40 dynes/cm^2. To reach this shear stress, either a cone angle of approximately 0.7° or a velocity greater than 8.33 RPS is required. Alternatively, the fluid viscosity could be increased to increase shear stress for a given cone angle and speed.

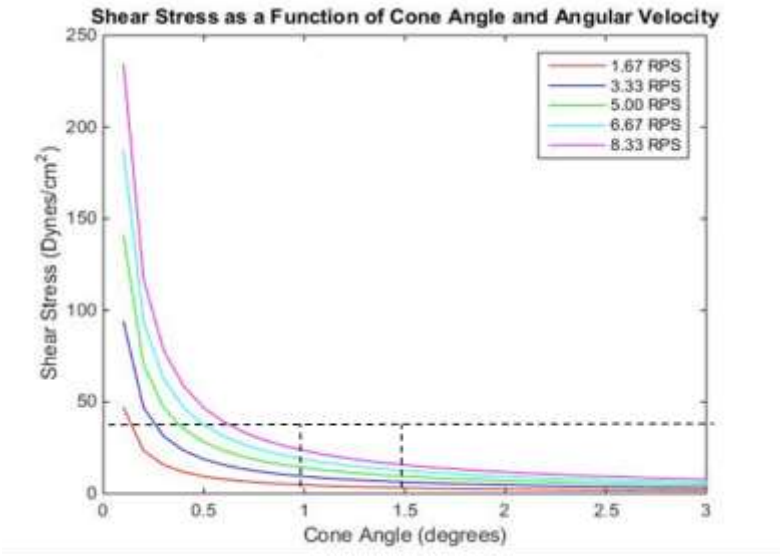

Figure 5: Shear stress as function of cone angle and angular velocity

Figure 6 shows the modified Reynolds number as a function of cone angle for multiple cone speeds. The modified Reynolds number increases exponentially with cone radius and angle and linearly with angular velocity. The modified Reynolds number is inversely proportional to the fluid viscosity. The horizontal dashed line represents the upper target limit of the modified Reynolds number (4), which is below the onset of turbulent flow. Speeds up to 8.33 RPS can accommodate a cone angle of up to 1.5° while remaining below the turbulent threshold.

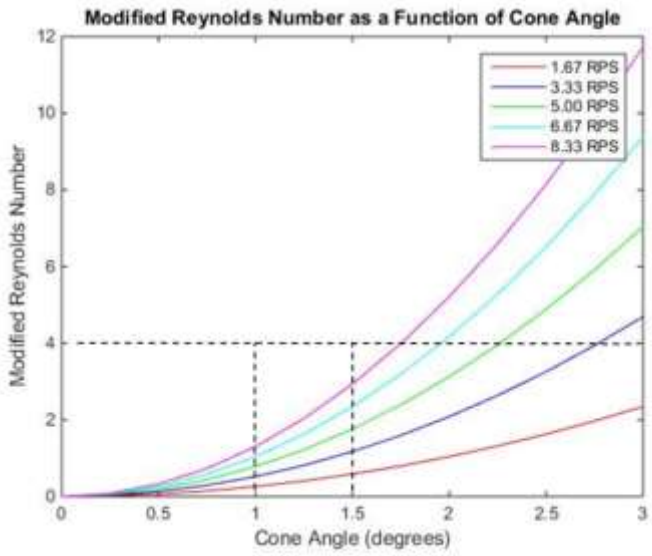

Figure 6: Modified Reynold Number as function of cone angle

From this analysis, it is clear that to maintain a low modified Reynolds number the values to be minimized are the cone radius, cone angle, and cone angular velocity. Additionally, increasing fluid viscosity will increase shear stress at a given radius, angle, and speed while simultaneously reducing turbulent effects. Specific effects and practical limitations of each variable are as follows:

Cone Radius: the cone radius is exponentially related to the modified Reynolds number and should be minimized to ensure laminar flow. The radius limitation is the specification for

endothelial cell surface area, which requires a minimum radius of 2 cm. The cone should be no larger than necessary to expose the require cell area to flow.

Cone Angle: the cone angle has an exponential relationship with the modified Reynolds number, which increases with angle. The angle should be reduced to ensure laminar flow. Furthermore, decreasing the cone angle will create a greater shear stress for a given angular velocity, which allows greater FSS to be attained at lower motor output. The limitation of cone angle is fabrication techniques and materials. A small cone angle will require smaller tolerances and greater precision.

Cone Angular Velocity: the cone angular velocity is directly proportional to the modified Reynolds number, and therefore has a smaller impact compared to radius and angle. The angular velocity must be minimized to reduce the required motor speed, which will reduce power requirements and the potential for system vibration and wear. The upper limitations on angular velocity arise from the motor and power requirements.

Fluid Viscosity: the fluid viscosity is inversely related to the modified Reynolds number and proportional to the shear stress. The fluid viscosity can be increased to increase shear stress at given angle and speed, while simultaneously decreasing the corresponding modified Reynolds number. The limitations on viscosity pertain to the ability to accurately alter the viscosity of the culture media using an inert additive such as dextran.

2.5.3 Prototype Sub-System 01: Cone Geometry Design and Fabrication

To select cone angle, values between 0.5° and 1.5° were plotted against the FSS and modified Reynolds number using the viscosity of saline as an approximate to cell culture media at 37°C. The resulting FSS is computed from 0 to 40 dynes/cm^2 as required by the specifications

previously defined (Figure 7). This supports the expected outcome that reducing cone angle will reduce the angular velocity necessary to produce the requisite FSS.

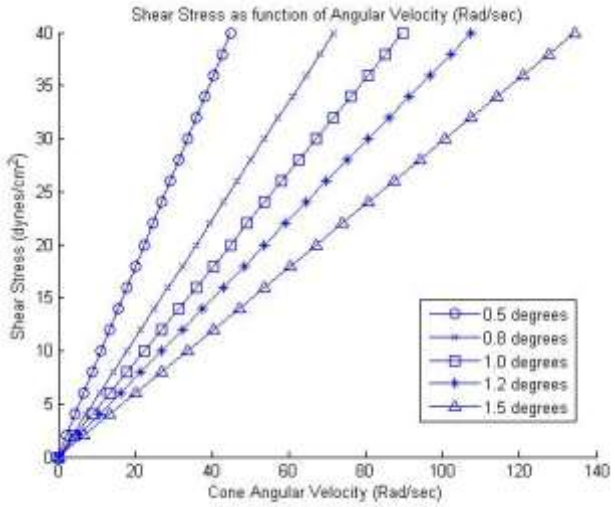

Figure 7: Shear stress as a function of angular velocity with varied cone angle

The modified Reynolds number is plotted in Figure 8 vs. FSS from 0 to 40 dynes/cm^2 with varied cone angle. Each calculation is made at the cone edge, where the radius and hence the modified Reynolds number are largest. At the largest cone angle of 1.5°, the modified Reynolds number is approximately 6, indicating that Re* > 1 at the largest FSS required for this project. A cone angle of 1° was selected to achieve laminar flow with Re* < 1 at 20 dynes/cm^2 with the given fluid viscosity of culture media. While this angle may not afford the lowest possible modified Reynolds number, this angle can be fabricated by manual lathe and machining methods. To achieve FSS greater than 20 dynes/cm^2, the media will be adjusted with dextran to increase viscosity. This cone angle is also consistent with devices created and validated in the literature (Spruell & Baker, 2013).

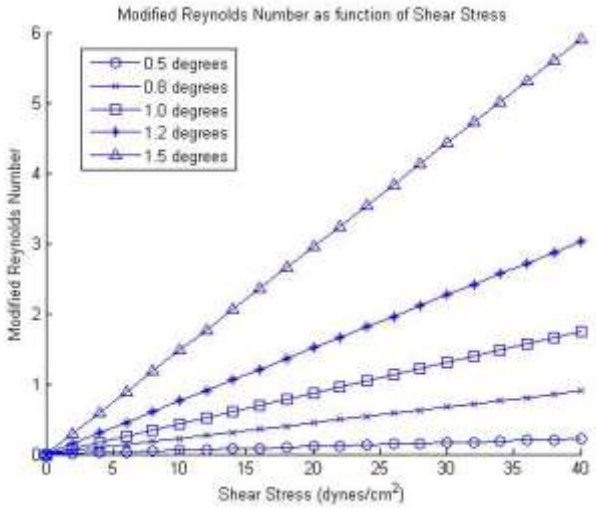

Figure 8: Modified Reynolds number as a function of FSS with varied cone angle

The cone was turned from a 2.25” diameter round stock of 6061 aluminum. A rough blank was made with a 1” diameter shaft for use in a collet chuck (Figure 9), which was selected for the greater stability compared to a jaw chuck. The cone was turned to final dimensions while mounted in the 1” collet, including a 1° taper on the cone surface. All operations were performed without removing the part from the collet to ensure circularity and concentricity of the surfaces. The cone was cooled to 4°C and press fit into the 2” steel taper bearing assembly (McMaster 6678K14) using an arbor press (Figure 10).

Figure 9: Cone with 1" collet shaft for mounting in lathe chuck

Figure 10: Cone press-fit into tapered roller bearing

The selected bearings are tapered roller bearings, used for the ability to constrain both axial and tangential shaft forces. This type of bearing is typically used in machinery applications requiring a shaft to be precision aligned while being subjected to forces along and perpendicular the shaft. This will be necessary as the cone will experience an axial force (gravity) while also experiencing a tangential tension force from the motor drive belt. The side view cut-away in

Figure 11 shows the roller orientation (shaded). The arrows represent the direction of reaction forces, which are capable of resisting applied load in the downward and tangential directions. Figure 12 shows a 3 dimensional CAD model of the bearing, with both the roller bearing and the tapered ring. These two parts nest together to form the tapered roller bearing.

Figure 11: Side view cut-away of 2" diameter steel tapered roller bearing with arrows representing reaction forces to indicate constrained directions

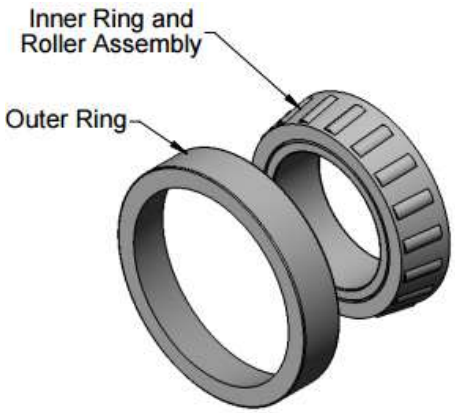

Figure 12: Assembly model of tapered roller bearing showing bearing and nesting ring

2.5.4 - Prototype Sub-System 02: Cone-Plate Gap Control Design and Fabrication

Precise control of the gap between the cone tip and the substrate is crucial for controlling the flow regime. Previous devices accomplished this using an electrical contact signal

that indicated when the cone tip made contact with the plate below, a method only applicable for a cone and substrate made of conductive material (Bussolari, Dewey, & Gimbrone, 1982). The conductive metal cone and baseplate completed a circuit when in contact to signal an indicator. However, this method is impossible when using a culture dish or gel substrate with inconsistencies between each samples' height. Furthermore, the delicate gel or plastic dish surface can be deformed by the rigid metal cone tip. Two designs were attempted to detect the cone tip height in relation to the substrate 1) change in electrical resistance across the gel and 2) force detection of the cone tip.

The objective of the electrical resistance sensor was to detect the changing resistance between a voltage applied to the cone tip and an electrode inserted in the dish bottom Figure 13. A voltmeter was used to detect the resistance through the culture media and gel layer as seen in Figure 14. As the probe was brought closer to the contact, it was expected that the resistance would decrease. Upon contact, the resistance would reach zero as a circuit was completed. Furthermore, it was expected that a difference in resistance would be encountered upon reaching the gel layer. This change could be used to detect contact between the cone tip and the gel layer, effectively setting the cone in the correct position for flow testing.

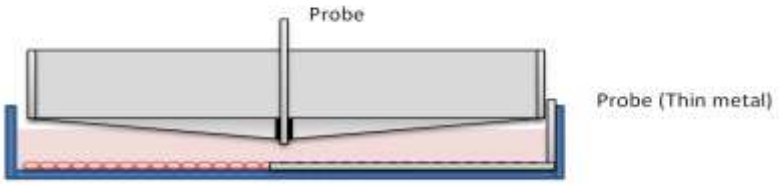

Figure 13: Electrical Contacts were located in the cone tip and along the bottom of the dish below the gel layer

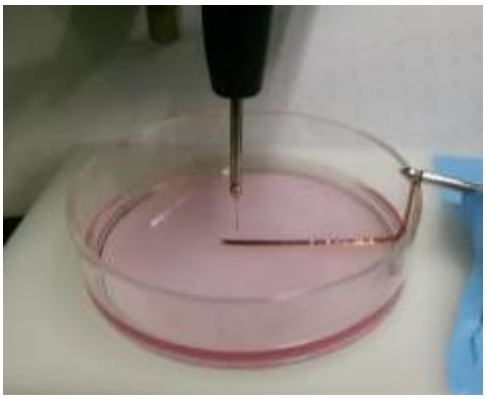

Figure 14: Voltmeter leads were connected to a narrow conductive probe mounted in the micrometer and to the metal foil contact in the dish bottom.

The voltmeter lead was a thin copper wire mounted in an Eppendorf micromanipulator. The other voltmeter lead contacted the metal foil in the dish bottom. The experimental setup is displayed in Figure 15.

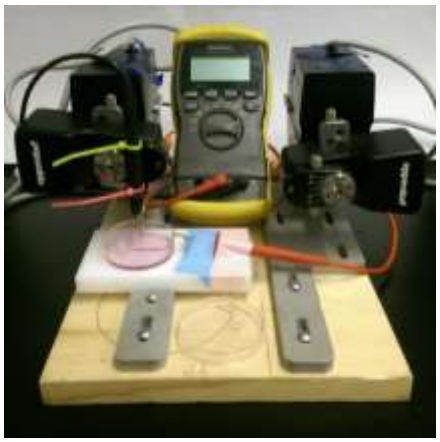

Figure 15: Micromanipulator with voltmeter. The culture dish can be seen on the white platform below the electrical probe.

A series of validation experiments using different dish contents were conducted to test resistance. In all tests, the probe was positioned 1 to 2 mm above the metal contact in the dish.

The probe was then lowered gradually using the micromanipulator while resistance readings were recorded.

1) Distilled water:

The probe displayed infinite resistance before being lowered into contact with the water. Resistance is shown in Figure 16 as a function of probe position. As the probe neared the metal contact, resistance decreased nearly linearly. The probe made contact with the metal at the last data point, showing near zero resistance. This experiment demonstrated that the probe can detect resistance changes dependent upon distance between the contacts and therefore supported the proposed design.

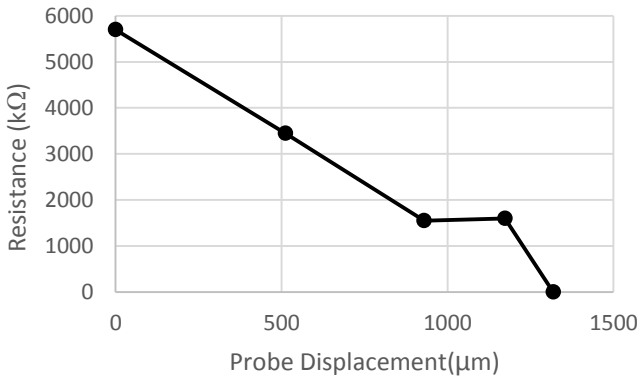

Figure 16: Resistance testing of sample containing only water.

2) Culture Media:

The previous experiment was replicated with culture media, which is accurate to actual use during live cell testing. The culture media contains salts and so was expected to show a higher conductivity and lower resistance compared to distilled water. The resistance followed a similar trend to the water, but displayed lower resistance values as expected. The resistance reached zero upon making contact with the metal in the dish, as expected (Figure 17). This

experiment demonstrated that the culture media displayed a resistance dependent upon distance between the electrical contacts, supporting the proposed design.

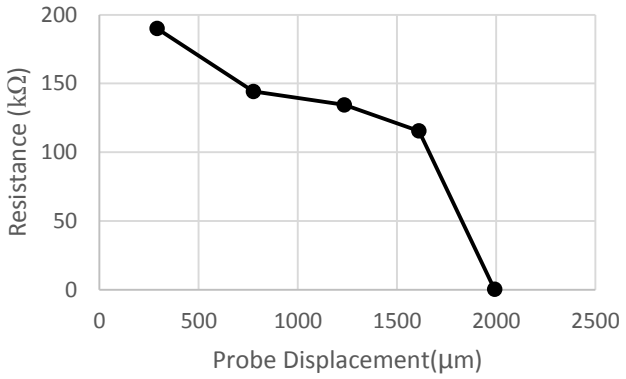

Figure 17: Resistance testing of sample containing only culture media.

3) No fluid, 2mm gelatin layer:

The next experiment tested the resistance characteristics of the gelatin layer. It was expected that gelatin would display similar resistance to the water and media but have a different conductivity upon contact. The resistance profile is shown in Figure 18, where only small fluctuations in resistance were detected as the probe moved. Unlike the fluid samples, the gel layer did not appear to have a strong dependency on resistance due to distance between the electrical contacts. These data were promising, as they indicated that the electrical properties change between the fluid and gel layer which may permit detection of the point when the cone comes in contact with the gel.

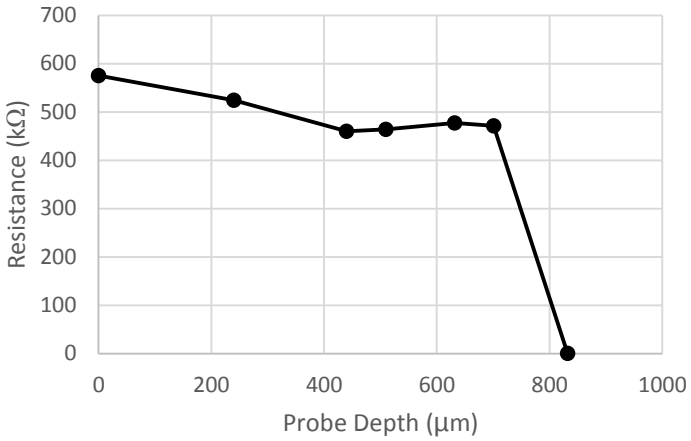

Figure 18: Resistance testing of 2mm thick gelatin layer without media.

4) Media with 2mm gelatin layer:

This experiment was accurate to the expected experimental setup, which will use a gel layer covered with media. At probe depth = 0, the probe was in contact with the media. It was expected that the resistance profile might show a change when the probe contacted the gel layer, but no change was observed until contact was made between the probe and the metal contact below the gel (Figure 19).

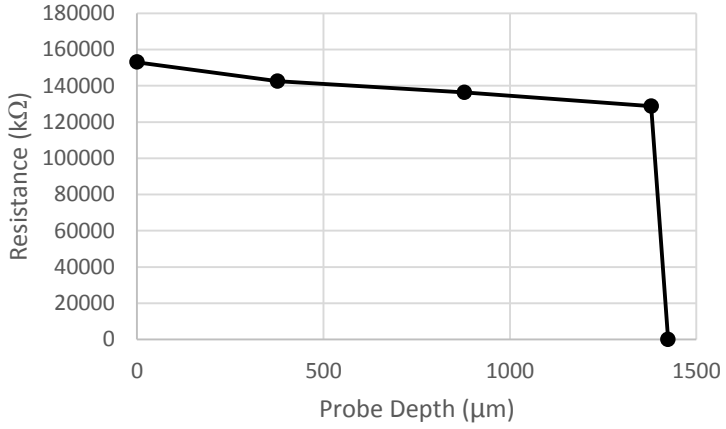

Figure 19: Resistance testing of 2mm thick gelatin layer with culture media

From these experiments, it was concluded that there was no detectable change in resistance between the fluid and the gel layer that indicated the beginning of the gel surface. This was likely due to the similarities in the gel and culture media, as both are highly conductive. The soaking of the gelatin in the media further homogenized the two materials.

The second method of gel layer detection was a force sensor to detect cone tip contact with the gel surface. This design proof of concept used a laboratory scale as a force sensor. Similar to the resistance testing, the cone tip was brought into contact with a culture dish containing a 2mm gelatin layer placed onto a scale as seen in Figure 20. A change of 0.2 grams was detected when the cone touched the dish, equating to a force of 0.00196 N. This force is hypothesized to be small enough for detection without causing a significant gel deformation under the cone tip.

Figure 20: Cone lowered onto laboratory scale to detect force upon contact

A similar design was pursued to integrate a force sensor capable of detecting cone tip contact into the cone and plate device. This design provided distinct advantages over the resistance testing described previously, including: 1) no metal electrodes were required, and 2)

the substrate was detected with or without the presence of the gel layer. Figure 21 shows a free body diagram illustrating the setup described in Figure 20.

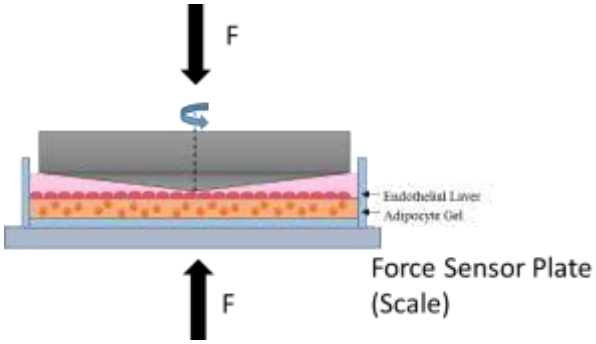

Figure 21: Free body diagram of proposed cone and force sensor plate

A piezoelectric resistive load sensor was selected for the 1) minimal displacement during loading, 2) slim, compact geometry, 3) simple resistive output and data reading. A 3/8" diameter, 1 pound capacity resistive load sensor (Flexi-force) was selected. A 1 mm thick circle of PDMS rubber was cut and mounted to the surface of the load sensor to evenly transfer the load to the entire surface. To allow freedom of movement for the sensor plate, the plate was suspended upon 3 spiked pins fitted into matching recesses. These pivot hinges constrained the plate to move in the vertical direction. A schematic of the sensor plate and hinges is shown in Figure 22. A sensor "foot" made of polycarbonate was machined with a matching pivot joint and placed over the PDMS circle on the load sensor. The sensor and sensor foot are shown in detail in Figure 23.

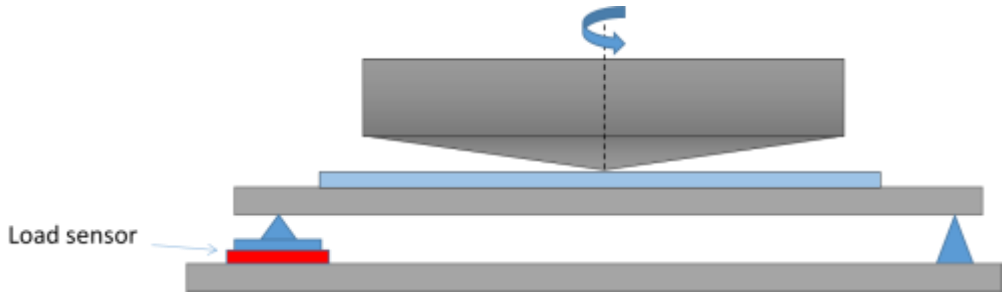

Figure 22: Schematic of force sensor plate with pivot hinges and load sensor

Figure 23: Resistive Load sensor with PDMS rubber spacer and sensor foot with pivot spike

The sensor output was read as a change in resistance detected by an Arduino Uno microprocessor by applying a 5V potential across the sensor. The analog signal was filtered using a moving average filter to account for sensor reading fluctuations and displayed in real time using the Serial Monitor function in the Arduino software. Upon beginning the program, the sensor input was zeroed to account for the dish weight. A threshold was set to detect a 0.7% increase in resistance, indicating an increased force applied. The increased force signaled a visual cue (LED light) so that the operator could determine when the cone made contact with the gel layer. The sensor plate, electronics, and LEDs are shown in Figure 24.

Figure 24: Sensor plate electronics assembly with LED indicator lights

The sensor plate was made from a 0.25” polycarbonate plate, selected as the most rigid optically clear material to allow imaging through the device bottom. The hinge pins were made from 10-24 aluminum screws which had been ground to a point, allowing sensor plate pivoting. The sensor foot was turned from polycarbonate round stock and polished with 1000 grit sandpaper to ensure a flat contact with the piezoresistive load sensor.

To suspend the cone above the substrate, a vertically translating “carriage” plate was created to mount the cone, bearing, and motor. Vertical movement was constrained by using a dovetail-type sliding rail on each side of the carriage plate. This design is commonly used in the design of machinery to create very precise movement in one direction and maintain plate alignment as it travels up and down (Figure 25, Figure 26). Figure 27 and Figure 28 show a CAD model of the carriage plate assembly with the cone, bearing, and motor.

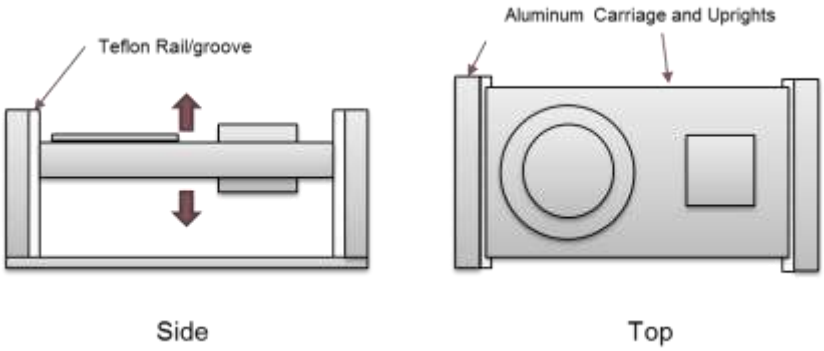

Figure 25: Diagram of Carriage plate with Teflon uprights and dovetail rails

Figure 26: Dovetail rail of carriage plate and vertical rail of Teflon upright

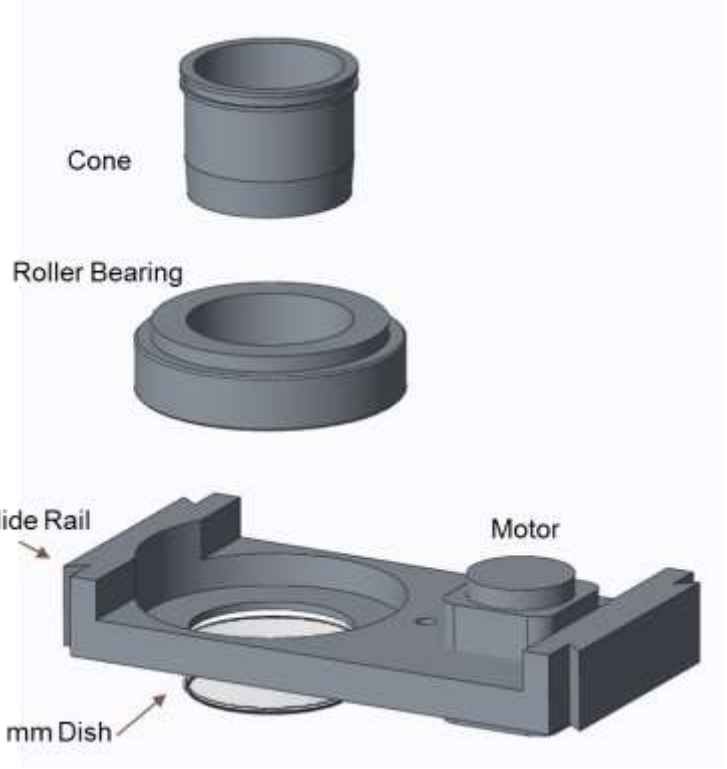

Figure 27: Carriage plate assembly with cone, bearing, and motor exploded view

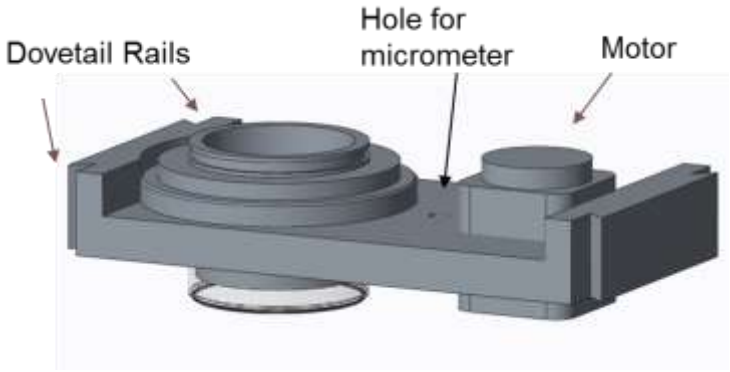

Figure 28: Carriage plate assembly with cone, bearing, and motor

A depth micrometer was selected as the control for vertical translation, as observed in previous devices in the literature (Blackman et al., 2000; Spruell & Baker, 2013). A digital depth micrometer with IP54 environment rating was selected (Fowler 54-225-456). This model had improved features compared to analog micrometers such as a digital readout with multiple

units, as well as the IP54 rating for water, humidity, and temperature resistance for use in laboratory and incubator environments. The micrometer was mounted in the center of the carriage plate, with the probe extending through a hole. Magnets were mounted using epoxy into groves machined into the carriage plate to lock the micrometer in place. Lengthening or retracting the micrometer probe allows the entire carriage plate, and therefore cone, to be moved vertically with +/- 0.001 mm precision.

A study was conducted to determine the sensor plate repeatability and determine if gel deformation occurred during gel surface detection. It was expected that the gel would deform elastically upon contact with the cone, even under the small force applied. To test this, two sample groups were used: one group with a bare culture dish and one group of a culture dish with a ~2mm gelatin layer. It was hypothesized that if a difference could be found between the bare dish and gel dish measurements, then the deformation of the gel was likely introducing error into the measurement. The cone was lowered using the micrometer and stopped when the surface was detected via the sensor plate. This was repeated on the same sample, and the frequency that each measurement was recorded were plotted in the histograms in Figure 29 and Figure 30 to demonstrate the distribution of measurements.

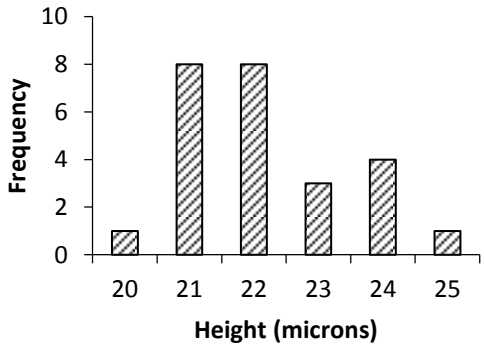

Figure 29: Sensor plate height detection, bare culture dish with no gel (n=25)

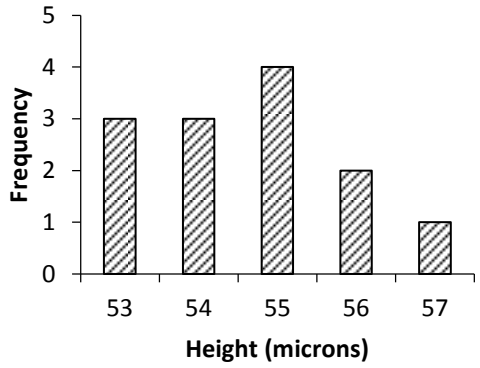

Figure 30: Sensor plate height detection with 2mm gelatin layer (n=13)

A T-test was used to determine that the two sets of measurements were not statistically different (P = 0.3042), and therefore the presence of the gel layer did not significantly change measurement repeatability from the bare dish. This suggests that the gel deformation was not a factor in repeatable detection of the surface, as the bare dish and the gel layer were not statistically different. The bare dish displayed a standard deviation of 1.28 µm, and a range of 5 µm. The gel layer sample displayed a standard deviation of 1.26 µm and a range of 4 µm. These values fell into the acceptable specifications previously defined for tolerance of detection. The descriptive statistics of both sample groups are in Table 3 and Table 4. However, it is important to note that this analysis only applies to the repeatability of the measurement and not the accuracy to the actual gel height.

Table 3: Descriptive statistics of gel height detection using force sensor plate in bare culture dish (n=27)

Bare Dish (µm)	
Average	22
SD	1.2

min	20
max	25
Tolerance	+/- 2.5

Table 4: Descriptive statistics of gel height detection using force sensor plate with 2mm gel layer (n=13)

2mm Gel Layer (µm)	
Average	54
SD	1.2
min	53
max	57
Tolerance	+/- 2.0

2.5.5 - Prototype Sub-System 03: Electrical and Motor Design and Fabrication

The motor must be capable of rotating the cone at the desired steady angular velocity. Furthermore, the motor must have sufficient torque to start from a standstill and maintain velocity even with fluid resistance from the sample. A list of motor specifications was identified and listed in Table 5 based upon standard parameters of motor performance (Bartheld, Robert G. Dippery et al., 2004).

Table 5: Motor design and selection parameters

	Parameter :	Description:	Value:
1	Constant Load Torque	Total resistance of load at steady operational speed	> 0.00784 Nm
2	Startup Torque	Total torque require to accelerate to speed	~0.104 Nm
3	Speed Range	Range of angular velocity at given load	85 Rad/sec
4	Effective Mom. Inertia	Total inertia of system (load+bearings+motor+gearing)	>0.00136 kgm^2
5	Ramp-up Time	Time to accelerate to desired speed	< 1 second

The constant load torque was approximated based upon the total shear force over the dish surface. At a dish radius of up to 2.5 cm, the surface area is 0.00196 m^2. A maximal shear stress of 40 dynes/cm^2 equates to 4 N/m^2, which creates a total rotational shear force of 0.00784 N. This force acts across the entire cone radius. If it were assumed that the entire shear force were focused at the cone edge (radius = 2.5 cm), a value of $1.96*10^{-4}$ N·m can be assigned for the constant load torque due to fluid resistance. This value is small, and therefore unlikely to limit the system capabilities. However, the actual constant load torque will be larger due to friction in the bearings and motor.

The startup torque of the system and effective inertia are a result of the cone friction and rotational inertia. The cone and bearing assembly inertia was computed by approximating the parts as a system of cylinders and rings, using Equation 5 and Equation 6 (Harrison, 1997). The mass of each component was measured using a balance. The total moment of inertia of the cone and bearing assembly was computed as the sum of the parts, and found to be ~0.000412

kgm^2. This value is small and nearly insignificant; however it does not take into account the static friction forces in the bearing or motor that may increase the startup torque required.

Equation 5: Moment of Inertia of solid cylinder

$$I_{cylinder} = \frac{1}{2}mr^2$$

Equation 6: Moment of Inertia of ring

$$I_{ring} = \frac{1}{2}m(R_1^2 + R_2^2)$$

An experiment was conducted to quantify the actual rotational inertia of the cone and bearing assembly. A thin wire was wrapped around the cone and passed over a pulley. A weight of known mass was suspended from the wire and allowed to fall while pulling the wire to rotate the cone. The weight was released and timed as it fell over a measured distance. Using the known distance, mass, geometry, and time, the moment of inertia was calculated to be 0.00136 kgm^2. Compared to the calculated value of 0.000412 kgm^2 this suggests that the majority of startup torque forces are a result of the friction within the bearing and not of the rotational inertia of the parts. The known gravitational force of the weight was then multiplied by the cone radius to yield an approximation of the torque required to accelerate the cone (0.104 N/m). Although this startup torque value depends upon the desired acceleration and top speed of the cone, the approximation provides some insight into the necessary torque specifications for the motor selection.

The motor speed range must be able to reach 1.5 radians per second to achieve the desired shear stress of 40 dynes/cm^2 with a 1° cone angle. While this is the maximum speed required for this application, a safety factor of 1.25 was applied to avoid running the motor at

the maximum allowable speed. This was intended to prevent over-heating and wear to extend motor life.

Considering the application specifications, a stepper-type motor was selected. A stepper motor is a DC electric motor capable of discrete, incremental motion controlled by input of digital signals allowing manipulation of the shaft position, velocity, and acceleration (Bartheld, Robert G. Dippery et al., 2004). Stepper motors offer advantages over brushless DC motors because the speed can be exactly controlled, regardless of the applied drag forces on the motor (Hughes, Austin Drury, 2013). This will be ideal for this application because exact control over cone velocity through a digital signal output from a computer is necessary to produce known fluid shear stress.

A two-phase NEMA 17 size stepper motor with 0.45 Nm of holding torque was selected (OMC 17HS16-2004S1). This motor is commonly available and used in automation applications such as robotics, CNC machines, and 3D printers. The capabilities include a 1.8° step increment angle, +/-5% positional accuracy, and an 80°C maximum temperature rise. The motor controller selected was an H-bridge motor driver (Rugged Circuits SQ4382777) with peak DC current of 2.8 A. This model was selected for features such as over-current protection, over-temperature protection, and a 2x safety factor for required current rating for the selected motor. Furthermore, the driver was compatible with the Arduino Uno microprocessor. A 15 V power supply (Hewlett-Packard) was used to provide DC power to the motor driver, as seen in Figure 31. The motor driver allows use of greater current and voltage than that provided by the microcontroller.

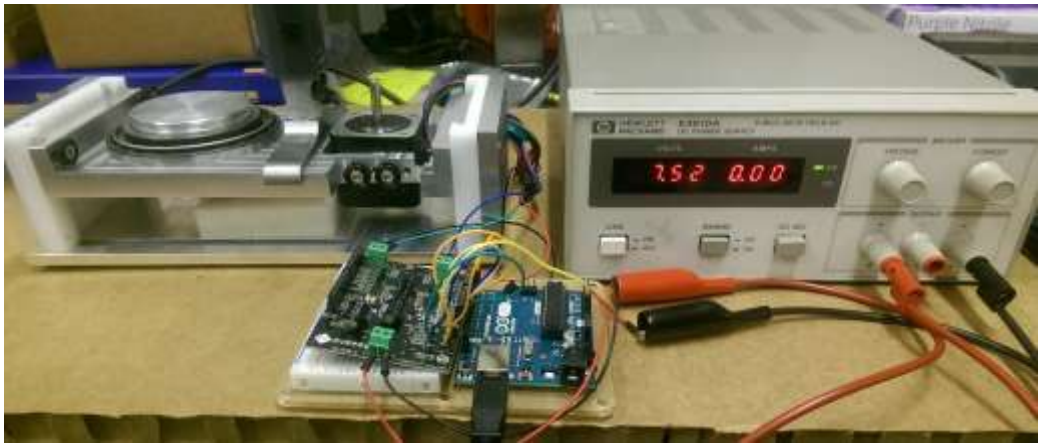

Figure 31: Arduino microcontroller, motor driver, and DC power supply

The microcontroller selected was an Arduino Uno microcontroller using an ATmega328 microprocessor. This controller provided basic functions and was capable of both analog and digital inputs and outputs. Furthermore, the open source Arduino software was an inexpensive and well supported prototyping platform. The microcontroller connected to a computer via USB cable and was powered by a 12V DC power supply. Programs were written on a computer using the Arduino software, then uploaded to the microprocessor where they operated independently of the computer. This feature was desirable, as the CPFD did not require a dedicated computer for operation and any personal computer could operate the software.

Optimal motor performance required synchronizing the proper pulse width modulation (PWM), a measure of power output, with the desired speed. This required increasing power to match the increasing speed. This relationship was determined experimentally by increasing motor speed and power incrementally and adjusting until the motor successfully operated. Successful operation was defined as smooth, noiseless motion at the desired speed. Unsuccessful operation was characterized by excessive vibration, noise, or a failure to move. This study was conducted with the motor in a 37°C incubator to simulate actual use conditions. Successful operating power was plotted from 0 to 500 RPM, at both 12 and 15 V DC power

(Figure 32). The power (PWM) and motor speed relationship was used as a reference for selecting the proper power for a given motor speed. The current used at each speed was measured and plotted in Figure 33, showing an exponential relationship between the current used and the motor speed. This study characterized the motor performance capabilities and confirmed the motor was capable of reaching the required speeds.

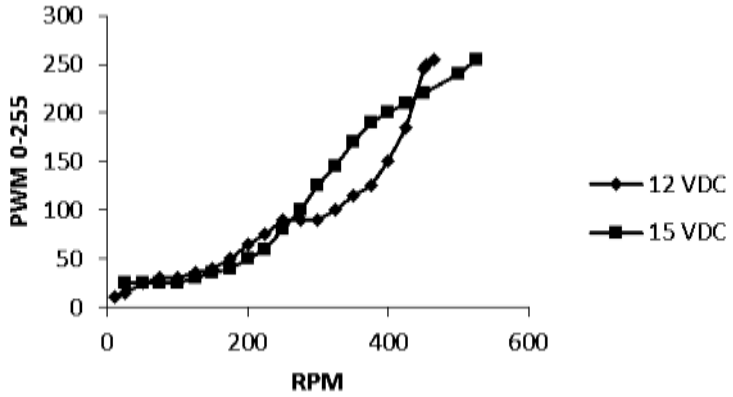

Figure 32: PWM plotted at varied motor speed for 12 and 15 volt DC power

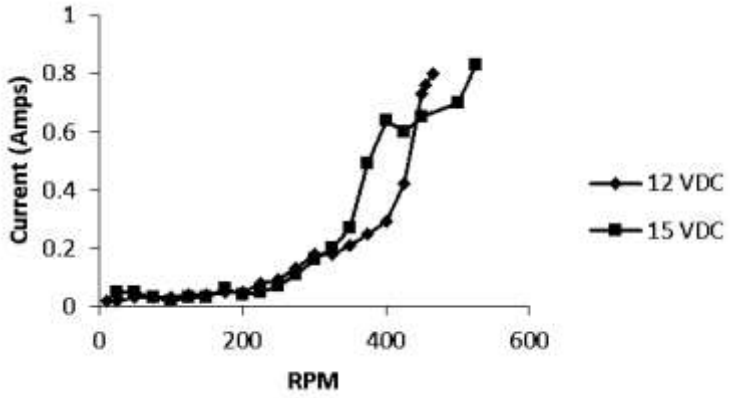

Figure 33: Current at varied motor speeds at 12 and 15 volt DC power

2.5.6 – Prototype Sub-System 04: Programming and Control Design and Fabrication

The program was written in Arduino version 1.6.7 for control of a single stepper motor utilizing an H-bridge motor drive. The microprocessor communicated to the motor drive using four outputs 1) ENABLE 1, 2) ENABLE 2, 3) DIRECTION 1, and 4) DIRECTION 2. These four data signals powered the four poles of the two-coil motor. Additionally, the microprocessor provided a 5V power and ground to the motor drive. An overview of the program is shown in Figure 34. The program controlled the 4 data signals which alternated their polarity in sequence, causing the motor to turn at the desired speed. Variable inputs were the motor angular velocity and the pulse width modulation. These values were entered into the "serial monitor" function and communicated directly to the microprocessor to adjust speed or power. The full program is shown in Appendix 3.

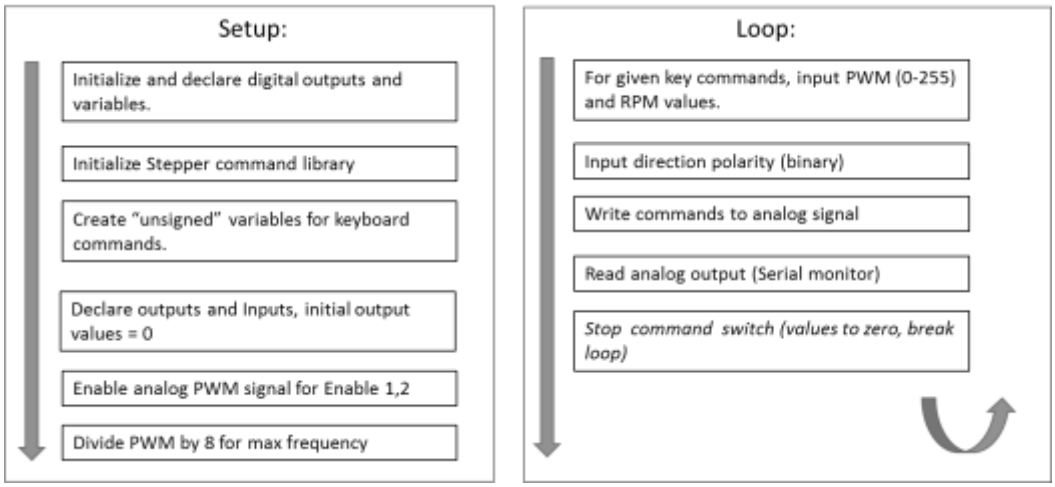

Figure 34: Flow chart of Arduino program for stepper motor control

2.5.7 – Prototype Cone & Plate Flow Device Validation

The prototype device validation experiments were conducted to confirm that the device could create laminar shear stress to stimulate NO production, verify that the cell type selected could be stimulated to produce NO, and to provide preliminary baseline data for future flow

testing with FFAs. Three experiments were performed: 1) Short acute flow time study at low shear stress (0-15 minutes, 6 dynes/cm^2), 2) Long acute flow time study at low shear (20-30 minutes, 6 dynes/cm^2), 3) Varied low shear stress (1,3,6 dynes/cm^2, 5 minutes). For a description of cell culture, solution preparation, and Western blot procedure, see section 4.2 – Methods. Negative control samples were subjected to no flow, but remained within the same incubator as the test samples during the experiment. Positive control samples were stimulated with insulin, a known p-eNOSp-eNOS stimulator, to ensure cells tested can in fact phosphorylate eNOS. A shear stress value of 6 dynes/cm^2 was selected for these experiments as it was expected to be large enough to phosphorylate eNOS, but low enough to ensure that cells would not be damaged or detached due to high flow.

1) Short acute flow time study at low shear stress (0-15 minutes, 6 dynes/cm^2):

This experiment was intended to confirm that the prototype device could stimulate cells with FSS to produce NO. BAECs were seeded at P5-P9 into 60mm culture dishes at a concentration of 200,000 cells/dish and allowed to grow for 48 hours until 90-100% confluent. Cells were serum starved for 3 hours with 1% FBS in DMEM before flow testing or insulin stimulation with 3% HEPES buffer (Sigma) (see section 4.2.2 – Preparation and use of Insulin Solutions). The flow experiment was conducted with the entire cone and plate prototype inside a cell culture incubator at 37°C, 80% humidity, and 5% CO_2. Samples were lysed and quantified for p-eNOSp-eNOS, eNOS, and β-Actin using Western blot as described in section 4.2.4 – Western Blot Protein Quantification. Sample groups are described in Table 6.

Table 6: Short acute flow time study at low shear stress (0-15 minutes, 6 dynes/cm2) samples groups

Sample:	Conditions	Size:
Control	Static	N = 2
5 minutes FSS	6 dynes/cm^2	N = 2
10 minutes FSS	6 dynes/cm^2	N = 2
15 minutes FSS	6 dynes/cm^2	N = 2
Insulin	100 nM Insulin for 3 mins	N = 2

The flow samples showed a clear 5 fold increase in eNOS phosphorylation as expected compared to the static group, which appeared consistent across all time points. The insulin positive control produced a 12 fold increase in p-eNOSp-eNOS (Figure 35a). The eNOS signal showed an inverse intensity compared to the p-eNOSp-eNOS, with a peak signal for the static control group (Figure 35b). β-actin was consistent and within a 1.0-0.8 fold change (Figure 41c). The Western blot protein bands are shown in Figure 35d and support the data shown in the quantification.

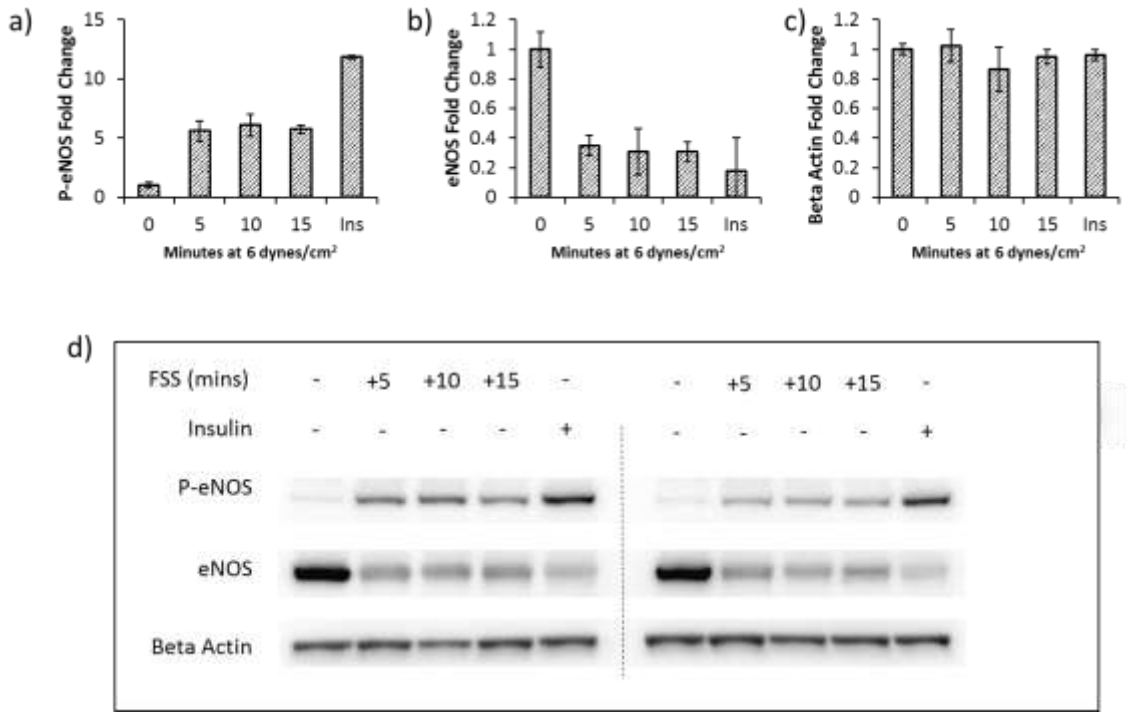

Figure 35: Short acute flow time study at low shear stress (0-15 minutes, 6 dynes/cm^2), a) p-eNOS fold change, b) eNOS fold change, c) β-actin fold change, d) Western blot bands of p-eNOS, eNOS, and B-actin

P-eNOS was normalized to eNOS to show the relative amount of eNOS phosphorylated, and normalized to β-actin to act as loading control. P-eNOS/eNOS values showed a ~20 fold increase in phosphorylation for flow samples compared to static samples (Figure 36a), with 5 minutes and 15 minutes showing statistical significance (Figure 36c). P-eNOS normalized to β-actin demonstrated a 6-7 fold increase in eNOS phosphorylation in flow samples compared to the static control (Figure 36b), with statistical significance for the 15 minute samples (Figure 36d).

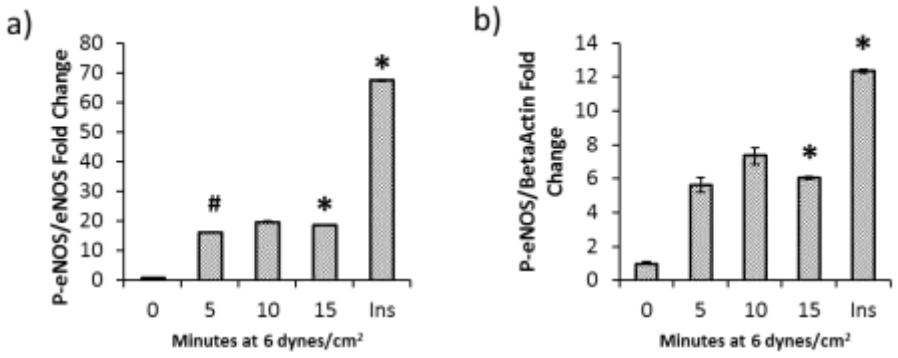

c)

P-eNOS/eNOS	
Unpaired T-test	p =
0 vs 5	0.0187
0 vs 10	0.0103
0 vs 15	0.0019
0 vs Ins	0.0068

d)

P-eNOS/beta actin	
Unpaired T-test	p =
0 vs 5	0.0571
0 vs 10	0.0639
0 vs 15	0.0035
0 vs Ins	0.0029

Figure 36: Short acute flow time study at low shear stress (0-15 minutes, 6 dynes/cm^2) results, a) P-eNOS normalized to eNOS, b) P-eNOS normalized to β-actin, c) P-eNOS/eNOS statistical analysis, d) P-eNOS/β-actin statistical analysis

2) Long acute flow time study at low shear stress (20-30 minutes, 6 dynes/cm^2)

This experiment was intended to confirm that the prototype device could stimulate cells with FSS to produce NO for time points 20-30 minutes. BAECs were seeded at P5-P9 into 60mm culture dishes at a concentration of 200,000 cells/dish and allowed to grow for 48 hours until 90-100% confluent. Cells were serum starved for 3 hours with 1% FBS in DMEM before flow testing or insulin stimulation with 3% HEPES buffer (Sigma) (see section 4.2.2 – Preparation and use of Insulin Solutions). The flow experiment was conducted with the entire cone and plate prototype inside a cell culture incubator at 37°C, 80% humidity, and 5% CO_2. Samples were lysed and quantified for p-eNOS, eNOS, and β-Actin using Western blot as described in section 4.2.4 – Western Blot Protein Quantification. Sample groups are described in Table 7: Long acute flow time study at low shear stress (20-30 minutes, 6 dynes/cm2) sample groups:

Table 7: Long acute flow time study at low shear stress (20-30 minutes, 6 dynes/cm^2) sample groups:

Sample:	Conditions:	Size:
Control	Static	N = 2
20 minutes FSS	6 dynes/cm^2	N = 2
25 minutes FSS	6 dynes/cm^2	N = 2
30 minutes FSS	6 dynes/cm^2	N = 2
Insulin	100 nM Insulin for 3 mins	N = 2

The 20, 25, and 30 minute groups produced a clear increase in mean p-eNOS signal, with a 5, 8, and 33 fold change respectively compared to the static control group (Figure 37a). The eNOS signal displayed an inverse intensity to the p-eNOS signal, with peak at the static control and lowest value at the 30 minute sample (Figure 37b). The β-actin signal was consistent, displaying less than a 1.0-0.9 fold change (Figure 37c). The quantified data were supported by the visual intensity of the Western blot proteins in Figure 37d.

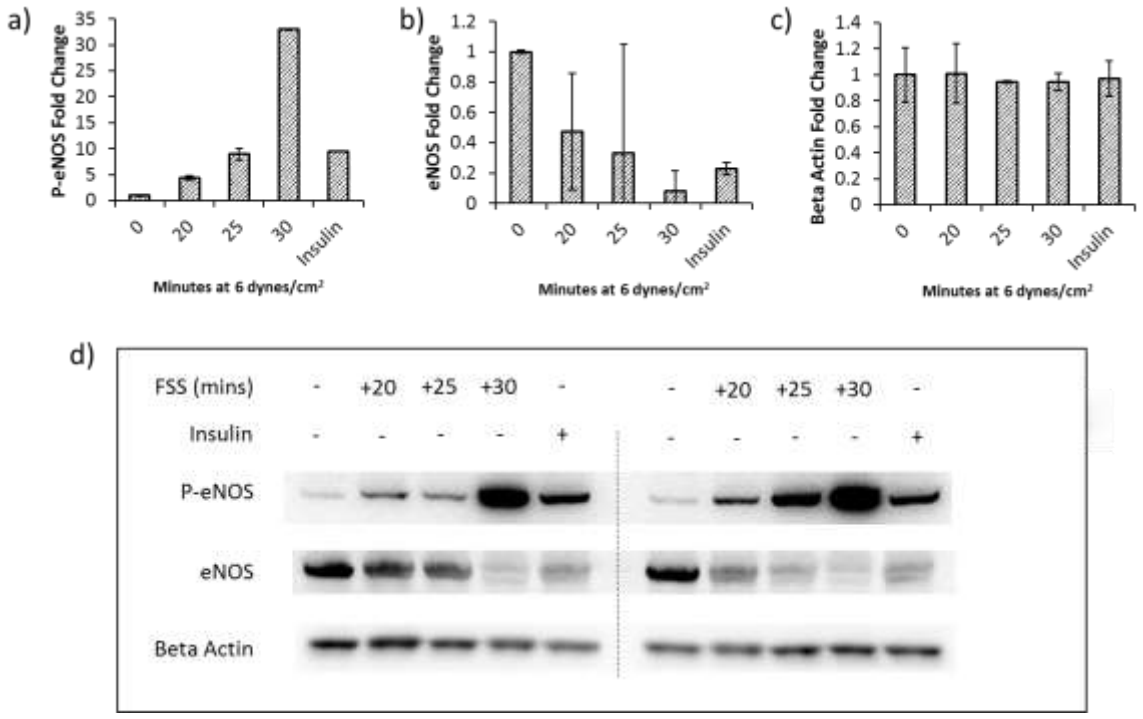

Figure 37: Long acute flow time study at low shear (20-30 minutes, 6 dynes/cm2) results, a) p-eNOS fold change, b) eNOS fold change, c) β-actin fold change, d) Western blot bands of p-eNOS, eNOS, and B-actin

P-eNOS normalization to eNOS displayed a significant change only for the 30 minute and insulin samples (Figure 38a,c). P-eNOS normalization to β-actin showed significance only for the 30 minute and insulin control samples as well (Figure 38b,d).

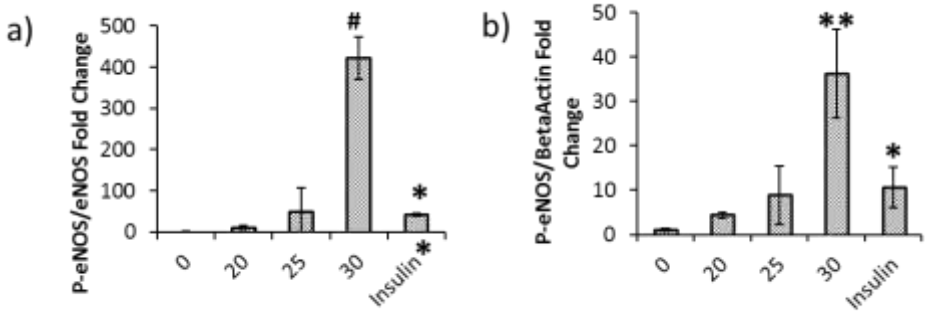

c)

P-eNOS/eNOS	
Unpaired T-test	p =
0 vs 20	0.0781
0 vs 25	0.1904
0 vs 30	0.0131
0 vs Ins	0.0004

d)

P-eNOS/beta actin	
Unpaired T-test	p =
0 vs 20	0.065
0 vs 25	0.157
0 vs 30	0.0003
0 vs Ins	0.006

Figure 38: Long acute flow time study at low shear (20-30 minutes, 6 dynes/cm^2) results, a) p-eNOS normalized to eNOS, b) p-eNOS normalized to β-actin, c) p-eNOS/eNOS statistical analysis, d) p-eNOS/β-actin statistical analysis

3) Varied low shear stress (1, 3, 6 dynes/cm^2, 5 minutes)

This experiment was intended to confirm that the prototype device could stimulate cells with FSS to produce NO, with a dependency based upon shear stress magnitude. BAECs were seeded at P5-P9 into 60mm culture dishes at a concentration of 200,000 cells/dish and allowed to grow for 48 hours until 90-100% confluent. Cells were serum starved for 3 hours with 1% FBS in DMEM before flow testing or insulin stimulation with 3% HEPES buffer (Sigma) (see section4.2.2 – Preparation and use of Insulin Solutions). The flow experiment was conducted with the entire cone and plate prototype inside a cell culture incubator at 37^{o}C, 80% humidity, and 5% CO_2. Samples were lysed and quantified for p-eNOS, eNOS, and β-Actin using Western blot as described in section 4.2.4 – Western Blot Protein Quantification. A flow duration of 5

minutes was selected, as this was the shortest duration shown to produce significant eNOS phosphorylation. Sample groups are described in Table 8.

Table 8: Varied low shear stress (1, 3, 6 dynes/cm2, 5 minutes) sample groups

Sample:	Conditions	Size:
Control	Static	N = 2
1 dynes/cm^2	5 minutes	N = 2
3 dynes/cm^2	5 minutes	N = 2
6 dynes/cm^2	5 minutes	N = 2
Insulin	100 nM Insulin for 3 mins	N = 2

P-eNOS signal increased with increasing shear stress magnitude, as expected. The 1 , 3, and 6 dynes/cm^2 resulted in a 3, 4, and 5 fold increase in mean value, respectively (Figure 39a). The eNOS signal produced an inverse change compared to the p-eNOS, with peak signal at the static sample and lowest signal at the insulin control (Figure 37b). The β-actin displayed a consistent signal except for a 1.3 fold mean increase for the 6 dynes/cm^2 samples. The Western blot band intensity agreed with the data quantification results (Figure 37d).

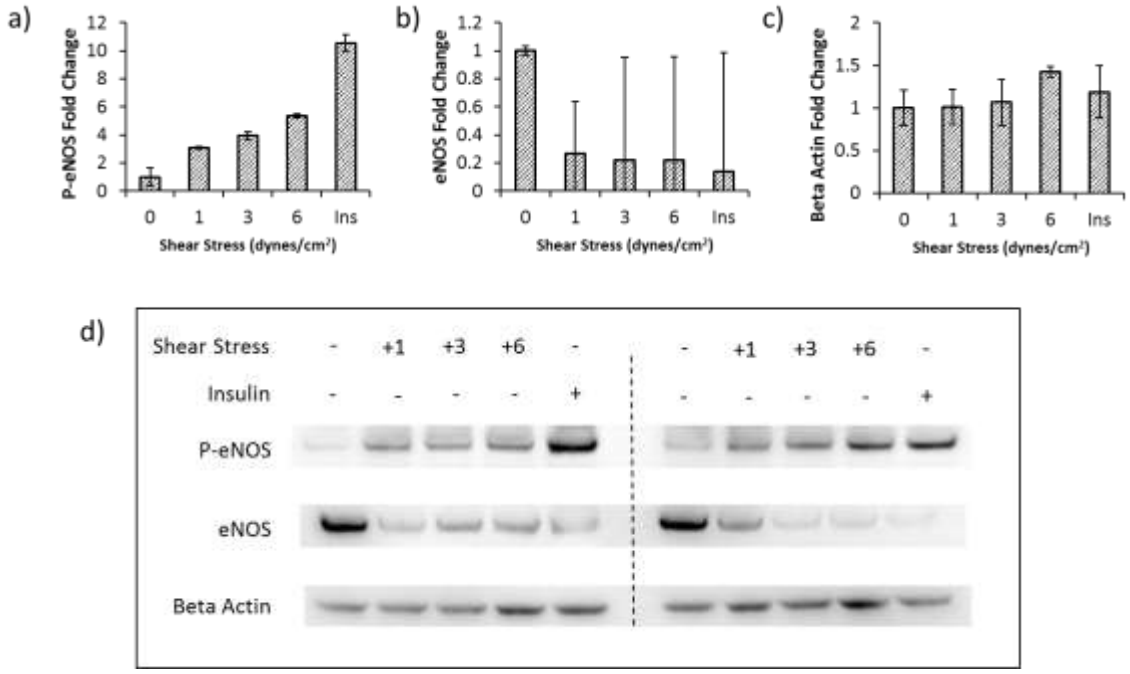

Figure 39: Varied low shear stress (1,3,6 dynes/cm^2, 5 minutes) results, a) p-eNOS fold change, b) eNOS fold change, c) β-actin fold change, d) Western blot bands of p-eNOS, eNOS, and B-actin

Normalization of p-eNOS to eNOS follows the trend of increasing mean signal with shear stress magnitude, but displayed a statistical significance only for the 1 dyne/cm^2 sample group (Figure 40a,c). Normalization of p-eNOS to β-actin displayed a more consistent ~4 fold increase in flow samples compared to the static control, and demonstrated a statistical significance for

the 1, 3, and 6 dynes/cm^2 sample groups (Figure 40b,c). Additional analysis showed that while there was significance between the static control and the respective flow groups, there was no statistical significance between the 1, 3, and 6 dynes/cm^2 groups.

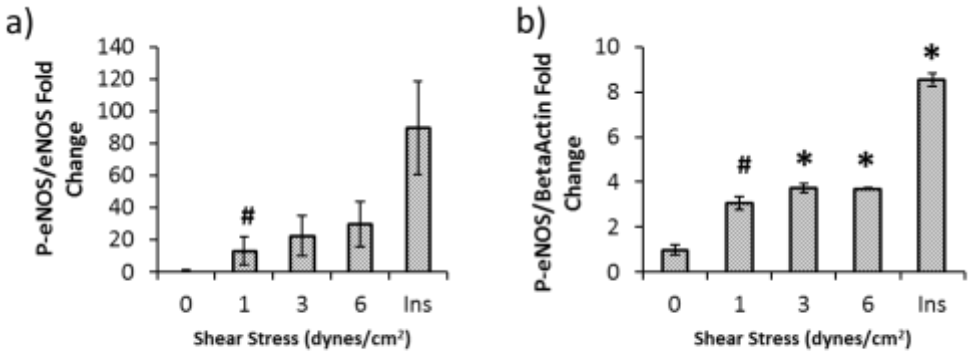

c)

P-eNOS/eNOS	
Unpaired T-test	p =
0 vs. 1	0.0299
0 vs. 3	0.1246
0 vs. 6	0.1132
0 vs. Ins	0.0861
1 vs. 3	0.4635
1 vs. 6	0.3695
3 vs. 6	0.7773

d)

P-eNOS/beta actin	
Unpaired T-test	p =
0 vs. 1	0.0175
0 vs. 3	0.0069
0 vs. 6	0.002
0 vs. Ins	0.0015
1 vs. 3	0.2668
1 vs. 6	0.1883
3 vs. 6	0.9537

Figure 40: Varied low shear stress (1,3,6 dynes/cm^2, 5 minutes) results, a) p-eNOS normalized to eNOS, b) p-eNOS normalized to β-actin, c) p-eNOS/eNOS statistical analysis, d) p-eNOS/β-actin statistical analysis

Overall, these experiments provided a proof of concept that the device was capable of stimulating eNOS phosphorylation in endothelial cells as intended. This knowledge supported following a similar design for the final cone and plate system.

2.5.8 – Prototype Cone & Plate Flow Device Capabilities, Limitations, and Discussion

The prototype device achieved nearly all of the design specifications previously created, with the exception of maximum FSS and sample throughput. The device created uniform laminar FSS over the required cell area, as calculated and validated through experimentation. The list of specifications and their assessment is shown in Table 9.

Table 9: Assessment of design specifications of prototype device:

#	Specification:	Success:	Result:
1	Modified Reynolds number < 1	Yes	Re* < 1
2	1 to 40 dynes/cm^2	No	Motor maximum speed insufficient at 15V
3	+/- 5.0 µm	Yes	Gel detection within +/- 2.0 µm
4	> 80% cell area at target FSS	Yes	86% of cell area is beneath cone.
5	15 cm^2 cell flow area	Yes	Western blot protein levels sufficient.
6	37^oC, 5% CO_2, 80% humidity	Yes	Device operates within incubator.
7	Optically clear bottom	Yes	Clear sensor plate and dish bottom.
8	Minimum 2 samples simultaneously	No	Only one prototype device.

The device mathematical model predicted that it produced laminar FSS, and these results were validated by showing the endothelial cells phosphorylated eNOS as expected when exposed to FSS in the CPFD. The maximum FSS however was not attained in this device due to the limitations of the power supply and motor gearing, factors that were addressed in the final device. The gel force detection method was validated as an accurate method to align the cone tip with the gel surface. The cone surface size was sufficient to subject 86% of the endothelial

cells to the desired FSS and provides the necessary 15 cm^2 of cell surface area for Western blot protein quantification, further validated by the device's use in live cell experiments and Western blot.

The prototype device was considered successful as a proof of concept and provided crucial insight for design changes. The final design iteration included a power supply capable of supplying up to 24 volts DC for increased maximum motor speed. The final system also included three independent cone and plate devices that could be operated simultaneously for increased experimental throughput. Other improvements included reduction in materials and dimensions. The rail system was replaced with a slide bearing system, as the sliding rails used in the prototype were found to be difficult to handle during use.

2.6 – Final Cone & Plate Flow System Design and Fabrication

2.6.1 – Cone & Plate Flow System Overview

The final design was again separated into 4 sub-systems: 1) Cone Geometry, 2) Cone-Plate Gap Control 3) Electrical and Motor, 4) Programming and Control similar to the prototype design. The following sections describe the design and fabrication of all parts of the final device, as well as validation of the aforementioned design specifications in Section 2.4 - Design Goals and Specifications.

The primary changes to the final system compared to the prototype were the creation of three independent CPFDs capable of simultaneous operation, fulfilling the specification of minimum two devices. Second, the motor power capabilities as well as the gearing ratio were modified to achieve sufficient cone velocity for > 40 dynes/cm^2 FSS. The full system with three cone and plate devices is shown in Figure 41.

Figure 41: Cone and plate flow system with 3 devices, motor controllers, drives, and power supply

2.5.2 – Fluid mechanics

The fluid mechanics utilized in CPFS are similar to those utilized in the prototype device. See section 2.5.2 - Fluid Mechanics for justifications.

2.5.3 – Cone & Plate Flow System 01: Cone Geometry Design and Fabrication

The cone geometry was changed from the prototype device to accommodate a smaller diameter bearing and drive belt repositioning. The cone angle was maintained at 1° due to the successful testing observed in the prototype device (see section 2.5.3 Prototype Sub-System 01: Cone Geometry Design and Fabrication). The material used was 6061 aluminum, which proved effective for the prototype device. Concentricity measurement was performed on the cone to compare concentricity of the cone to the cone shaft. A value of < 0.001” (0.025 µm) was measured for all three cones. The cone angle was measured by inverting the cone on a flat surface, then taking a height measurement at the cone tip and extents. The known radius and

height difference could be equated to angle using a trigonometric identity (tangent). All three cones were confirmed to be within 1.0° +/- 0.05° (more detailed measurement performed later in section 2.5.8 - Cone & Plate Flow System Experimental Validation).

The bearing diameter was reduced from a 2” diameter shaft to a 1.25” diameter shaft to reduce the assembly weight and cost and allow inclusion of gearing to increase the cone rotational velocity (see section 2.5.5 - Cone & Plate Flow System 03: Electrical and Motor Design and Fabrication). Additionally, the new bearing material was changed to a corrosion resistant steel to prevent corrosion observed in the prototype device. A second bearing was added to the shaft to further stabilize the device against the drive belt tension. This stabilizing bearing was mounted above the main bearing and resisted radial forces applied to the cone as shown in Figure 42. An image of the actual assembly is shown in Figure 43.

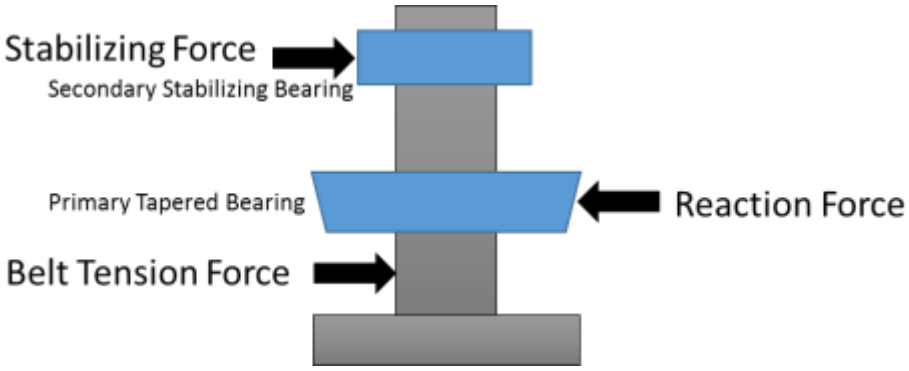

Figure 42: Free body diagram of bearing support for cone shaft with secondary stabilizing bearing

Figure 43: Image of cone and bearing assembly with primary tapered bearing and secondary stabilizing bearing (white)

The drive belt was reduced in size from a ¼" rubber belt to a 1/8" rubber belt, reducing cost and saving space. The drive belt was repositioned from above the carriage plate to below the carriage plate, requiring motor repositioning (see section 2.5.5 - Cone & Plate Flow System 03: Electrical and Motor Design and Fabrication). This change prevented the belt from interfering with the micrometer placement and acted as a safety precaution by positioning all moving parts inside the device. Figure 44 shows a side view of the device with the drive belt visible.

Figure 44: Side view of the drive belt (black) connecting the cone shaft and motor

2.5.4 - Cone & Plate Flow System 02: Cone-Plate Gap Control Design and Fabrication

The gap control feature was adapted from the prototype device into a more robust and easy to use design. The fundamental theory and operation remained unchanged (see section 2.5.4 - Prototype Sub-System 02: Cone-Plate Gap Control Design and Fabrication). The polycarbonate plate was replaced with an aluminum plate with a “dish cradle” designed to fit the P60 culture dish. The plate used 3 feet, including 2 rocker hinges and force sensor. The rocker hinges were machined from stainless steel and fitted into the sensor plate. The hinges were aligned vertically using a height micrometer to ensure the sensor plate was within +/- 0.001” of parallel to the device base, and therefore parallel to the cone. A 3D CAD model is shown in Figure 45, and an image of the final device is shown in Figure 46.

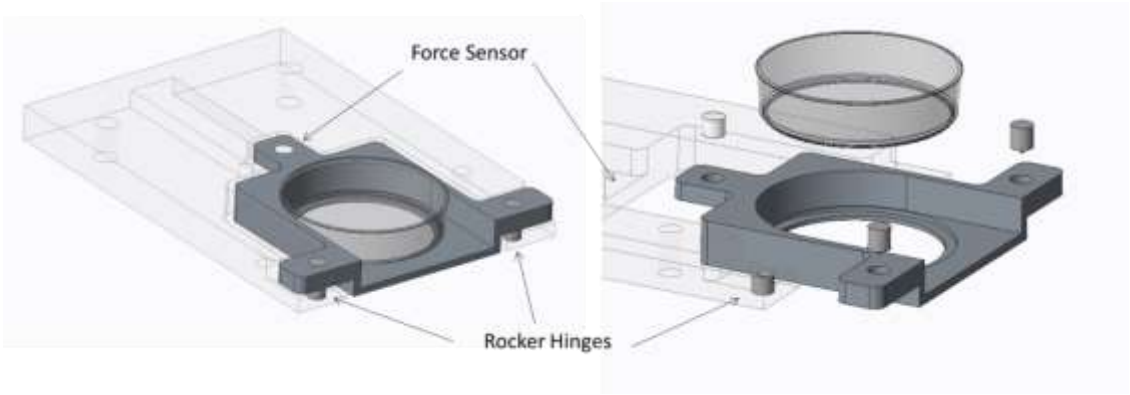

Figure 45: Model of force sensor plate using CREO 3.0

Figure 46: Image of force sensor plate mounted in device base

The sliding carriage plate was redesigned to incorporate linear sliding bearings to replace the sliding rails. These bearing provided smoother movement and constrained the movement to within 0.0005” alignment of the stainless steel slide shafts. The plate was made

from clear polycarbonate, which had similar properties to aluminum but offered easier machining, cleaning, and visibility. The micrometer mount was adapted to use two set screws to attach it in place, as this was more stable than the magnets used in the prototype version. Figure 47 shows the carriage plate lifted to demonstrate the sliding. The bearings and shaft were stainless steel for strength and corrosion resistance.

Figure 47: Expanded view demonstrating the sliding linear bearings and carriage plate

The gel height sensor was designed to operate similarly to the prototype device, and validated with a similar method using two experiments: 1) Validation of sensor precision for gel detection, and 2) Validation of sensor accuracy for gel detection. The precision validation was concerned with determining the range within which a gel layer can be detected, and establishing a tolerance for gel height. The accuracy validation was concerned with determining

how closely the detected gel height matches the height determined through measurement with confocal fluorescent microscopy as explained in section 3.6 – Validation of Hydrogel Mold for 3D Co-cultures in Cone and Plate Device.

1) Validation of Gel Sensor Precision

A P60 dish was measured via depth micrometer in the dish center, where the cone tip is expected to contact. 5 measurements of dish surface were also taken using the cone and plate force sensor, and averaged for the device. Gelatin was molded in the aforementioned P60 dish according to section 3.4 – Design of Hydrogel Mold for 3D co-cultures in Cone and Plate Device, and measured using fluorescent microscopy to determine the exact thickness of the gel layer. 5 microscope measurements of the gel thickness were performed at the dish center and averaged. The molded gel sample was then placed in the cone and plate device, with the micrometer zeroed at the previously recorded dish surface height. The cone was lowered until contact was detected, and the resulting value indicated the gel thickness. The microscope measured gel thickness was determined to be H = 317.30 µm, and force sensor measured gel height was determined to be h = 321.80. The resulting difference is a +4.498 µm, indicating a successful measurement within +/- 5 µm for this trial.

2) Validation of Gel Sensor Precision

To determine the precision of the sensor, a similar test was performed for this device as was performed for the prototype device in section 2.5.4 - Prototype Sub-System 02: Cone-Plate Gap Control Design and Fabrication. A bare dish and a gelatin coated dish were compared, and height measurements were recorded for 10 trials on the same samples, with the first measurement used to zero the micrometer. Results are plotted in the histograms in Figure 48. A range of +/- 2.0 µm was found for the bare dish, and a range of +/- 2.5 µm was found for the

gelatin dish, suggesting a minimal difference due to the gel. To confirm this, an unpaired T-test was performed on the two data sets. The resulting p value is 0.7586, strongly suggesting the presence of the gel does not significantly change the detected height precision.

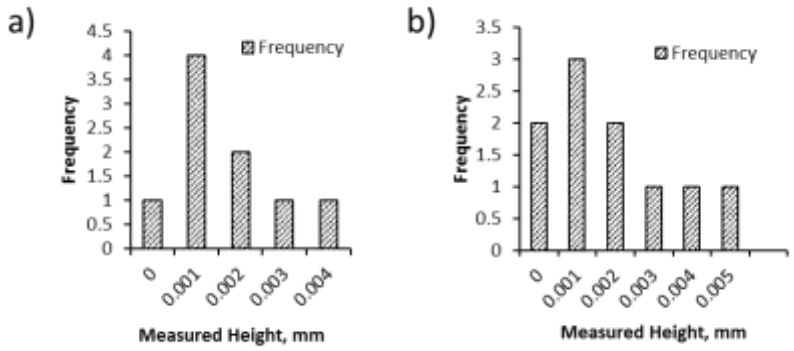

Figure 48: Validation of gel sensor precision with a) bare P60 dish and b) gelatin coated P60 dish

2.5.5 - Cone & Plate Flow System 03: Electrical and Motor Design and Fabrication

The motors used were the same model as those in the prototype device, as well as the motor driver and microcontroller (see section 2.5.5 - Prototype Sub-System 03: Electrical and Motor Design and Fabrication). The system was adapted to accommodate three sets of data outputs to control three devices, as shown in the electrical schematic (Figure 49). The motors shared a common input for the 5V power and ground, as well as the DIRECTION data input. An image of the electrical control system is shown in Figure 50.

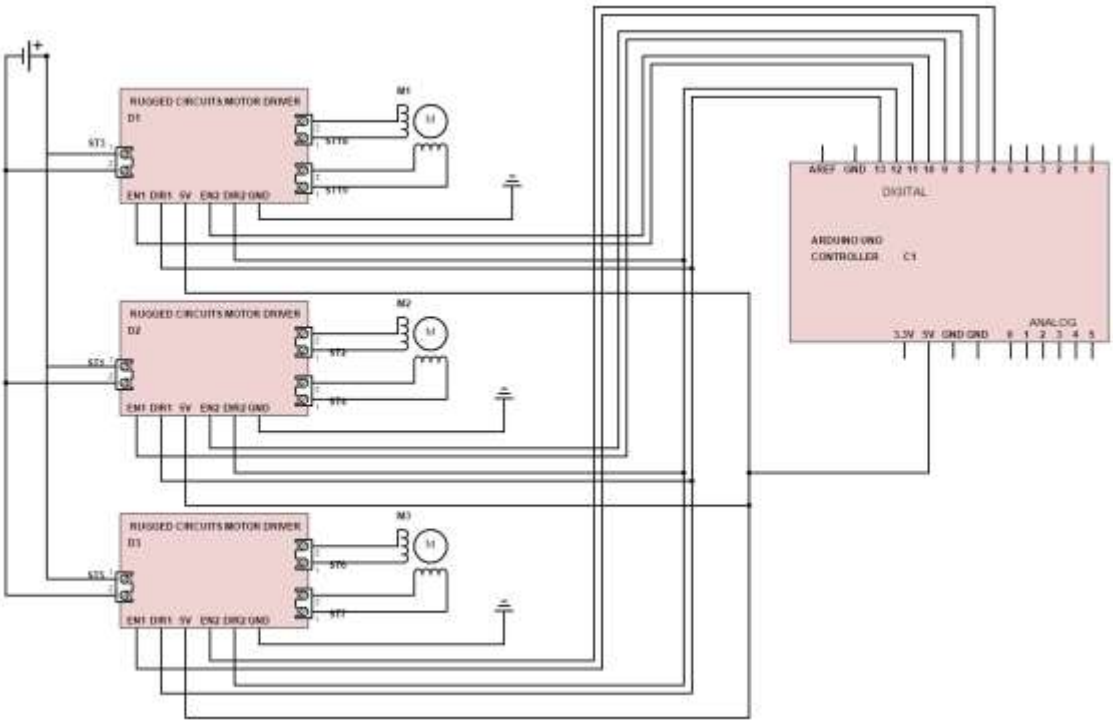

Figure 49: Electrical schematic of cone and plate flow system with three independent motors

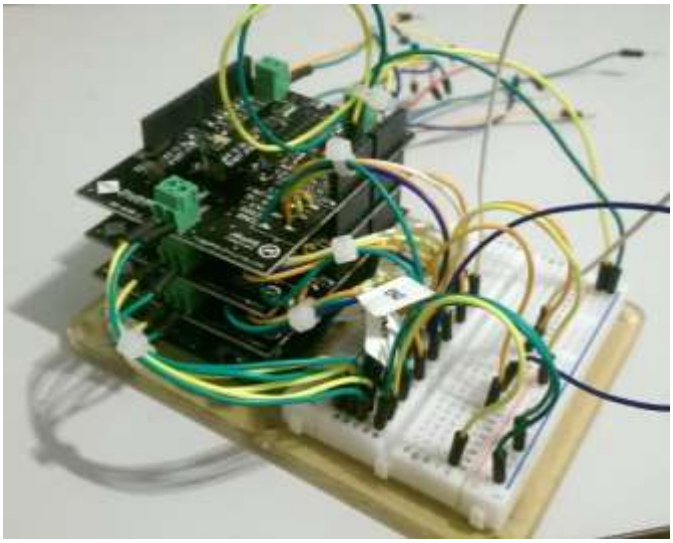

Figure 50: Cone and Plate flow system electrical controls, with Arduino microprocessor (bottom) and three motor drivers (top)

The motor drive wheel was adapted in this system to have a 1:1.5 gearing ratio with the cone shaft. The cone shaft diameter at the belt was 1”, and the drive wheel diameter was 1.5”. This allowed a factor of 1.5 to increase the speed output from the motor to achieve higher (40+ dynes/cm^2) FSS. Furthermore, this feature reduced the motor speed to reduce wear and heating and extend motor life.

2.5.6 - Cone & Plate Flow System 04: Programming and Control Design and Fabrication

The programming was adapted from the prototype to accommodate three devices, and followed a similar structure as described in section 2.5.6 – Prototype Sub-System 04: Programming and Control Design and Fabrication. This required the use of additional data pins to send signals controlling the ENABLE1, ENABLE 2, DIRECTION 1, and DIRECTION 2 poles of each motor. Variables were assigned to the speed and power input of each device and controlled using the serial monitor function in the Arduino software. The code can be found in Appendix 4: Arduino program for control of 3 stepper motors.

2.57 – Additional Design Changes and Justifications

A study was conducted to determine if cell media evaporation would be a problem during flow testing. Devices were operated in the incubator, and media weight was measured at time points during the test to detect evaporation, as shown in Figure 51. It was found that the media evaporated within several hours in both static and spinning dishes.

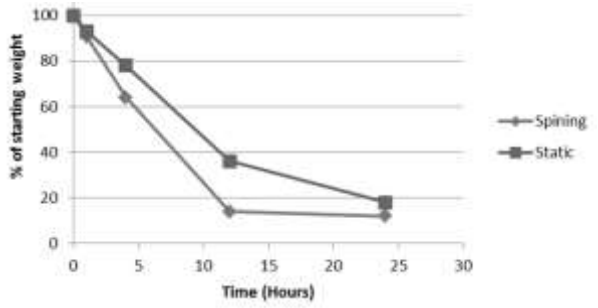

Figure 51: Media evaporation of spinning and static samples

To prepare the device for long flow testing durations, lids were created to prevent media evaporation from the dishes. The lids were machined from 1/8" thick Teflon and fitted to the P60 culture dish openings. The lids were installed on the cone shaft before mounting the shaft in the bearings. A CAD model is shown in Figure 52, and an image of the installed lid is shown in Figure 53. The lids maintained media volume for up to 24 hours of continuous flow testing.

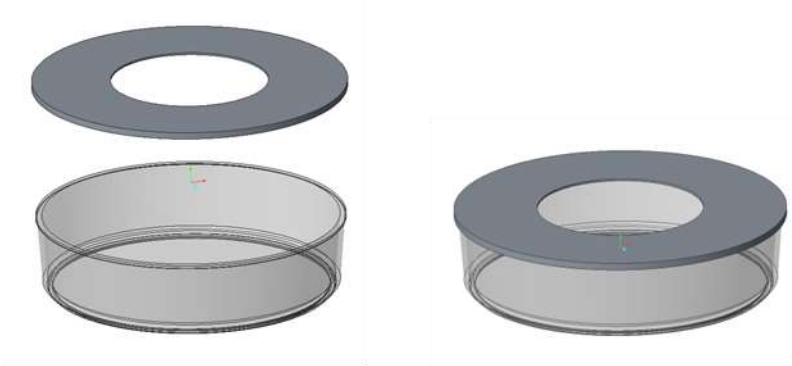

Figure 52: CAD drawing of dish lids

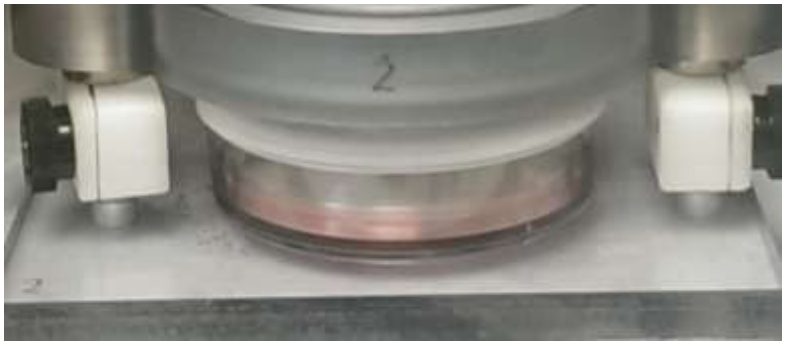

Figure 53: Image of dish lids installed on device

2.5.8 - Cone & Plate Flow System Experimental Validation

The cone and plate flow system was subjected to a series of experiments to validate its ability to keep cells alive and induce flow mediated eNOS phosphorylation. To confirm that the device produced laminar flow, 24 hour chronic flow tests were conducted to observe cell appearance and alignment. It was expected that if the device produced laminar flow and was compatible with cells, the results would show an elongated flow aligned phenotype.

1) Chronic Cone and Plate System 24 hour flow test at 20 dynes/cm^2

The system was tested with confluent BAECs seeded on to P60 dishes, using DMEM with 1% FBS and 3% HEPES. All flow experiments were conducted within a cell culture incubator, with samples run simultaneously on the 3 devices. Phase contrast images were taken before and after testing at 10x magnification. The 24 hour chronic experiment showed mixed results, with device 1 aligning cells and devices 2 and 3 causing cell detachment and death (Figure 54). This result did not indicate the cause of death or detachment, as cell toxicity and fluid forces could have been the cause. To isolate these factors, another experiment was performed with static samples left within the devices.

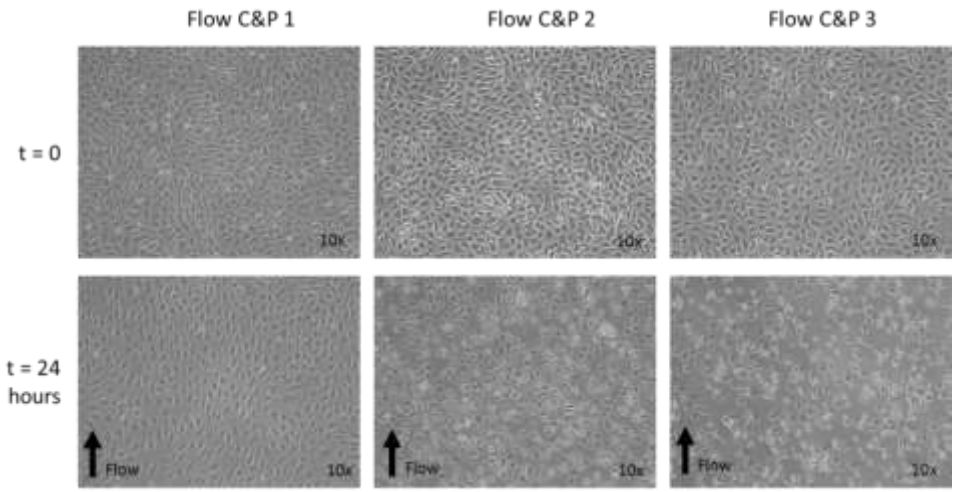

Figure 54: Chronic Cone and Plate System 24 hour flow test at 20 dynes/cm^2 phase contrast images at 10x magnification

2) Chronic 24 hour Static Test for Cell Survivability in Cone and Plate System

This experiment was intended to remove any potential toxicity from fluid forces to determine the cause of cell death in the previous experiment. BAECs were seeded into P60 culture dishes with DMEM 1% FBS and 3% HEPES and placed in the devices in a simulated flow test, however the device was left static. Phase contrast images taken before and after the 24 hour test period revealed that devices 1 and 2 kept cells alive for 24 hours; however device 3 showed cell detachment and death (Figure 55). A fourth control sample was kept in the same conditions but without a cone and showed cells alive after the test period. This result suggested that a toxic element was present in cone 3 that may have contaminated the media and killed cells. The most likely problems were residual chemicals and oils from the machining process that have lingered on the cone surface despite washing with ethanol and detergent, or lubricants from the bearings that traveled into the culture dish during testing. To eliminate these possible causes, inert and food-safe cutting oil and lubricant were found and the washing process was increased to include isopropyl alcohol, a solvent effective at removing cutting oil.

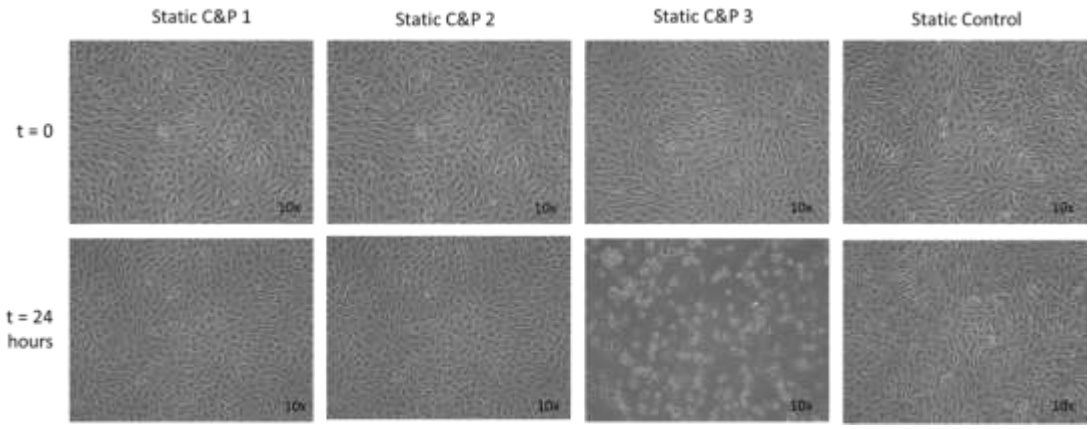

Figure 55: Chronic 24 hour Static Test for Cell Survivability in Cone and Plate System phase contract images at 10x magnification

3) Static Test for Lubricant and Cutting Oil Cytotoxicity

To test the cell compatibility of the proposed cutting oil and lubricant, a static test was conducted with BAECs with three conditions: 1) 50 µL/4mL of BioRad food-safe cutting oil/DMEM, 2) 50 µL/4mL of 3M Liquid silicone lubricant, 3) Dried 3M silicone lubricant, 4) static control with no additives. These materials were chosen as they were expected to be inert and non-toxic to live cells, even if they came into direct contact with the media. Cells were seeded into P60 dishes and grown to confluence for 48 hours, then media was changed to DMEM+10% FBS with the added chemical mixed in. Three samples were used for each condition. Phase contrast images were taken before the media change and after 24 hours in the cell culture incubator. The results showed that none of the samples tested displayed visible cell death or detachment, suggesting that these materials were suitable for use in the device (Figure 56).

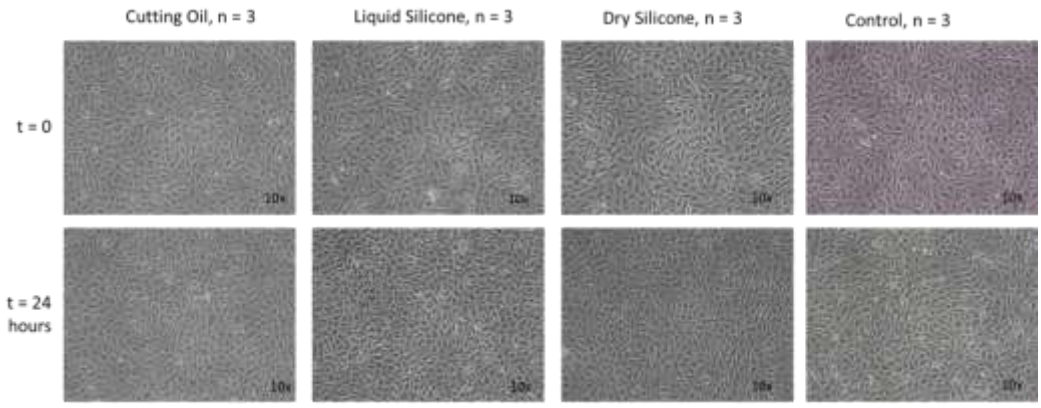

Figure 56: Static Test for Lubricant and Cutting Oil Cytotoxicity phase contrast images at 10x

4) Chronic 24 hour flow test at 20 dynes/cm^2

The cone and plate devices were resurfaced to remove the toxic compounds on the surface, then machined using the food-safe cutting oil previously validated. The cone and bearing assembly was then washed in 1% SDS detergent for 1 hour, then washed with ethanol and isopropyl alcohol to remove any trace of lubricant or cutting oil. The devices were reassembled and lubricated with the previously validated 3M silicone lubricant. A 24 chronic flow test was conducted at 20 dynes/cm^2 to observe if cells could now be kept alive in the devices. Phase contrast images were taken before and after the 24 hour flow, and the results showed that cells were successfully kept alive in all devices, suggesting that the problem of cytotoxicity was addressed due to the change in chemicals and improved cleaning (Figure 57). Furthermore, samples in devices 1 and 3 displayed successful flow alignment, validating that the devices produced laminar flow. However, device 2 did not display alignment and suggested that this device may not have produced the laminar flow as desired. This was hypothesized as a result of either unusual cell behavior or a result of inaccurate disturbed or turbulent flow produced by the device, possibly due to a machining misalignment.

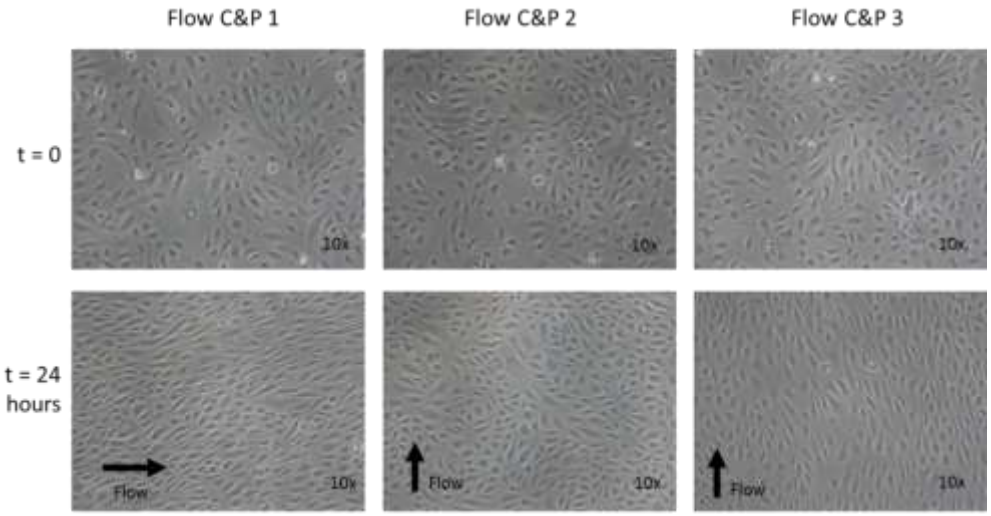

Figure 57: Chronic 24 hour flow test at 20 dynes/cm2 phase contrast images

4) Analysis of Cone Geometry and Bearing Alignment

To determine the cause of unaligned cells in the previous experiment, a more thorough measurement of cone alignment was conducted. Previous measurements were taken after machining to ensure that the cone angle was correct and the bearing and cone were concentric. However, these measurements did not account for the alignment of the cone surface to the culture dish sample. To measure this, a micrometer setup was created to allow measurement of the cone surface with the cone mounted in the device, as it would be used during operation. Vertical displacements were measured from the tip of the cone and extending radially in 4 directions (Figure 58).

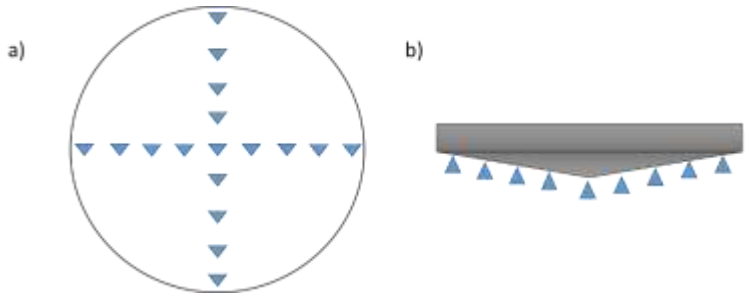

Figure 58: Diagram of micrometer measurement locations on cone surface a) top view, b) side view

The measurements were plotted with the radial location and vertical displacement, with the tip of the cone used as the datum. Standard deviation was plotted, as well as a linear fit equation with r^2 values (Figure 59). The plots showed a good surface flatness as r^2 values all exceed 0.99. However, cone 2 demonstrated a high deviation between measurements which increased radially. This suggests that while the cone is of correct geometry and surface finish, the alignment in the bearing relative to the culture dish may be inaccurate. As the cone rotates, this could cause fluctuations in the shear stress and compromise the laminar flow regime. This result agrees with that found in the chronic flow experiment, where cone 1 and 3 successfully aligned cells and cone 2 did not.

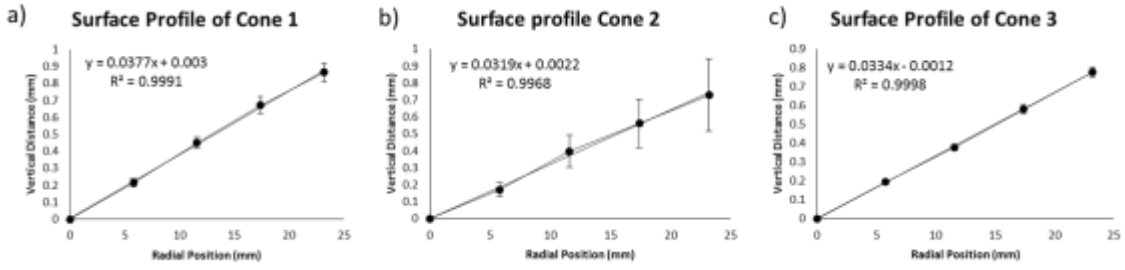

Figure 59: Surface profile of cones as function of radial position

5) Acute Flow mediated eNOS Phosphorylation at 20 dynes/cm^2

This experiment was intended to confirm that the prototype device could stimulate cells with FSS to produce NO, for time points 5, 15, and 30 minutes. BAECs were seeded at P5-P9 into 60mm culture dishes at a concentration of 200,000 cells/dish and allowed to grow for 48 hours until 90-100% confluent. Cells were serum starved for 3 hours with 1% FBS in DMEM before flow testing or insulin stimulation with 3% HEPES buffer (Sigma) (see4.2.2 – Preparation and use of Insulin Solutions). The flow experiment was conducted with the entire cone and plate devices inside a cell culture incubator at 37°C, 80% humidity, and 5% CO_2. Samples were lysed and quantified for p-eNOS, eNOS, and β-Actin using Western blot as described in section 4.2.4 – Western Blot Protein Quantification. Sample groups are described in Table 16.

Table 10: Acute Flow mediated eNOS Phosphorylation at 20 dynes/cm^2 sample groups

Sample:	Condition:	Size:
0 minutes FSS	Static control	N = 3
5 minutes FSS	20 dynes/cm^2	N = 3
15 minutes FSS	20 dynes/cm^2	N = 3
30 minutes FSS	20 dynes/cm^2	N = 3
Insulin	Static, 100nM Insulin 3 mins	N = 1

This experiment was successful in phosphorylating eNOS in all flow samples, with a mean 1.8 fold increase in all flow samples compared to the static control (Figure 60a). The eNOS signal displayed consistency for all samples, however did show a reduction in the insulin positive control, likely due to a defect in the blot (Figure 60b,d). The β-actin signal showed inconsistency, but it was unclear whether this is a result of the protein loading or possibly an incomplete transfer of proteins from the gel (Figure 60c,d).

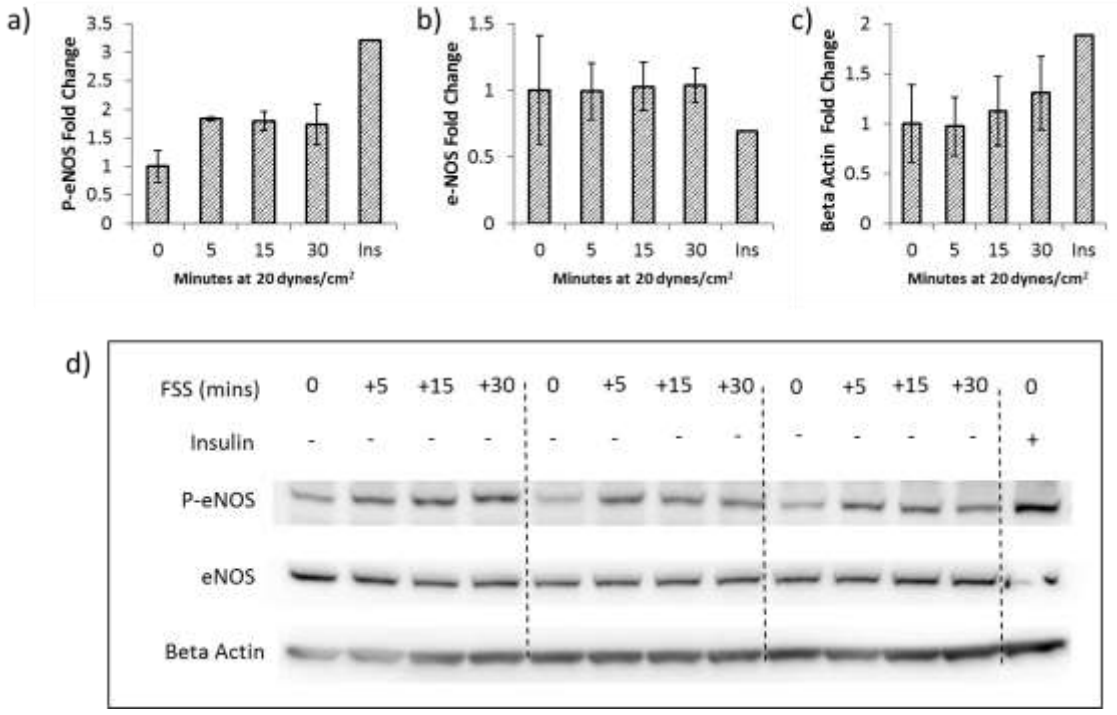

Figure 60: Acute Flow mediated eNOS phosphorylation at 20 dynes/cm^2 results, a) p-eNOS, b) eNOS, c) β-actin, d) Western blot protein bands

Normalization of the p-eNOS signal to total eNOS effectively reduced the variance and showed a 1.8 fold increase in p-eNOS/eNOS with statistical significance for all flow samples compared to the static control (Figure 61a,b). Normalization of p-eNOS to β-actin provided different results, likely due to the inconsistent levels of β-actin signal, especially in lanes 1-4. No statistical significance was found in p-eNOS/β-actin results (Figure 61c,d). Furthermore, no difference in p-eNOS phosphorylation was observed between sample groups on different

devices, suggesting that while device 2 may have affected cell alignment, it was still capable of inducing eNOS phosphorylation.

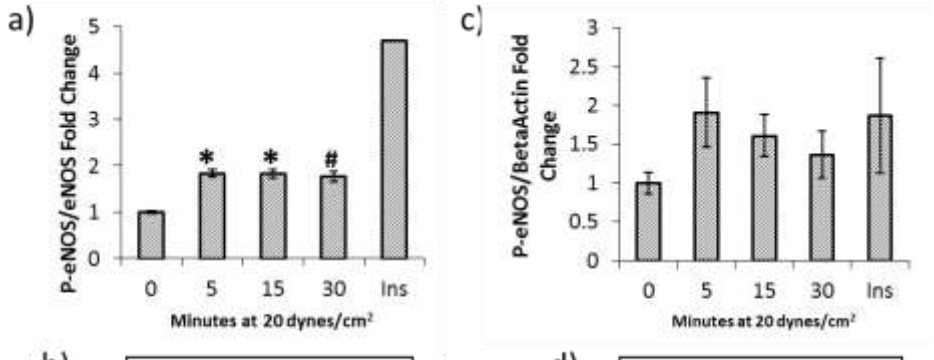

b)

P-eNOS/eNOS	
Unpaired T-test	p =
0 vs. 5	0.0026
0 vs. 15	0.0082
0 vs. 30	0.0257

d)

P-eNOS/beta actin	
Unpaired T-test	p =
0 vs. 5	0.0569
0 vs. 15	0.1354
0 vs. 30	0.2465

Figure 61: Acute Flow mediated eNOS Phosphorylation at 20 dynes/cm^2 results for a) p-eNOS normalized to eNOS, b) statistical analysis of p-eNOS/eNOS, c) p-eNOS normalized to β-actin, d) statistical analysis for p-eNOS/β-actin

2.5.9 - Cone & Plate Flow Device Capabilities, Limitations, and Discussion

The CPFD improved upon the prototype device substantially, with specifications listed in Table 11. Specifications already achieved such as modified Reynolds number, gel detection, target cell FSS area, and optically clear bottom were maintained. The motor capabilities were improved by increasing voltage from 12 to 24V, and gearing the motor with a 1.5 ratio to allow greater maximum speed. This allowed the peak shear stress necessary to be reached, though this would require either reduction of the cone angle to 0.5° or manipulation of the flow media to increase viscosity. The number of functioning devices was increased to 3, allowing triplicate samples to be run simultaneously. This not only reduced the duration needed for testing, but provided greater experimental control by subjecting replicates to the exact same experimental

conditions. Additionally, the CPFS improved the usability of the system with more robust and simpler user operation of both the device and software. The device was validated to phosphorylate eNOS in flow at a single shear stress as well as align cells in chronic flow; however more experiments should be done to fully characterize the eNOS phosphorylation at longer time points (> 30 minutes) and varied shear stress. Further improvements to the device should include a resurfacing of the cones with 0.5° angles, as well as confirming the accurate rotation of the cones while mounted in the bearing to ensure laminar flow.

Table 11: Achievement of Design specifications for cone and plate flow system

#	Specification:	Success:	Result:
1	Modified Reynolds number < 1	Yes	Re* < 1
2	1 to 40 dynes/cm^2	Y/N	Up to 850 RPM at 24 volts DC (viscosity adjustment)
3	+/- 5.0 µm	Yes	Gel detection within +/- 2.5 µm
4	> 80% cell area at target FSS	Yes	86% of cell area is beneath cone.
5	15 cm^2 cell flow area	Yes	Western blot protein levels sufficient.
6	37^{o}C, 5% CO_2, 80% humidity	Yes	Devices operates within incubator.
7	Optically clear bottom	Yes	Clear sensor plate and dish bottom.
8	Minimum 2 samples simultaneously	Yes	3 samples simultaneously

Chapter 3: Design and Validation of a 3D Hydrogel for use with Cone and Plate Flow Testing

3.1 – Introduction

Hydrogel scaffolds are widely used in microfluidics and tissue engineering because of their ability to be formed into complex geometries and simulate the native extracellular matrix (B. G. Chung, Lee, Khademhosseini, & Lee, 2012). Natural hydrogels include include collagen, agarose, alginate, chitosan, gelatin, and fibrin (Ratner, Hoffman, Schoen, & Lemons, 2013). Gelatin in particular is considered a good material for creating cellular scaffolds and substrate because it is naturally derived from collagen and contains RGD peptides to assist in cell adhesion (B. G. Chung et al., 2012).

Hydrogel co-culture has previously been used for endothelial cells and smooth muscle cells in flow. Type I collagen was used to create a scaffold for smooth muscle cells with an endothelial monolayer cultured on top of the cell-laden collagen. The entire 3D co-culture was then used in a parallel plate flow chamber (Ziegler et al., 1995). Enzymatically crosslinked gelatin was also used to create microchannels for microfluidic cell culture due to its ability to hold microscale dimensions when molded (He et al., 2016; A. L. Paguirigan & Beebe, 2007). The low relative cost of gelatin compared to other hydrogels (i.e. collagen) and the simplicity of enzymatic crosslinking made gelatin an ideal candidate for producing the co-culture structure in the relative large cone and plate device (Paguirigan & Beebe, 2006).

3.2 – Problem Statement

A flat gel layer of consistent height must be integrated into the P60 culture dish to enable endothelial cells to be co-cultured under flow with another cell type in a hydrogel. The gel layer must be compatible with the gel detection system previously described.

3.3 – Design Goals and Specifications

A successful hydrogel component must fulfil two main design specifications: 1) the gel must have a flat surface to maintain the cone and plate fluid mechanics, which necessitate a flat substrate for accurate shear stress, 2) the gel must be compatible with both an endothelial monolayer on the surface and a suspension of cells within the gel. The specifications are listed in Table 12. The tolerance for gel surface flatness was selected based upon the knowledge that crosslinked gelatin can be molded to micron resolution, and the limitation would likely therefore be in the dimensions of the apparatus designed for molding. A standard +/- 0.001" precision machining tolerance (~0.025mm) was selected assuming the gelatin would match the mold shape.

Table 12: Specifications of hydrogel co-culture component

Item:	Need:	Specification:
1	Flat gel surface for Couette flow	+/- 0.025 mm avg. flatness
2	Endothelial monolayer and suspended cell co-culture	48 hour cell survival

3.4 – Design of Hydrogel Mold for 3D co-cultures in Cone and Plate Device

The hydrogel mold was designed to create a hydrogel layer that covered the bottom of the P60 culture dish selected for the cone and plate device. The mold was designed to ensure the gel surface was independent of the dish surface shape, but parallel to the base of the dish. This was accomplished by "floating" a mold above the dish, as shown in Figure 62. Note that the mold surface is parallel to the base of the dish through a similar alignment technique of vertical slide posts as used in the cone and plate devices.

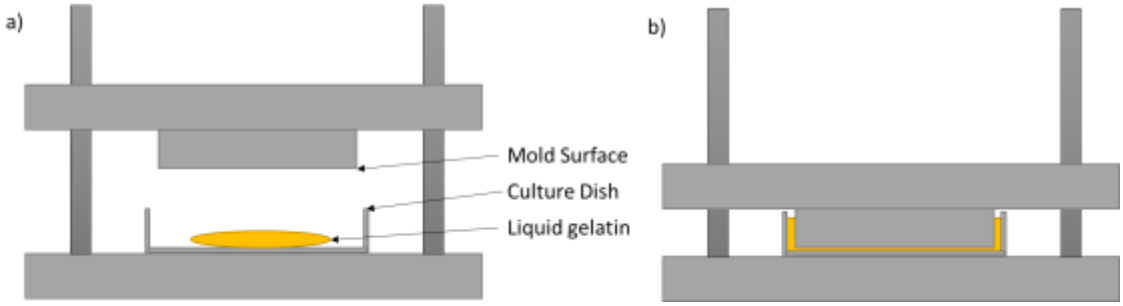

Figure 62: Hydrogel mold for P60 dish, a) before mold is lowered over added liquid, b) after mold is lowered to create molded gel

The mold surface was machined from Delrin acetal resin, chosen for small machining tolerance, chemical resistance, and hydrophobicity. The frame was made of clear polycarbonate, chosen for stiffness and low cost. The slide rails were 0.25” stainless steel, chosen for high stiffness and corrosion resistance. An adjustable stop was mounted between the base and mold block to allow adjustment of the gel thickness by rotating a screw. The mold can be seen closed with gelation in progress in Figure 63. Figure 64 shows the mold surface removed and inverted, and Figure 65 shows a P60 dish with crosslinked molded gelatin. Note the change in color from the center to the edges of the dish. This shows the change in gel thickness as it is thinner in the center where the dish surface is higher.

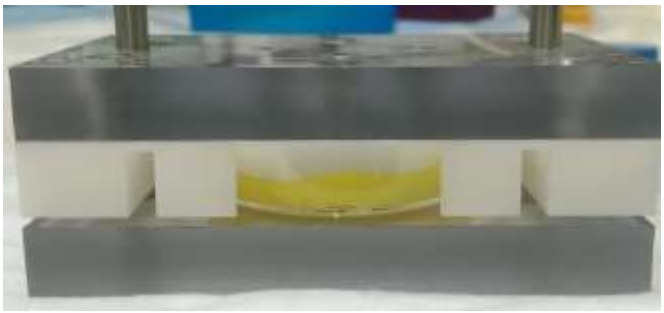

Figure 63: Closed mold with gelatin, yellow dye added for color

Figure 64: Inverted mold with surface visible

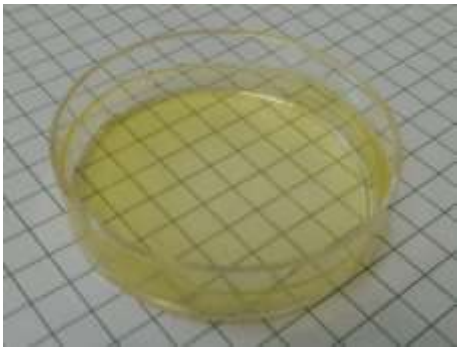

Figure 65: Molded crosslinked gelatin in P60 dish, with yellow dye added for color

3.5 – Protocol for Molding 3D Gelatin Layer

The gelatin crosslinking process using transglutaminase (TG) was adapted from Paguirigan et al. (A. L. Paguirigan & Beebe, 2007). A final mixture of 10% w/v bovine gelatin (Sigma) with 0.1 g/mL TG (Modernist Pantry) was prepared and molded. First, 1g bovine gelatin was dissolved into 9mL of PBS at 65°. A second solution was prepared of 0.5g TG in 5 mL of PBS at room temperature. 1.5 mL of crosslinked gelatin was prepared by mixing 1350 µL liquid gelatin with 150 µL liquid TG in PBS. The P60 culture dish was prepared by plasma treatment for 1 minute to increase gelatin adhesion to the dish surface. The mold surface was coated in a small amount of 3M silicone lubricant to improve mold hydrophobicity and act as a mold release agent. Immediately after plasma treatment, the crosslinked liquid gelatin was pipetted into the dish center and the mold was closed. The entire mold was placed in the cell incubator at 37° for

30 minutes to begin crosslinking, then allowed to cool to room temperature before separation. Gels were stored at 4°C until needed and UV sterilized for 5 minutes prior to use.

3.6 – Validation of Hydrogel Mold for 3D Co-cultures in Cone and Plate Device

Surface flatness was measured to validate the gel molding process. This was accomplished using a confocal fluorescent microscope, allowing gel layer measurement with micron accuracy. The gelatin was found to auto-fluoresce, allowing gel visualization by focusing the microscope while recording the z-axis displacement, measured in 0.0001 mm. Measurements were taken on gels radially as shown in Figure 66.

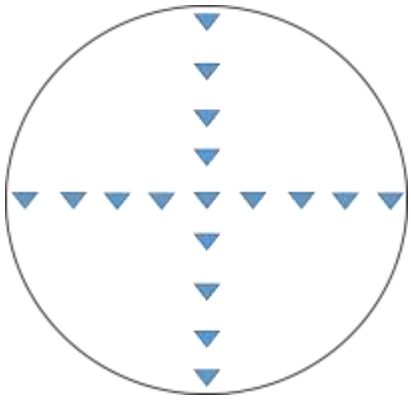

Figure 66: Diagram of gel surface measurements

To create the gel surface height profile, the dish was centered on the microscope stage. The z-axis was started from the lowest position and advanced vertically until the bottom gel surface was found (blue, Figure 67c). The z-axis was then advanced through the gel layer until the top surface was located, indicated by a transition from blue to dark blue (Figure 67b,c). This ~5 µm transition space was considered to be the gel surface, and a measurement of Z axis position was recorded. To characterize the surface, the z-axis was zeroed and additional measurements were taken by moving the dish and re-focusing on the gel surface.

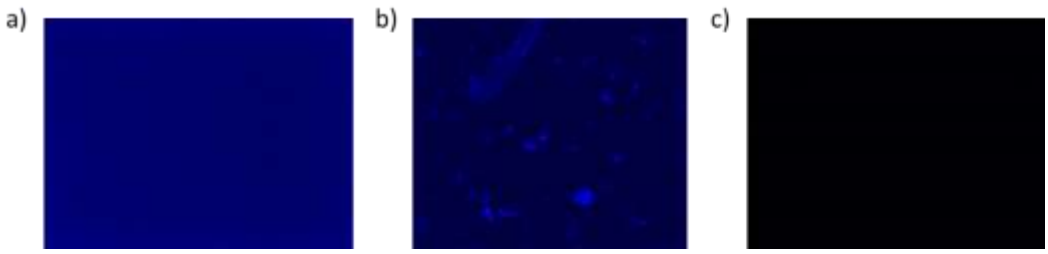

Figure 67: Confocal fluorescent microscope images of a) inside the gel layer, b) top surface of gel, c) above or below gel

A molded gel was measured according to this protocol, and the resulting four datasets were plotted in Figure 68. The top graph shows all data points measured from each of the four sets, resulting in 4 contours. The bottom plot shows the average and standard deviation plotted for each, with a third order polynomial equation fitted to the line. The measurement shows that the gel surface has the highest point in the center, and the gel height then reduces radially by a total of -96.40 µm at the extents. At a given radial position, the surface displayed a maximal range of 20.86 µm[M1].

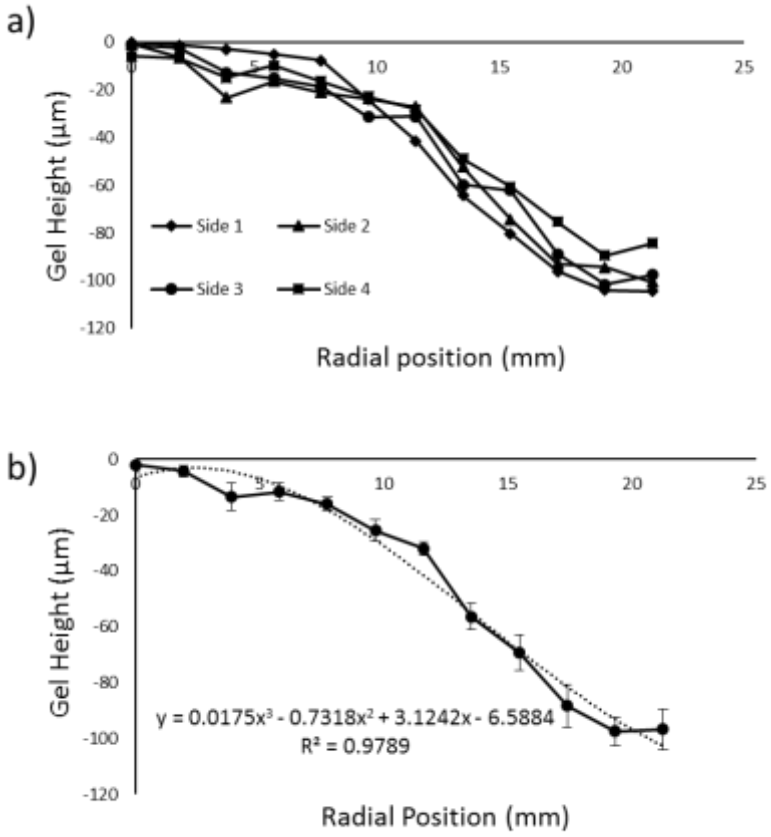

Figure 68: Measurement of gel height using confocal microscope, a) four data sets plotted together, b) four data sets averaged with standard deviation fit to third-order polynomial

3.7 – Discussion

The gel molding procedure developed here was partially successful, as it created an improved surface, but ultimately failed to meet the specification of +/- 25 µm of surface flatness. The variation between measurements at a given radius were within this specification; however the overall shape of the gel surface was raised in the center and lower at the extents, with an average change of 96.40 µm. This variation is likely due to error in machining, as a difference of 96.40 µm is a small value below standard machining tolerance of +/- 0.005". The radial change in dimension is also suggestive of a machining error, as the mold surface is cut from the center to the outside. Heating of the part during cutting could result in enough warping to cause this error. This could be solved by using a stainless steel or cast aluminum material for

the mold, though this would be a more expensive and time consuming process. A metal with greater rigidity than plastic could disperse heat more effectively and hold a surface tolerance near 0.001”.

Chapter 4: Endothelial Nitric Oxide Phosphorylation in the Presence of Circulating Free Fatty Acids

4.1 – Introduction

Elevated free fatty acids may play a role in vascular dysfunction by inhibiting endothelial nitric oxide production, leading to adipose tissue inflammation. Free fatty acids (FFA) are circulating lipids which have been introduced to the bloodstream from dietary intake or mobilized from stored triacylglycerides (TAG) in the adipose tissue. The movement of FFAs is a highly dynamic metabolic process and is primarily dictated by fasting, feeding, and exercise (Ballard, 1978; Lafontan, 2014). Among the symptoms of metabolic syndrome, obesity in particular has been linked to excessive FFA levels, especially after consuming a meal (Guenther Boden, 2008; Jansson et al., 1998). Excess FFAs inhibit the endothelial cells' ability to produce atheroprotective nitric oxide (NO), a vasodilator which promotes vascular health (Guenther Boden, 2008; Klöting et al., 2010; Scalia, 2013).

Nitric oxide production in the adipose tissue may be linked to blood flow in the adipose microvasculature, as endothelial NO production is known to be induced by shear stress (Kabirian et al., 2014; Noris et al., 1995). Adipose tissue blood flow (ATBF) is dynamically regulated by metabolic factors, and metabolic syndrome is linked with decreased pre- and post-prandial adipose tissue blood flow, especially in patients with insulin resistance and obesity (Goossens, 2008; Sotornik et al., 2012; Summers et al., 1999). This suggests that patients with metabolic syndrome, and specifically obesity, may exhibit a reduced shear stress during the post-prandial period, and therefore a reduced capacity to produce endothelial NO during this acute window of impaired flow.

The objective of this chapter was to determine the effects of FFAs and shear stress on endothelial nitric oxide synthase (eNOS) phosphorylation. The experiments were designed in three stages:

1. Determine shear stress timing required to induce eNOS phosphorylation. See section 2.5.8 - Cone & Plate Flow System Experimental Validation.

2. Confirm that FFAs inhibit eNOS Phosphorylation in response to insulin, as previously demonstrated in the literature (Kim et al., 2005).

3. Determine if increasing shear stress can maintain eNOS phosphorylation in the presence of FFAs.

4.2 – Methods

4.2.1 – Cell Culture

Bovine aortic endothelial cells (BAECs) were grown in Dulbecco's Modified Eagle Medium (DMEM) media with 10% fetal bovine serum (FBS), 0.5% penicillin streptomycin (PS), and 0.5% glutamine (G). BAECs were grown in a cell culture incubator at 37°C, 100% humidity, and 5% carbon dioxide. Cells were passaged at 75%-100% confluence in P100 culture dishes using Trypsin-EDTA and suspended in the culture media for seeding. Culture media was replaced every 48 hours during cell growth. Cells from passage 5 to 10 were used for all experiments. Cells were imaged with a Nikon phase contrast microscope at 4x and 10x magnification, with grayscale filter applied to the images.

4.2.2 – Preparation and use of Insulin Solutions

100 nM insulin in warm PBS was prepared for each experiment from a stock of 5mM insulin in 2.5 mM NaOH kept at 4°C. The stock solution was diluted from bovine pancreatic insulin (Sigma) in HEPES buffer. The insulin solution was kept on ice until the samples were prepared for testing. The insulin was added to a pre-warmed tube of PBS at 37°C and vortexed for 30 seconds. The current media was aspirated completely, then the sample was washed with 4 mL of warmed PBS. The PBS was aspirated completely and replaced with 4 mL of the 100 nM insulin solution and allowed to incubate at 37°C for the specified time, consistent with protocol from the literature (Kim et al., 2005). The insulin solution was immediately aspirated and the sample was washed with cold PBS according to the cell lysis protocol described in4.2.4 – Western Blot Protein Quantification.

4.2.3 – Preparation and use of Free Fatty Acid Solutions

100 μM palmitic acid in serum free DMEM was used for FFA incubations, based upon an existing protocol (Cousin et al., 2001). Palmitic acid (Sigma) was dissolved into 0.1M NaOH at 70°C to create a stock solution. The stock solution was then diluted into 10% bovine serum albumin in PBS (BSA, Sigma) and mixed at 55°C for 10 minutes. This solution was aliquoted and stored at -20°C for up to 4 weeks. Aliquots were thawed and diluted into serum free DMEM at 37°C for final 100nM concentration and added to cells for FFA incubation. The growth media was aspirated completely, then replaced with 4 mL of the 100 μM palmitic acid solution and incubated for 3 hours at 37°C until testing.

4.2.4 – Western Blot Protein Quantification

Western blot was used to measure relative levels of p-eNOS, eNOS, and βactin in the cell lysate. This assay uses gel electrophoresis to separate proteins based upon molecular weight

then transfer them to a membrane. The membrane is then incubated with targeted antibodies specific to the desired proteins, which are visualized using a chemiluminescent marker.

Following the experiment, cells were immediately placed on ice and the media aspirated. Samples were washed with PBS. If needed, cell images were taken at this point. Next the cold PBS was completely aspirated and 200 µL of lysis buffer (20mM TRIS base, 150mM NaCl, 2mM EDTA, 50mM NaF, 1mM Na_3VO_4, 1% v/v Triton X-100, 0.1% v/v 10% SDS, 10% v/v Glycerol) with protease inhibitor cocktail, PMSF, and 2x phosphatase inhibitor was added to the sample for 10 minutes at 4°C under gently rocking to completely lyse the cells. The sample was then removed from the rocker and scraped to acquire the BAEC lysate. The lysate was collected into 1.5mL centrifuge tubes then sonicated in a water bath at 10°C for 30 seconds at 1 Hz to further break the cell solids and shear DNA strands. The lysate was then centrifuged at 10,000 RPM for 10 minutes to isolate the solid material from the supernatant. The supernatant was removed without disturbing the cell pellet and aliquoted into 0.65 mL centrifuge tubes. Lysate was stored on ice for short term (less than 3 hours), or frozen at -80°C for long-term storage. Bichromatic Analysis (BCA) was performed to determine the relative protein concentration in each lysate to enable equal protein quantities to be loaded in the gel for each sample.

The desired lysate volume and deionized (DI) water were added to 0.65mL tubes and kept on ice. 2.5µL of SDS-PAGE sample buffer was added to each sample to create negative charge during denaturing. Lastly, 1 µL of reducing agent was added to the sample for a total volume of 10µL. All tubes were centrifuged for 30 seconds to collect the solution at the bottom, then vortexed for 5 seconds to mix. These samples were then immediately denatured in a hot water bath at 70-80°C for 10 minutes. Samples were then centrifuged for 30 seconds to re-collect the solution and remove air bubbles.

The gel electrophoresis system was placed in an insulated container and surrounded with ice. One or two 12% bis-tris gel cassettes (NuPAGE, Thermo Fischer Scientific) were mounted in the device and sealed. Cold MOPS buffer was added to the inner and outer chambers, and 500µL of anti-oxidant was added and mixed in the inner chamber. Samples were loaded using a micro-capillary pipette tip into the gel wells. A 5 µL protein standard ladder (Magic Mark, Thermo Fischer Scientific) was added to the left-most well in all gels. Gel electrophoresis was conducted at 200 mAmps for 1.5 hours or until the protein bands reached the bottom of the cassette. The gel cassette was then removed and rinsed in DI water.

The gel cassette was opened, and the gel removed and rinsed gently in DI water to remove MOPS buffer. The membrane stack was prepared for the iBlot Blotting System (Thermo Fischer Scientific) by first opening the bottom (electrode and membrane) layer and moistening with DI water. The gel was carefully placed on the membrane. A roller was used to remove bubbles between the gel and membrane. DI water soaked filter paper was placed on top of the gel, then the top stack electrode and sponge. The iBlot device was closed and run for 10 minutes at 25 volts to transfer proteins onto the membrane. The transfer stack was removed and disassembled and the membrane was immediately placed in a container of Tris Buffered Saline with Tween (TBS-T). Transfer was confirmed using a Coomassie Blue staining solution to visualize proteins remaining in the gel, and a Ponceau S red solution (Sigma) to visualize proteins transferred to the membrane.

All wash steps were done with a 5 mL rinse of TBS-T, followed by a 20mL TBS-T wash on the rocker for 10 minutes. After successful protein transfer was confirmed, the membrane was washed before adding 5 mL of 5% Blotto blocking solution in TBS-T (Thermo Fischer Scientific) for 1 hour at room temperature. The membrane was then washed and a 5 mL solution of primary antibody was added at 1:1000 dilution in 5% BSA in TBS-T and allowed to rock overnight

(8+ hours) at 4°C. The membrane was then washed and a 5 mL solution of secondary antibody at 1:2000 dilution in 5% Blotto in TBS-T was added for a 2 hour incubation at room temperature with rocking. After washing, the TBS-T was replaced with 10 mL of TBS and washed for an additional 5 minutes. A solution of 1.5 mL of chemiluminescent reagent (Luminol) was prepared immediately before use. The membrane was placed in a clean plastic container and chemiluminescent reagent was added to the entire surface and allowed to incubate for 1 minute. The membrane was placed in an Alpha Innotech Fluorchem SP Imager and exposed for varied time (1 second to 2 minutes) to detect the protein bands.

Once the appropriate protein bands were identified using the protein standard, protein levels were quantified using image spot-densitometry of the selected band regions. Measurement regions were identical in area and dimensions, and positioned over the entire band. Background subtraction was performed using a similarly sized region positioned directly below, but not overlapping, the target protein band. Spot density data was exported to Microsoft Excel for analysis and graphing. The raw data were normalized to the negative control sample for each membrane, and the average value was plotted in a bar graph. The standard deviation was normalized to the average of the sample, and plotted on the bar graph. Data were shown in relative fold change from the negative control samples.

4.2.5 – Statistical Analysis

Statistical analysis was performed using GraphPad Prism and Microsoft Excel. Data are presented as mean value with standard deviation. Western blot results are normalized to the static control sample to show fold change. A student's t-test for unpaired samples was used to analyze change between two groups of Western blot data. A p value < 0.05 is considered significant, where (**) $p < 0.001$, (*) $p < 0.01$, (#) < 0.05.

4.2.6 – Insulin Mediated eNOS Phosphorylation Experiment

This experiment validated that insulin induced eNOS phosphorylation and was used to select the treatment duration and the cell type for highest p-eNOS signal. It was hypothesized that the 5 minute insulin stimulation would be most effective, as demonstrated in Kim et al., and that bovine aortic endothelial cells (BAEC) would perform similarly to porcine aortic endothelial cells (PAEC) (Kim et al., 2005).

Cells were seeded at P5-P9 into 60mm culture dishes at a concentration of 200,000 cells/dish and allowed to grow for 48 hours until 90-100% confluent. Cells were serum starved for 3 hours with 1% FBS in DMEM before insulin stimulation (see section 4.2.2 – Preparation and use of Insulin Solutions) for 0, 2, 3, and 5 minutes, depending upon cell type. Samples were lysed and quantified for p-eNOS, eNOS, and β-Actin using Western blot as described in section 4.2.2 – Preparation and use of Insulin Solutions. A list of samples and conditions is shown in Table 13.

Table 13: Insulin mediated eNOS phosphorylation experiment samples and conditions

Sample:	Condition:	Size:
PAEC Control	PAEC Basal conditions	N = 2
PAEC Ins 3	3 minutes insulin stimulation	N = 2
BAEC Control	BAEC Basal conditions	N = 2
BAEC Ins 2	2 minutes insulin stimulation	N = 2
BAEC Ins 3	3 minutes insulin stimulation	N = 2
BAEC Ins 5	5 minutes insulin stimulation	N = 2

4.2.7 – Insulin Mediated eNOS Phosphorylation PBS vs. DMEM Experiment

This experiment determined if there was a difference in eNOS phosphorylation when samples were stimulated using PBS or serum free DMEM as a medium for the insulin. It was hypothesized that PBS would provide a higher P-eNOS signal by eliminating any interacting substances found in the DMEM.

Cells were seeded at P5-P9 into 60mm culture dishes at a concentration of 200,000 cells/dish and allowed to grow for 48 hours until 90-100% confluent. Cells were serum starved for 3 hours with 1% FBS in DMEM before insulin stimulation (see section 4.2.2 – Preparation and use of Insulin Solutions). For PBS samples, the media was aspirated, cells were washed with warm PBS, and then cells were given 4 mL of 100 nM insulin in warm PBS for 3 minutes. For DMEM samples, the media was aspirated, cells were then washed with warm PBS and given 4 mL of 100 nM insulin in serum free DMEM. Samples were lysed and quantified for p-eNOS, eNOS, and β-Actin using Western blot as described in section 4.2.4 – Western Blot Protein Quantification. A list of samples and conditions is shown in Table 14.

Table 14: Insulin mediated eNOS phosphorylation PBS vs. DMEM experiment samples and conditions

Sample:	Condition:	Size:
PBS Control	Basal conditions	N = 2
PBS Insulin	3 minutes 100 nM insulin in PBS	N = 2
DMEM Control	Basal conditions	N = 2
DMEM Insulin	3 minutes 100 nM insulin in serum free DMEM	N = 2

4.2.8 – FFA and Insulin Mediated eNOS Phosphorylation Experiment

This experiment determined the effects of FFAs on eNOS phosphorylation in a static BAEC culture stimulated with bovine insulin. It was hypothesized that FFAs would reduce eNOS phosphorylation in samples treated with insulin, as demonstrated in a study experiment by Kim et al. (Kim et al., 2005).

Cells were seeded at passage 5-9 into 60mm culture dishes at a concentration of 300,000 cells/dish and allowed to grow for 24-36 hours until 90-100% confluent. Sample media was changed 3 hours before testing to either serum free DMEM, or serum free DMEM with 10% BSA and 100 µM palmitic acid as described in section4.2.3 – Preparation and use of Free Fatty Acid Solutions. Images were taken after the 3 hour incubation at 4x magnification using a phase contrast microscope. DMEM was then removed and replaced with 4 mL of 100 µM insulin in warm PBS then incubated for 3 minutes at 37^{o}C as described in section 4.2.2 – Preparation and use of Insulin Solutions. Samples were washed and lysed according to the protocol described in section 4.2.4 – Western Blot Protein Quantification. A table listing the samples and experimental conditions is shown below in Table 15.

Table 15: FFA and Insulin Mediated eNOS Phosphorylation Experiment Samples and Conditions

Sample:	Description:	Size:
Control	Basal conditions	N = 3
Insulin	3 minutes with 100 nM insulin in PBS	N = 3
FFA	3 hours 100 µM palmitic acid	N = 3
Insulin + FFA	3 hours 100 µM palmitic acid , 3 minutes with 100 nM insulin in PBS	N = 3

4.2.9 – FFA and Flow Mediated eNOS Phosphorylation Experiment

This experiment determined if increased shear stress induced eNOS phosphorylation in the presence FFAs. It was hypothesized that increased shear stress would maintain eNOS phosphorylation despite the presence of FFAs.

Cells were seeded at passage 5-9 into 60mm culture dishes at a concentration of 300,000 cells/dish and allowed to grow for 24-36 hours until 90-100% confluent. The samples were treated with either serum free DMEM, or serum free DMEM with 100 µM palmitic acid for 3 hours as described in section 4.2.3 – Preparation and use of Free Fatty Acid Solutions. Images were taken before testing. Flow samples were subjected to moderate (20 dynes/cm^2) 5 minutes, a duration previously shown to consistently phosphorylate eNOS. Insulin samples were treated with 3 minute stimulation with 100 nM insulin in warm PBS as described in section 4.2.2 – Preparation and use of Insulin Solutions. Images were taken again after flow to confirm that cells were alive and attached. Samples were lysed and Western blot was performed according to section4.2.4 – Western Blot Protein Quantification. The experimental conditions are listed in Table 16.

Table 16: Flow mediated eNOS Phosphorylation in the presence of FFAs experiment samples and conditions

Sample:	Condition:	Size:
Control	Basal Conditions	N = 3
FFA	3 hours 100 µM palmitic acid	N = 3
Fluid Shear Stress	20 dynes/cm^2 for 5 minutes	N = 3
FFA + FSS	3 hours 100 µM palmitic acid , 20 dynes/cm^2 for 5 minutes	N = 3
Insulin	100 nM insulin in PBS for 3 minutes	N = 1

4.3 – Experimental Results

4.3.1 - Insulin Mediated eNOS Phosphorylation Results

This experiment compared p-eNOS, eNOS, and β-actin in BAECs and PAECs with insulin stimulation to determine the cell type and insulin stimulation duration to produce the highest p-eNOS signal. Western blot band density (Figure 69d) displayed a clear increase of p-eNOS in BAECs with insulin stimulation as compared to unstimulated controls. BAEC showed a 5-7 fold increase in p-eNOS compared to the BAEC control, and a 10+ fold increase in p-eNOS signal compared to PAEC (Figure 69a). The eNOS signal showed a 0.7 - 1.0 fold change with high variability (Figure 69b,d). β-actin displayed mean values between 1.0 -1.75 fold changes, and small variation within samples (Figure 69c).

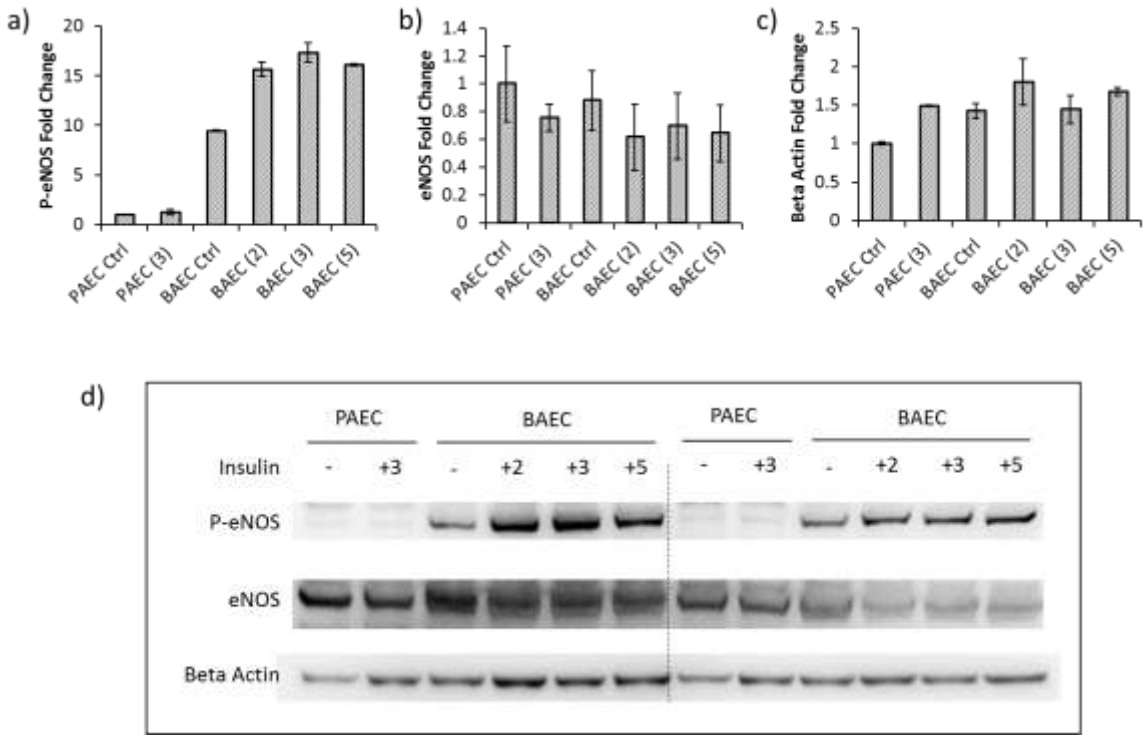

Figure 69: Insulin Mediated eNOS Phosphorylation Results comparing insulin stimulation duration and cell species, including a) p-eNOS fold change, b) eNOS fold change, c) β-actin fold change, and d) Western blot band density results

P-eNOS was normalized to total eNOS (Figure 70a) as well as to β-actin as loading control (Figure 70b). Statistical analysis using an unpaired t-test are shown in Figure 70b,d[M2] for p-eNOS/eNOS and p-eNOS/ β-actin respectively. The 10 fold change observed in p-eNOS/eNOS signal between PAEC samples and BAEC samples was statistically significant ($p = 0.0308$, Figure 70b). The 2-fold change between BAEC control samples and BAEC insulin stimulated samples normalized for p-eNOS/eNOS was statistically significant for 2, 3, and 5 minute stimulation durations (Figure 70a,b). P-eNOS/β-actin samples showed a significant ($p = 0.0094$) 6-fold change between PAEC control and BAEC control samples (Figure 70c,d). BAEC insulin stimulated samples showed an 8-fold, 10-fold, and 9-fold change increase compared to the PAEC control for BAEC 2, 3, and 5 minute insulin stimulated samples respectively. The

increase in P-eNOS/β-actin between BAEC control and BAEC insulin stimulated samples was found to be significant for 2, 3, and 5 minutes (Figure 70b,c).

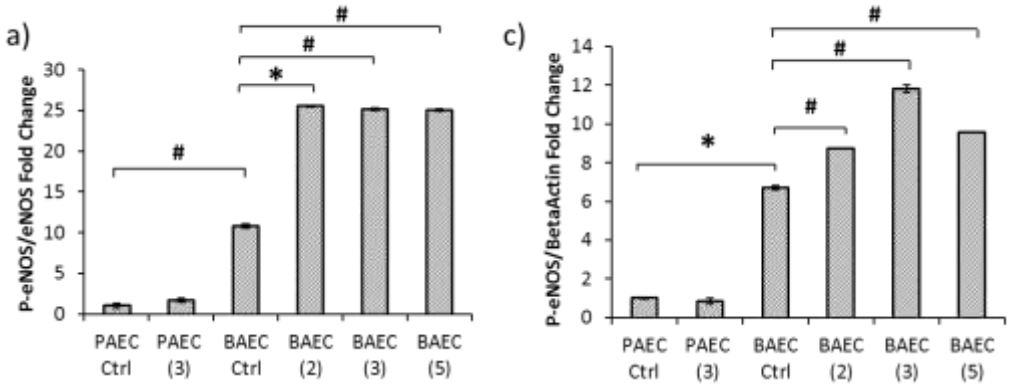

b)

Non-Paired T-test:	p =
PAEC Ctrl vs BAEC Ctrl	0.0308
BAEC Ctrl vs BAEC (2)	0.0098
BAEC Ctrl vs BAEC (3)	0.0215
BAEC Ctrl vs BAEC (5)	0.021

d)

Non-Paired T-test:	p =
PAEC Ctrl vs BAEC Ctrl	0.0094
BAEC Ctrl vs BAEC (2)	0.0344
BAEC Ctrl vs BAEC (3)	0.046
BAEC Ctrl vs BAEC (5)	0.0184

Figure 70: Insulin Mediated eNOS Phosphorylation Results for a) p-eNOS normalized to eNOS, b) P-eNOS normalized to β-Actin, c) Statistical analysis of p-eNOS/eNOS, d) Statistical Analysis of p-eNOS/β-actin

4.3.2 - Insulin Mediated eNOS Phosphorylation PBS vs. DMEM Experiment

This experiment compared eNOS phosphorylation with PBS or DMEM as a medium for insulin stimulation. Fold changes in p-eNOS, eNOS, and β-actin are shown in Figure 71a,b,c, with spot densitometry data quantified from the Western blot bands displayed in Figure 71d. P-eNOS was higher in PBS control and insulin stimulated samples (Figure 71a) . PBS samples also show a smaller variance between replicate samples compared to DMEM samples as evidenced by the

plotted standard deviation. PBS insulin stimulation showed a 1.6 fold increase in p-eNOS, while DMEM showed a reduced fold change with insulin stimulation as compared to the control. The eNOS signal displayed an inconsistent fold change of 0.8-1.6 which appeared to show an inverse behavior to the p-eNOS signal (Figure 71b,d). The β-actin showed a consistent 1.0-1.2 fold change, but with a higher standard deviation in PBS samples compared to DMEM samples (Figure 71c).

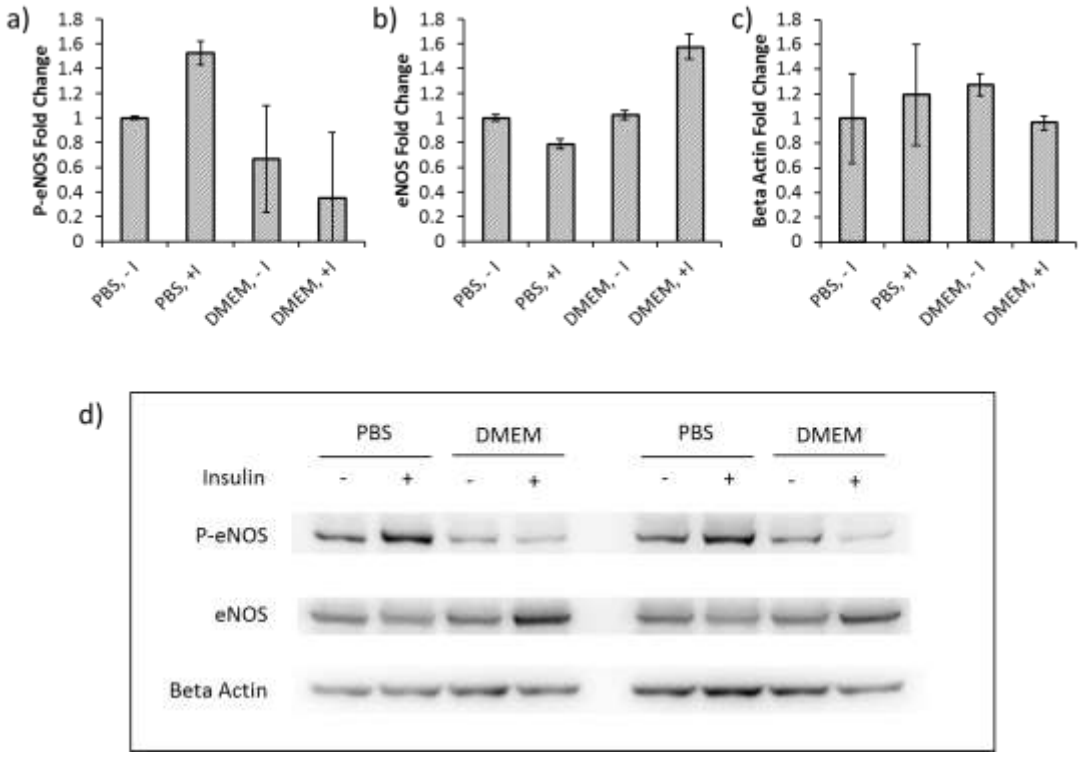

Figure 71: Insulin Mediated eNOS Phosphorylation PBS vs. DMEM Experiment Results, a) p-eNOS fold change, b) eNOS fold change, c) β-actin fold change, d) Western blot band density results

P-eNOS values were normalized to eNOS to determine the relative eNOS phosphorylation compared to the total available eNOS (Figure 72a). P-eNOS was also normalized to β-actin as loading control (Figure 72b). The statistical analysis is shown in Figure 72b,d using

an unpaired t-test. The p-eNOS/eNOS showed a significant 2-fold increase between PBS control and PBS insulin stimulation (p = 0.0078), while DMEM samples did not demonstrate a significant change between control and insulin stimulation (Figure 72a,b).[M3] The PBS insulin stimulated sample was statistically significantly different from the DMEM insulin stimulated group (P = 0.0047, Figure 72a,b). The p-eNOS normalized to β-actin did not display the same fold changes and significance was not found between the same groups compared in the p-eNOS/eNOS analysis (Figure 72c,d), though a similar trend was observed with PBS samples showing greater fold change of mean values compared to DMEM samples.

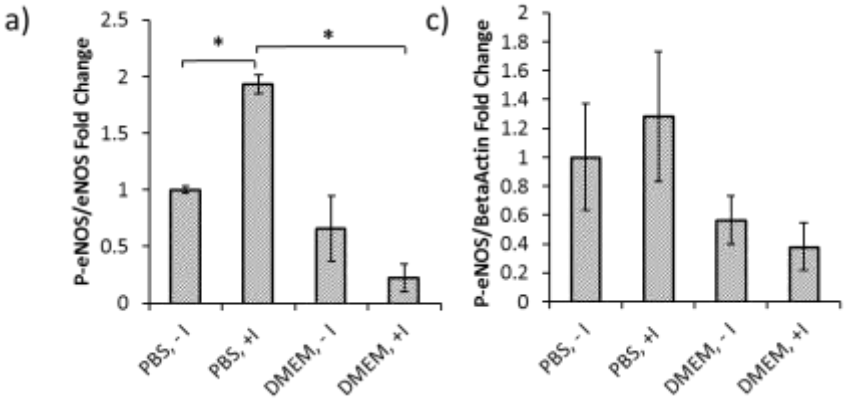

b)

Non-Paired T-test:	p =
PBS , -I vs PBS +I	0.0078
DMEM -I vs DMEM +I	0.0856
PBS -I vs DMEM -I	0.1274
PBS +I vs DMEM +I	0.0047

d)

Non-Paired T-test:	p =
PBS , -I vs PBS +I	0.3004
DMEM -I vs DMEM +I	0.1873
PBS -I vs DMEM -I	0.2104
PBS +I vs DMEM +I	0.1535

Figure 72: Insulin Mediated eNOS Phosphorylation PBS vs. DMEM Experiment Results, a) p-eNOS normalized to eNOS, b) statistical analysis of p-eNOS/eNOS, c) p-eNOS normalized to β-actin, d) statistical analysis of p-eNOS/β-actin

4.3.3- FFA and Insulin Mediated eNOS Phosphorylation Experiment

This experiment shows the effects of 3 hour FFA incubations on eNOS phosphorylation when BAEC were stimulated with insulin. An important distinction in this experiment compared to previous was the use of two separate Western blots for p-eNOS and eNOS, respectively. Therefore, two sets of β-actin were measured, one for each membrane to allow accurate loading control. The results of the Western blot spot densitometry are quantified in Figure 73a,b,c,d for p-eNOS, eNOS, β-actin of p-eNOS, and β-actin of eNOS respectively. The Western blot membrane showing band density is displayed in Figure 73e, with the β-actin bands located in the box corresponding to the membrane in which they originated. P-eNOS was 2.5-fold higher in the insulin stimulated sample as compared to control (Figure 73a,e). The FFA incubated control samples showed a similar mean value as compared to the non-FFA control group (Figure 73a,e). The FFA+insulin samples displayed a 2.25 fold increase compared to the control which was slightly lower than the insulin stimulated samples (Figure 73a,e). The eNOS signal was consistent, with a 1.0-0.8 range of fold changes, though with an increased variability in FFA samples compared to non-FFA samples (Figure 73b). The β-actin loading control was consistent for both mean values and standard deviation (Figure 73c,d,e).

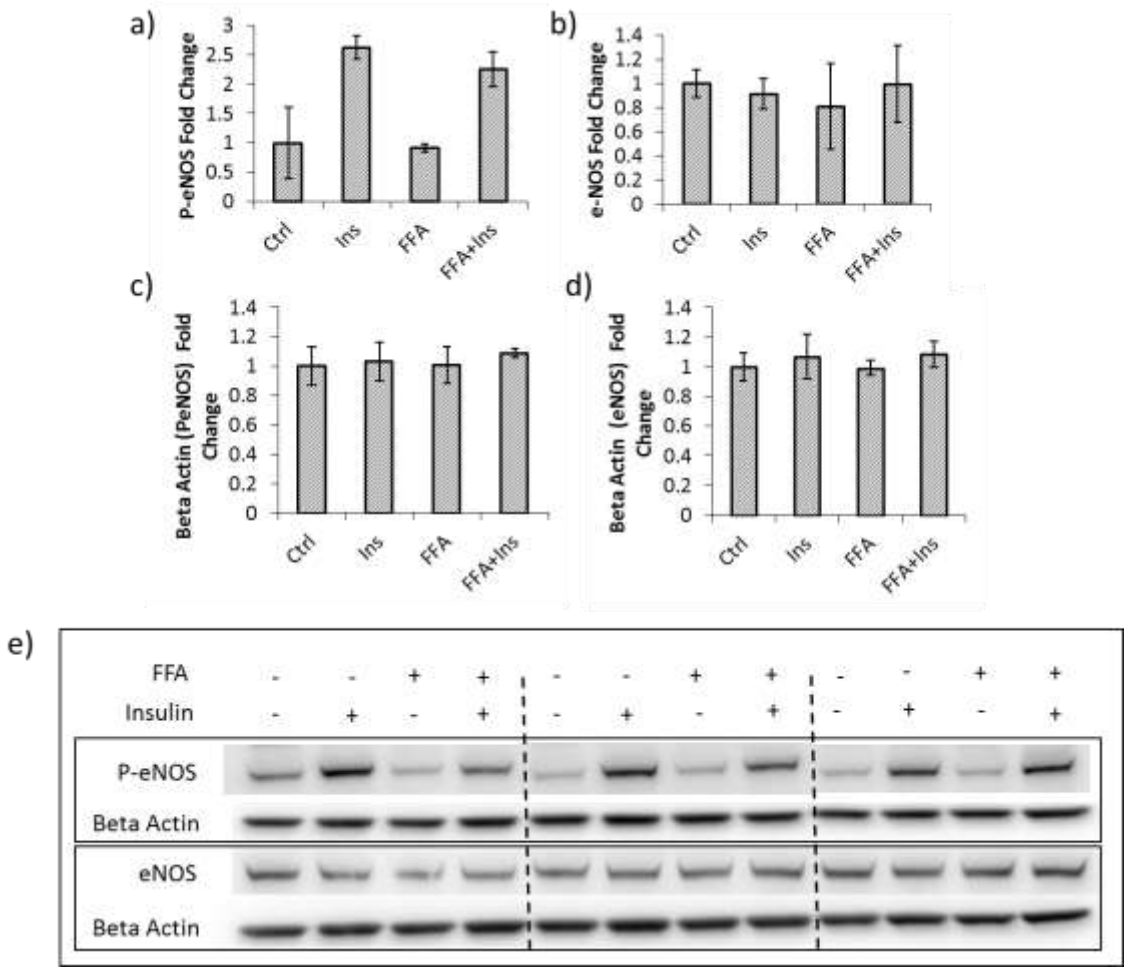

Figure 73: FFA and Insulin Mediated eNOS Phosphorylation Results, a) p-eNOS fold change, b) eNOS fold change, c) β-actin fold change for p-eNOS blot, d) β-actin fold change for eNOS blot, e) Western blot band results

P-eNOS was normalized to eNOS to show the relative phosphorylation of the total eNOS available and normalized to β-actin as loading control (Figure 74a,b). Additionally, p-eNOS was normalized to the β-actin value for the p-eNOS blot, then normalized to eNOS which was also normalized to the β-actin value for its blot (Figure 74c). This was intended to account for any loading inconsistencies due to performing the p-eNOS and eNOS on separate blots. The results of selected statistical analysis using unpaired t-test are shown in Figure 74e,f. The p-eNOS/eNOS

results show a statistically significant 2.8-fold increase between control and insulin stimulated samples, as well as a significant 2.2-fold increase for FFA+insulin samples compared to control. No significance was found between the non-FFA control and FFA control samples, which displayed a similar mean value (Figure 74a,d). The insulin and FFA+insulin samples showed a difference in mean value with 2.8 vs. 2.2 fold changes compared to control; however comparison of these groups did not yield a statistical significance (P = 0.0633, Figure 74a,d). Normalizing p-eNOS to β-actin and p-eNOS/eNOS/ β-actin provided similar results (Figure 74b,e, Figure 74c,f). It is likely that more samples are needed to show a statistically significant result.

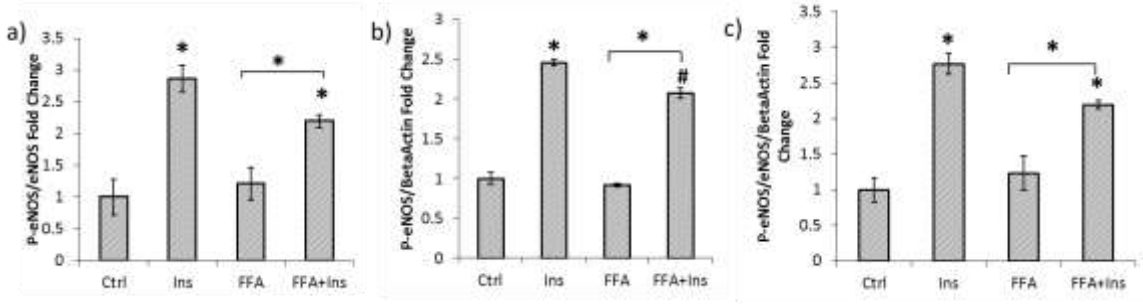

d)

Non-Paired T-test:	p =
Ctrl vs Ins	0.0045
Ctrl vs FFA	0.3134
Ctrl vs FFA+Ins	0.0025
Ins vs FFA+Ins	0.0633
FFA vs FFA+Ins	0.004

e)

Non-Paired T-test:	p =
Ctrl vs Ins	0.003
Ctrl vs FFA	0.2664
Ctrl vs FFA+Ins	0.0142
Ins vs FFA+Ins	0.0884
FFA vs FFA+Ins	0.0039

f)

Non-Paired T-test:	p =
Ctrl vs Ins	0.0024
Ctrl vs FFA	0.2642
Ctrl vs FFA+Ins	0.0009
Ins vs FFA+Ins	0.058
FFA vs FFA+Ins	0.0046

Figure 74: FFA and Insulin Mediated eNOS Phosphorylation Results, a) p-eNOS fold change normalized to eNOS, b) p-eNOS fold change normalized to β-actin, c) p-eNOS/β-actin fold change normalized to eNOS/ β-actin fold change, d) statistical analysis of p-eNOS/eNOS e) statistical analysis of p-eNOS/β-actin, f) statistical analysis of p-eNOS/eNOS/β-actin

This protocol was repeated in a second experiment using the same conditions and cell treatments. The trends in p-eNOS, eNOS, and β-actin were relatively consistent with the

previous experiment. P-eNOS was increased in insulin stimulated samples (Figure 75a,e). An inconsistency between this experiment and the previous experiment was the mean value of the FFA sample, which was 0.5-fold lower than the control sample. eNOS displayed a high standard deviation in the control sample (Figure 75b,e). The β-actin mean values was consistent and show a low fold change range of 1.0-0.8 for both the p-eNOS and eNOS membranes (Figure 75c,d).

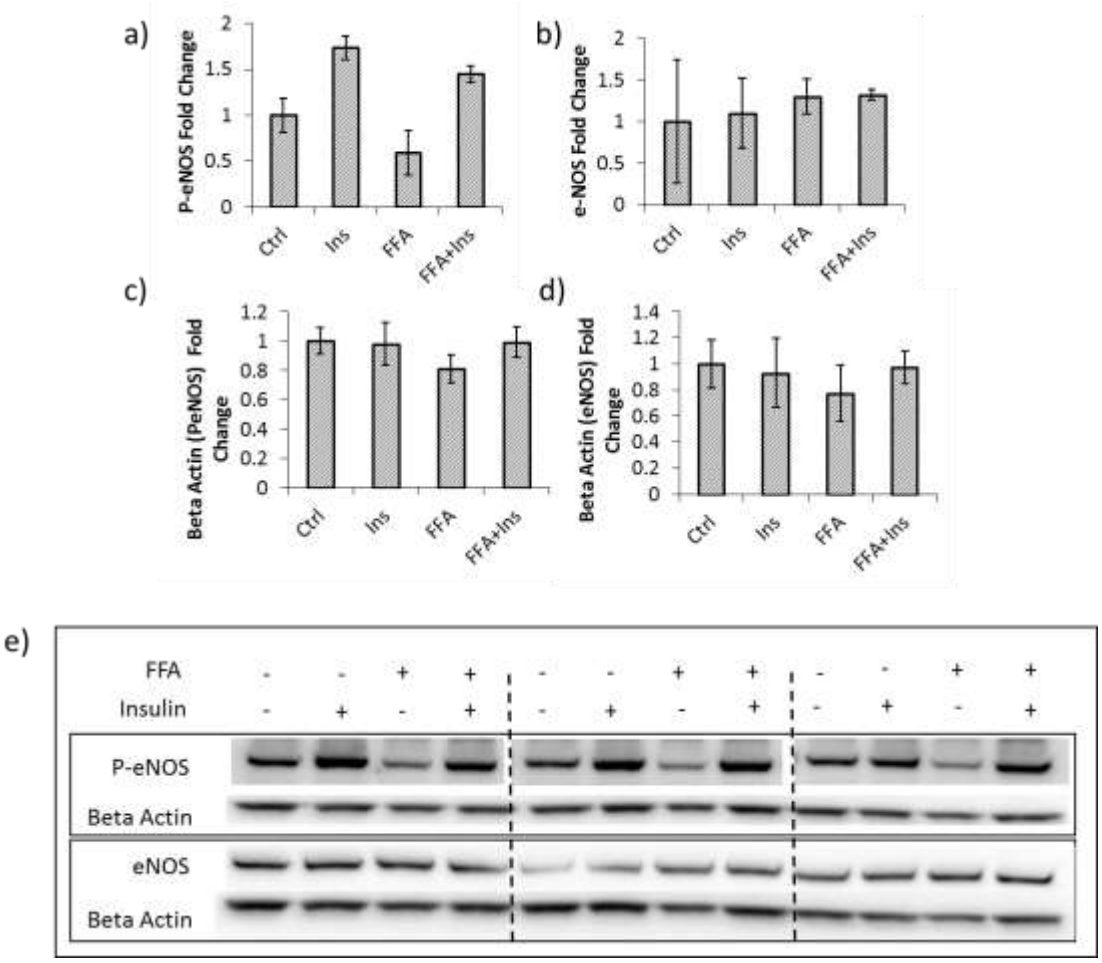

Figure 75: FFA and Insulin Mediated eNOS Phosphorylation Replicate Results, a) p-eNOS fold change, b) eNOS fold change, c) β-actin fold change for p-eNOS blot, d) β-actin fold change for eNOS blot, e) Western blot band results

The p-eNOS/eNOS normalized group showed statistically significant change between the insulin and FFA+insulin samples (p=0.0443) to support the 1.6 vs. 1.2-fold change observed (Figure 76a,d). Statistical significance was also found between the control and the FFA-treated sample (P = 0.0367), which was inconsistent with the previous experiment (Figure 76a,d). Normalization of p-eNOS to β-actin showed statistically significant differences between insulin-treated, FFA-treated, and FFA+Insulin treated samples as compared to control. Furthermore, the mean fold change between insulin and FFA+insulin samples (1.8 vs. 1.4) was significant (p = 0.0439, Figure 76b,e). Normalization of p-eNOS/eNOS after normalizing each to the respective β-actin values varied from the previous experiment, showing significance only between the control vs. FFA and FFA vs. FFA+insulin samples (Figure 76c,f).

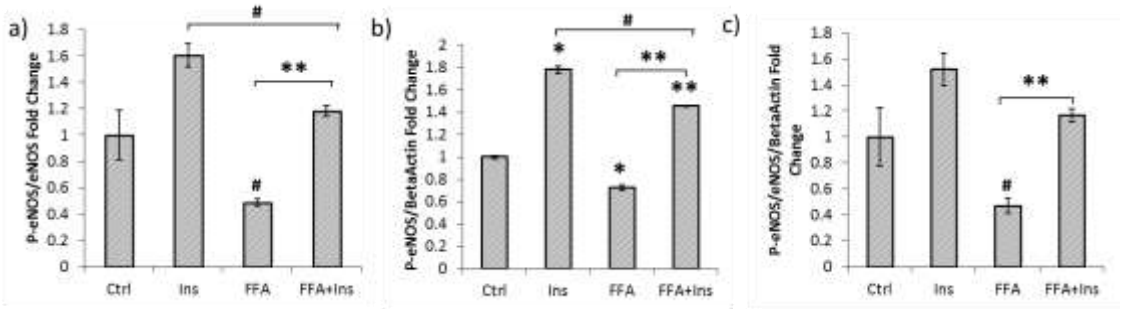

d)

Non-Paired T-test:	p =
Ctrl vs Ins	0.0702
Ctrl vs FFA	0.0367
Ctrl vs FFA+Ins	0.3408
Ins vs FFA+Ins	0.0443
FFA vs FFA+Ins	0.0003

e)

Non-Paired T-test:	p =
Ctrl vs Ins	0.0034
Ctrl vs FFA	0.0043
Ctrl vs FFA+Ins	0.0002
Ins vs FFA+Ins	0.0439
FFA vs FFA+Ins	< 0.0001

f)

Non-Paired T-test:	p =
Ctrl vs Ins	0.1229
Ctrl vs FFA	0.0433
Ctrl vs FFA+Ins	0.395
Ins vs FFA+Ins	0.088
FFA vs FFA+Ins	0.0005

Figure 76: FFA and Insulin Mediated eNOS Phosphorylation Replicate Results, a) p-eNOS fold change normalized to eNOS, b) p-eNOS fold change normalized to β-actin, c) p-eNOS/β-actin fold change normalized to eNOS/β-actin fold change, d) statistical analysis of p-eNOS/eNOS e) statistical analysis of p-eNOS/β-actin, f) statistical analysis of p-eNOS/eNOS/β-actin

4.3.4 - FFA and Flow Mediated eNOS Phosphorylation Results

This experiment was intended to demonstrate that fluid shear stress will increase eNOS phosphorylation to offset the inhibition caused by FFAs. The P-eNOS shows a reduction between the control and FFA sample, which is consistent with the static samples in the previous experiments. The Flow shows a 1.7 increase in P-eNOS, while FFA+flow shows a lower 1.5 fold increase in P-eNOS compared to the control (Figure 77a). eNOS shows a 1.0 to 0.5 fold change variation (Figure 77b). Beta actin shows consistent loading throughout, though the western blot appear to show some variability likely due to background variation in the membrane (Figure 77c,d). P-eNOS results appear consistent in the second and third group of samples, however the first group demonstrates a higher P-eNOS for the FFA+flow than the flow sample Figure 77e.

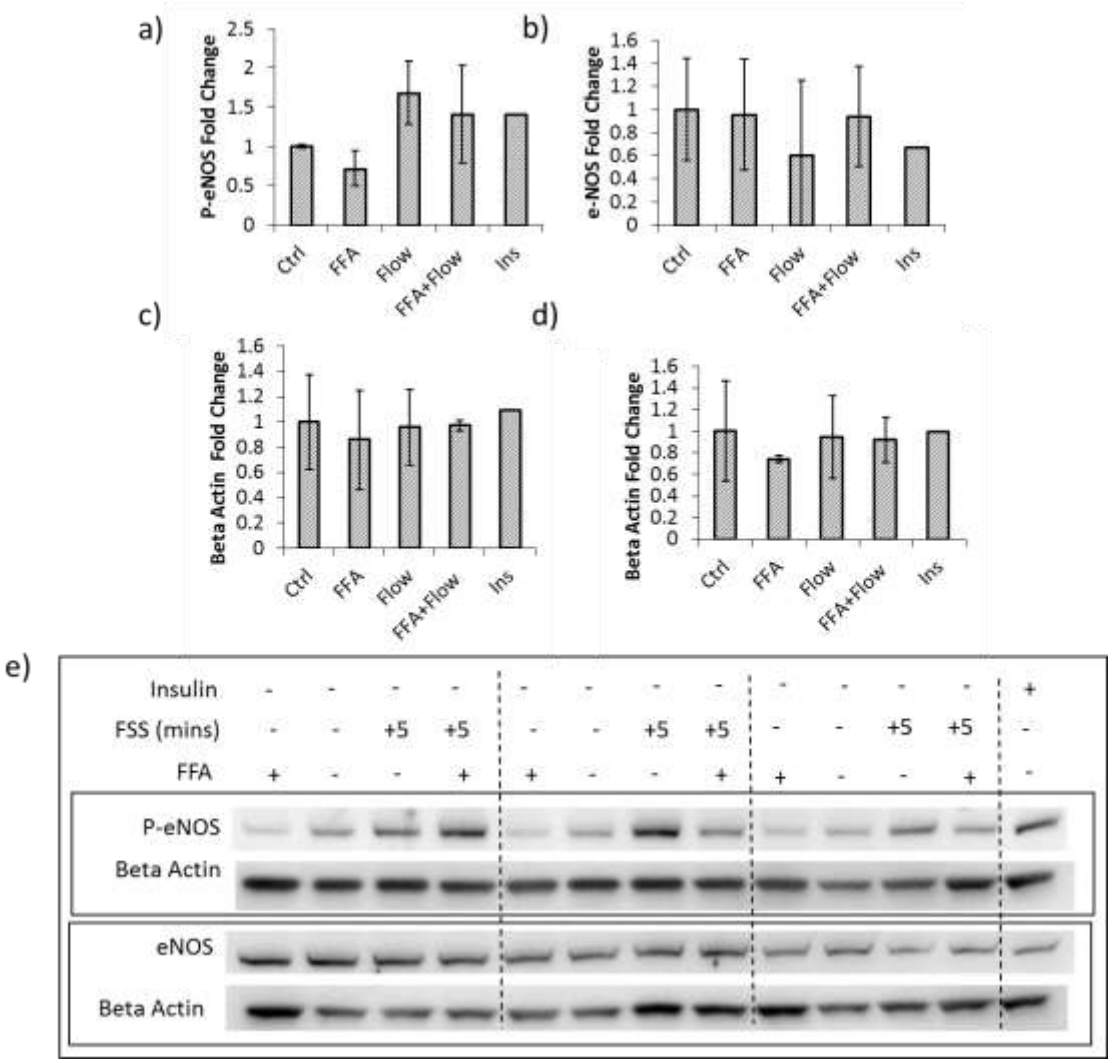

Figure 77: FFA and Flow Mediated eNOS Phosphorylation Results, a) p-eNOS fold change, b) eNOS fold change, c) β-actin fold change for p-eNOS blot, d) β-actin fold change for eNOS blot, e) Western blot band results

When p-eNOS is normalized to eNOS, a statistical significance is displayed between the static and flow samples, as well as the FFA+flow groups indicating that both groups significantly increased eNOS phosphorylation. Statistical significance was also found between the FFA and FFA+flow sample, with a 0.75 to 1.5 fold change demonstrating an increase in eNOS phosphorylation between FFA samples without and with flow, respectively. Furthermore, no

significance was found between the flow samples and the FFA+flow samples, though the average value for FFA+flow was lower. (Figure 78a,d). P-eNOS normalized to beta actin showed a somewhat similar trend in the average values, however only produced statistical significance for the flow sample compared to the static control sample (Figure 78b,e). P-eNOS normalized to eNOS and beta actin showed a similar trend as the two previous datasets, however not statistical significance was displayed (Figure 78c,f).

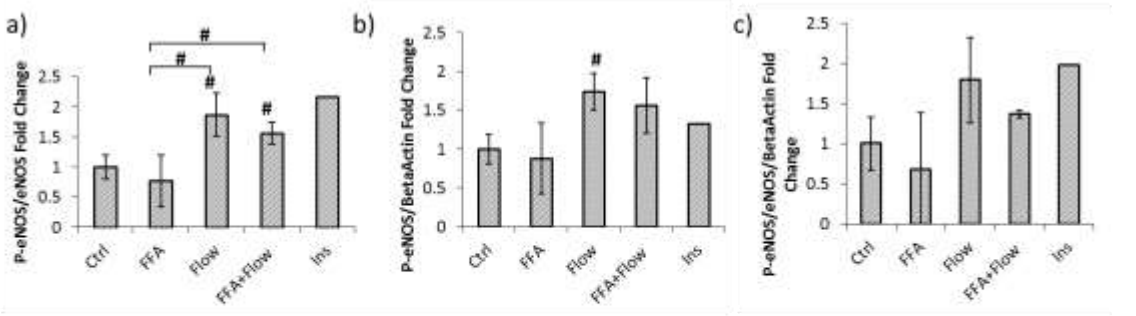

d)

Unpaired T-test	p =
Ctrl vs FFA	0.4282
Ctrl vs. Flow	0.0497
Ctrl vs. FFA+Flow	0.0423
FFA vs. FFA+Flow	0.0313
Flow vs. FFA+Flow	0.3787
FFA vs. Flow	0.0354

e)

Unpaired T-test	p =
Ctrl vs FFA	0.682
Ctrl vs. Flow	0.0416
Ctrl vs. FFA+Flow	0.2121
FFA vs. FFA+Flow	0.0994
Flow vs. FFA+Flow	0.4754

f)

Unpaired T-test	p =
Ctrl vs FFA	0.5258
Ctrl vs. Flow	0.1237
Ctrl vs. FFA+Flow	0.1289
FFA vs. FFA+Flow	0.0845
Flow vs. FFA+Flow	0.3903

Figure 78: FFA and Flow Mediated eNOS Phosphorylation Results, a) p-eNOS fold change normalized to eNOS, b) p-eNOS fold change normalized to β-actin, c) p-eNOS/β-actin fold change normalized to eNOS/β-actin fold change, d) statistical analysis of p-eNOS/eNOS e) statistical analysis of p-eNOS/β-actin, f) statistical analysis of p-eNOS/eNOS/β-actin

4.4 – Discussion

BAECs showed a greater increased in eNOS phosphorylation in response to insulin as compared to PAECs. Furthermore, the BAEC p-eNOS signal increase in response to insulin was statistically significant for all insulin stimulation durations when normalized to both eNOS and β-actin. For these reasons, BAECs were selected for the remainder of experiments. The insulin

stimulation time of 3 minutes showed a peak in p-eNOS when normalized to β-actin. From this result, 3 minutes was selected for insulin stimulation time. A limitation of this experiment may be the inconsistency in eNOS and β-actin seen in the Western blot and quantification. The eNOS appeared to have a slight inverse relationship with p-eNOS, which has not been observed in the literature. This trend may affect the normalization, as total eNOS is expected to be consistent and independent of p-eNOS levels. The β-actin variance affected p-eNOS normalization; however this did not confound the data. The higher intensity bands correspond to the high p-eNOS samples and low intensity bands correspond to the lower p-eNOS signals, meaning that normalization actually decreased relative changes among the samples. This indicates that fold changes in p-eNOS/β-actin may actually be higher than represented in the data. It is unclear whether this variance is a result of protein during gel loading, or if it a poor transfer of proteins from the gel to the membrane. The association of the darkest p-eNOS bands with the darkest β-actin bands (lanes 3,4,5 Figure 69d) implies that the data normalization is accurate, and loading may be inconsistent.

Comparison of PBS vs. DMEM for insulin stimulation showed that eNOS was more effectively phosphorylated in PBS. This observation supported the decision to use PBS as the insulin stimulation medium in all following experiments. The eNOS and β-actin exhibited some variance in this experiment, similar to that discussed in the previous experiment. The eNOS signal displayed a slight inverse trend compared to p-eNOS. This suggests that the eNOS values may not reflect the total cellular eNOS but may be affected by p-eNOS antibody or incomplete membrane stripping. The β-actin followed a similar trend, but like the previous experiment the high β-actin corresponded with higher p-eNOS. The β-actin variance is attributed to inconsistent proteins loading during Western blot.

FFA incubation had mixed effects on insulin stimulation of eNOS phosphorylation. Two experiments were presented, and both displayed the hypothesized changes in eNOS phosphorylation due to insulin, FFA, and FFA+insulin treatments. Visual examination of the Western blot band density agreed with results presented by Kim et al., showing that FFAs inhibited eNOS phosphorylation due to insulin (Kim et al., 2005). Quantification and statistical analysis of the data, however, only supports the hypothesis in the second experiment. It is likely that more samples are needed to consistently show a statistically significant difference. The number of samples required could be determined using a power analysis.

FFA and flow mediated eNOS phosphorylation shows promising preliminary results, however only 2 of the 3 sample groups showed results that were consistent with the hypothesis. As expected, samples displayed an increase in p-eNOS after application of fluid shear stress, and a reduction with FFAs. In two of the three samples, the FFA+flow group displayed a greater eNOS phosphorylation than control and FFA samples, but lower levels that the flow group. In one sample group, the p-eNOS was higher in the FFA+flow group. It is unclear why this occurred, and may be a result of the sample receiving higher shear stress than expected or a lower FFA concentration. Additional experiments are required to determine which sample groups display the accurate data.

The experiments presented here provide effective preliminary data for performing the proposed shear stress experiments in the presence of FFA and fluid shear stress. The results indicate that the experimental and Western blot techniques used here are sufficient for detecting changes in p-eNOS. Some limitations exist among all experiments, including the variation observed in total eNOS levels and β-actin loading controls, and the small sample size of the experiments. Additional replicate experiments may be able to show a greater statistical significance for the effects of FFA incubation on insulin and flow stimulation.

Chapter 5: Conclusions and Future Work

5.1 – Conclusions

In conclusion, this thesis provides the design of an effective cone and plate system with promising capabilities for 3D hydrogel co-cultures. As a stand-alone system for subjecting cells to FSS, the cone and plate system produced cell alignment in chronic flow and eNOS phosphorylation in acute flow. For applications requiring FSS at 24 hours or less, this design provides significant advantages over parallel plate flow chambers and microfluidic devices when high throughput and protein quantification are required. Further work may also be required to investigate the use of culture dishes as a flow substrate for endothelial cells. While this has been shown to suffice in devices seen in the literature, some variability may be arising from the use of these dishes.

The gel co-culture shows proof of concept; however, more work will be needed before it can be implemented. The gel detection system performed well. The main shortcoming was the inability to produce a molded gel with a flat surface for consistent Couette flow in the cone and plate device. Gel molding appears to be a promising method, but different materials and higher fabrication tolerances will be needed to produce a flat gel with fine enough dimensional tolerances for cone and plate flow testing.

This thesis established preliminary data for studying the effects of FFAs on eNOS phosphorylation in flow. Protocols for p-eNOS and eNOS Western blot quantification were established and validated, as well as procedures for treating BAECs with FFAs and insulin. Initial flow validation test also provided baseline data on eNOS phosphorylation that assisted in selecting the time point for future experiments. While the data suggest that FFAs inhibit eNOS phosphorylation in response to insulin as hypothesized, additional experiments are needed to

confirm this behavior. BAECs with FFA incubation subjected to fluid shear stress show promising preliminary results that suggest flow can correct FFA mediated p-eNOS inhibition, though this was only displayed in 2 of 3 sample groups.

5.2 - Future Work

The first step to further this work would be to conduct additional experiments of FFAs in flow to test the final hypothesis of this thesis. The gelatin molding must be further explored and validated to improve the surface flatness before an effective co-culture can be created. Finally, an adipocyte-endothelial co-culture would provide the next step in increasing the physiological relevance of the system (Figure 79). This would allow experimentation with inflammation in the endothelial and adipose tissue, and help further knowledge of how flow plays a role in the interaction between the adipose tissue and the vasculature.

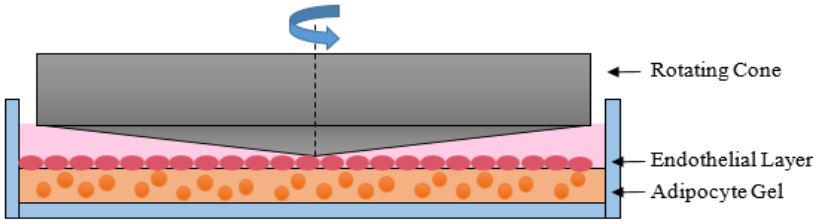

Figure 79: Adipocyte-endothelial co-culture for cone and plate device

List of References

Alberts, B., Johnson, A., & Lewis, J. (2002). *Molecular Biology of the Cell* (4th ed.). New York: Garland Science.

Albrecht, E. W. J. a, Stegeman, C. a, Heeringa, P., Henning, R. H., & van Goor, H. (2003). Protective role of endothelial nitric oxide synthase. *The Journal of Pathology*, *199*(1), 8–17. http://doi.org/10.1002/path.1250

Ando, J., & Yamamoto, K. (2009). Vascular Mechanobiology. *Circulation Journal*, *73*(11), 1983–1992. http://doi.org/10.1253/circj.CJ-09-0583

Ando, T., Komatsuda, T., & Kamiya, A. (2016). Cytoplasmic Calcium Response to Fluid Shear Stress in Cultured Vascular Endothelial Cells Author (s): Joji Ando , Teruhiko Komatsuda and Akira Kamiya Source : In Vitro Cellular & Developmental Biology , Vol . 24 , No . 9 (Sep ., 1988), pp . 871-877 Pu. *In Vitro Cellular & Developmental Biology*, *24*(9), 871–877.

Ballard, K. W. (1978). Functional characteristics of the microcirculation in white adipose tissue. *Microvascular Research*, *16*(1), 1–18.

Bartheld, Robert G. Dippery, R. E., Kao, C., Richard, N., Johnson, J. H., Mullen, D. M., Dymond, J. H., … Dubey, C. K. (2004). *Handbook of Electric Motors*. (H. A. Toliyat, Ed.).

Bhatia, S. N., & Ingber, D. E. (2014). Microfluidic organs-on-chips. *Nature Biotechnology*, *32*(8), 760–772. http://doi.org/10.1038/nbt.2989

Blackman, B. R., Barbee, K. a., & Thibault, L. E. (2000). In vitro cell shearing device to investigate the dynamic response of cells in a controlled hydrodynamic environment. *Annals of Biomedical Engineering*, *28*(4), 363–372. http://doi.org/10.1114/1.286

Blackman, B. R., & Wamhoff, B. R. (2014). USE OF AN IN VITRO HEMODYNAMIC ENDOTHELIAL/SMOOTH MUSCLE CELL CO-CULTURE MODEL TO IDENTIFY NEW THERAPEUTIC TARGETS FOR VASCULAR DISEASE. United States.

Boden, G. (2008). Obesity and Free Fatty Acids. *Endocrinology and Metabolism Clinics of North America*, *37*(3), 635–646. http://doi.org/10.1016/j.ecl.2008.06.007

Boden, G., Chen, X., Ruiz, J., White, J. V, & Rossetti, L. (1994). Mechanism of fatty acid-induced inhibition of glucose uptake. *J Clin Invest*, *93*, 2438–2446. http://doi.org/10.1172/JCI117252

Buschmann, M. H. (2002). A solution for the flow between a cone and a plate at low Reynolds number. *Journal of Thermal Science*, *11*(4), 289–295. http://doi.org/10.1007/s11630-002-0041-1

Buschmann, M. H., Dieterich, P., Adams, N. a., & Schnittler, H. J. (2005). Analysis of flow in a cone-and-plate apparatus with respect to spatial and temporal effects on endothelial cells. *Biotechnology and Bioengineering*, *89*(5), 493–502. http://doi.org/10.1002/bit.20165

Bussolari, S. R., Dewey, C. F., & Gimbrone, M. A. (1982). Apparatus for subjecting living cells to fluid shear stress. *Review of Scientific Instruments*, *53*(12), 1851–1854. http://doi.org/10.1063/1.1136909

Carmeliet, P. (2000). Mechanisms of angiogenesis and arteriogenesis. *Nature Medicine*, *6*(4), 389–395. http://doi.org/10.1038/74651

Choi, J. H., Bellas, E., Gimble, J. M., Vunjak-Novakovic, G., & Kaplan, D. L. (2011). Lipolytic function of adipocyte/endothelial co-cultures. Tissue Engineering.

Choi, J. H., Gimble, J. M., Vunjak-Novakovic, G., & Kaplan, D. L. (2010). Effects of Hyperinsulinemia on Lypolytic Function of Three-Dimensional Adipocyte/Endothelial Co-Cultures. Tissue Engineering.

Chung, B. G., Lee, K.-H., Khademhosseini, A., & Lee, S.-H. (2012). Microfluidic fabrication of microengineered hydrogels and their application in tissue engineering. *Lab on a Chip*, *12*(1), 45. http://doi.org/10.1039/c1lc20859d

Chung, K. R., & Dai, G. (2013). Design a Dynamic Flow Co-culture System to Investigate the Effect of Biomechanical Force Found in Vascular Niche on Cell Functions. *2013 39th Annual Northeast Bioengineering Conference*, (Figure 2), 213–214. http://doi.org/10.1109/NEBEC.2013.11

Coppack, S. W., Jensen, M. D., & Miles, J. M. (1994). In vivo regulation of lipolysis in humans, *35*, 177–193.

Cousin, S. P., Hügl, S. R., Wrede, C. E., Kajio, H., Myers, M. G., & Rhodes, C. J. (2001). Free Fatty Acid-Induced Inhibition of Glucose and Acid Synthesis in the Pancreatic Beta-Cell Line INS-1. *Endocrinology*, *142*(1), 229–240.

Cutler, D. M., Glaeser, E. L., & Shapiro, J. M. (2003). Why Have Americans Become More Obese? *Journal of Economic Perspectives*, *17*(3), 93–118. http://doi.org/10.1257/089533003769204371

Dahlin, R. L., Gershovich, J. G., Kasper, F. K., & Mikos, A. G. (2014). Flow perfusion co-culture of human mesenchymal stem cells and endothelial cells on biodegradable polymer scaffolds. *Annals of Biomedical Engineering*, *42*(7), 1381–1390. http://doi.org/10.1007/s10439-013-0862-y

Davies, P. F. (2015). Flow mediated endothelial mechanotransduction. *Physiological Reviews*, *3*(July 1995), 1–49.

Davis, C. a., Zambrano, S., Anumolu, P., Allen, A. C. B., Sonoqui, L., & Moreno, M. R. (2015). Device-Based In Vitro Techniques for Mechanical Stimulation of Vascular Cells: A Review. *Journal of Biomechanical Engineering*, *137*(4), 040801. http://doi.org/10.1115/1.4029016

De Boer, A. a, Monk, J. M., & Robinson, L. E. (2014). Docosahexaenoic acid decreases pro-inflammatory mediators in an in vitro murine adipocyte macrophage co-culture model. *PloS One*, *9*(1), e85037. http://doi.org/10.1371/journal.pone.0085037

Defining Adult Overweight and Obesity. (2012). Retrieved from http://www.cdc.gov/nccdphp/dnpa/healthyweight/assessing/bmi/childrens_BMI/about_childrens_BMI.htm

Dejana, E. (1996). Endothelial adherens junctions: implications in the control of vascular permeability and angiogenesis. *The Journal of Clinical Investigation*, *98*(9), 1949–1953. http://doi.org/10.1172/JCI118997

Dimitriadis, G., Lambadiari, V., Mitrou, P., Maratou, E., Boutati, E., Panagiotakos, D. B., … Raptis, S. a. (2007). Impaired Postprandial Blood Flow in Adipose Tissue May Be an Early Marker of Insulin Resistance in Type 2 Diabetes. *Diabetes Care*, *30*(12), 3128–3130. http://doi.org/10.2337/dc07-0699

Dimmeler, S., Fleming, I., Fisslthaler, B., Hermann, C., Busse, R., & Zeiher, a M. (1999). Activation of nitric oxide synthase in endothelial cells by Akt-dependent phosphorylation. *Nature*, *399*(6736), 601–605. http://doi.org/10.1038/21224

Finkelstein, E. a., & Strombotne, K. L. (2010). The economics of obesity. *American Journal of Clinical Nutrition*, *91*(5), 1520–1524. http://doi.org/10.3945/ajcn.2010.28701E

Finkelstein, E. A., Trogdon, J. G., Cohen, J. W., & Dietz, W. (2009). Annual medical spending attributable to obesity: Payer-and service-specific estimates. *Health Affairs*, *28*(5). http://doi.org/10.1377/hlthaff.28.5.w822

Galie, P. a., van Oosten, a., Chen, C. S., & Janmey, P. a. (2015). Application of multiple levels of fluid shear stress to endothelial cells plated on polyacrylamide gels. *Lab Chip*, *15*(4), 1205–1212. http://doi.org/10.1039/C4LC01236D

Goossens, G. H. (2008). The role of adipose tissue dysfunction in the pathogenesis of obesity-related insulin resistance. *Physiology and Behavior*, *94*(2), 206–218. http://doi.org/10.1016/j.physbeh.2007.10.010

Grundy, S. M., Brewer, H. B., Cleeman, J. I., Smith, S. C., & Lenfant, C. (2004). Definition of Metabolic Syndrome: Report of the National Heart, Lung, and Blood Institute/American Heart Association Conference on Scientific Issues Related to Definition. *Circulation*, *109*(3), 433–438. http://doi.org/10.1161/01.CIR.0000111245.75752.C6

Hagyoung, J., & Choi, K. (2009). Three-dimensional adipocyte/endothelial co- cultures for adipose tissue engineering, (November).

Harrison, H. R. (1997). *Advanced Engineering Dynamics*. London: Wiley.

He, J., Chen, R., Lu, Y., Zhan, L., Liu, Y., Li, D., & Jin, Z. (2016). Fabrication of circular microfluidic network in enzymatically-crosslinked gelatin hydrogel. *Materials Science and Engineering: C*, *59*, 53–60. http://doi.org/10.1016/j.msec.2015.09.104

Hebebrand, J., & Hinney, A. (2015). Obesity and overweight. Retrieved from http://www.who.int/mediacentre/factsheets/fs311/en/

Hotamisligil, G., Shargill, N., & Spiegelman, B. (1993). Adipose Expression of Tumor Necrosis Factor α : Direct Role in Obesity-Linked Insulin Resistance. *Science*, *259*(5091), 87–91. Retrieved from http://www.sciencemag.org/content/259/5091/87.short

Hughes, Austin Drury, B. (2013). *Electric Motors and Drives - Fundamentals, Types and Applications*. Elsevier. Retrieved from http://app.knovel.com/hotlink/toc/id:kpEMDFTA01/electric-motors-drives/electric-motors-drives

Ignarro, L. J., Buga, G. M., Wood, K. S., Byrns, R. E., & Chaudhuri, G. (1987). Endothelium-derived relaxing factor produced and released from artery and vein is nitric oxide. *Proceedings of the National Academy of Sciences*, *84*(24), 9265–9269. http://doi.org/10.1073/pnas.84.24.9265

Jansson, P. a, Larsson, a, & Lönnroth, P. N. (1998). Relationship between blood pressure, metabolic variables and blood flow in obese subjects with or without non-insulin-dependent diabetes mellitus. *European Journal of Clinical Investigation*, *28*(10), 813–818.

Kabirian, F., Amoabediny, G., Haghighipour, N., Salehi-Nik, N., & Zandieh-Doulabi, B. (2014). Nitric oxide secretion by endothelial cells in response to fluid shear stress, aspirin, and temperature. *Journal of Biomedical Materials Research. Part A*, 1231–1237. http://doi.org/10.1002/jbm.a.35233

Karpe, F., Fielding, B. a., Ilic, V., Macdonald, I. a., Summers, L. K. M., & Frayn, K. N. (2002). Impaired Postprandial Adipose Tissue Blood Flow Response Is Related to Aspects of Insulin Sensitivity . *Diabetes*, *51*(8), 2467–2473. http://doi.org/10.2337/diabetes.51.8.2467

Kemeny, S. F., Figueroa, D. S., & Clyne, A. M. (2013). Hypo- and Hyperglycemia Impair Endothelial Cell Actin Alignment and Nitric Oxide Synthase Activation in Response to Shear Stress. *PLoS ONE*, *8*(6). http://doi.org/10.1371/journal.pone.0066176

Kiess, W., Petzold, S., Töpfer, M., Garten, A., Blüher, S., Kapellen, T., … Kratzsch, J. (2008). Adipocytes and adipose tissue. *Best Practice and Research in Clinical Endocrinology and Metabolism*, *22*(1), 135–153. http://doi.org/10.1016/j.beem.2007.10.002

Kim, F., Tysseling, K. a, Rice, J., Pham, M., Haji, L., Gallis, B. M., … Raines, E. W. (2005). Free fatty acid impairment of nitric oxide production in endothelial cells is mediated by IKKbeta.

Arteriosclerosis, Thrombosis, and Vascular Biology, *25*(5), 989–994. http://doi.org/10.1161/01.ATV.0000160549.60980.a8

Klöting, N., Fasshauer, M., Dietrich, A., Kovacs, P., Schön, M. R., Kern, M., … Physiol, A. J. (2010). Insulin-sensitive obesity, 506–515. http://doi.org/10.1152/ajpendo.00586.2009.

Lafontan, M. (2014). Adipose tissue and adipocyte dysregulation. *Diabetes and Metabolism*, *40*(1), 16–28. http://doi.org/10.1016/j.diabet.2013.08.002

Lakka, H. M., Laaksonen De Fau - Lakka, T. a, Lakka Ta Fau - Niskanen, L. K., Niskanen Lk Fau - Kumpusalo, E., Kumpusalo E Fau - Tuomilehto, J., Tuomilehto J Fau - Salonen, J. T., … Jama. (2002). The metabolic syndrome and total and cardiovascular disease mortality in middle-aged men, *288*(0098-7484 (Print)), 2709–2716.

Lamberti, G., Prabhakarpandian, B., Garson, C., Smith, A., Pant, K., Wang, B., & Kiani, M. F. (2014). Bioinspired microfluidic assay for in vitro modeling of leukocyte-endothelium interactions. *Analytical Chemistry*, *86*(16), 8344–51. http://doi.org/10.1021/ac5018716

Large, V., Peroni, O., Letexier, D., Ray, H., & Beylot, M. (2004). Metabolism of lipids in human white adipocyte. *Diabetes & Metabolism*, *30*(4), 294–309. http://doi.org/10.1016/S1262-3636(07)70121-0

Malek, A. M., Ahlquist, R., Gibbons, G. H., Dzau, V. J., & Izumo, S. (1995). A cone-plate apparatus for the in vitro biochemical and molecular analysis of the effect of shear stress on adherent cells. *Methods in Cell Science*, 165–176.

Manolopoulos, K. N., Karpe, F., & Frayn, K. N. (2010). Gluteofemoral body fat as a determinant of metabolic health. *International Journal of Obesity*, *34*(6), 949–959. http://doi.org/10.1038/ijo.2009.286

Michiels, C. (2003). Endothelial cell functions. *Journal of Cellular Physiology*, *196*(3), 430–443. http://doi.org/10.1002/jcp.10333

Moncada, S., Palmer, R. M. J., & Higgs, E. A. (1991). Nitric Oxide: Physiology, Pathophysiology, and Pharmacology. *Pharmacological Reviews*, *43*(2).

Mottillo, S., Filion, K. B., Genest, J., Joseph, L., Pilote, L., Poirier, P., … Eisenberg, M. J. (2010). The metabolic syndrome and cardiovascular risk: A systematic review and meta-analysis. *Journal of the American College of Cardiology*, *56*(14), 1113–1132. http://doi.org/10.1016/j.jacc.2010.05.034

Muller, W. a. (2002). Leukocyte-endothelial cell interactions in the inflammatory response. *Laboratory Investigation; a Journal of Technical Methods and Pathology*, *82*(5), 521–533. http://doi.org/10.1038/labinvest.3780446

Munson, B. R., Okiishi, T. H., Huebsch, W. W., & Rothmayer, A. P. (2013). *Fundamentals of Fluid Mechanics* (7th ed.). Wiley.

Noris, M., Morigi, M., Donadelli, R., Aiello, S., Foppolo, M., Todeschini, M., … Remuzzi, a. (1995). Nitric oxide synthesis by cultured endothelial cells is modulated by flow conditions. *Circulation Research*, *76*(4), 536–543. http://doi.org/10.1161/01.RES.76.4.536

Ogden, C. L., Carroll, M. D., Kit, B. K., & Flegal, K. M. (2014). Prevalence of childhood and adult obesity in the United States, 2011-2012. *The Journal of the American Medical Association*, *311*, 806–814. http://doi.org/10.1001/jama.2014.732

Osawa, M., Masuda, M., Kusano, K. I., & Fujiwara, K. (2002). Evidence for a role of platelet endothelial cell adhesion molecule-1 in endothelial cell mechanosignal transduction: Is it a mechanoresponsive molecule? *Journal of Cell Biology*, *158*(4), 773–785. http://doi.org/10.1083/jcb.200205049

Paguirigan, A., & Beebe, D. J. (2006). Gelatin based microfluidic devices for cell culture. *Lab on a Chip*, *6*(3), 407–13. http://doi.org/10.1039/b517524k

Paguirigan, A. L., & Beebe, D. J. (2007). Protocol for the fabrication of enzymatically crosslinked gelatin microchannels for microfluidic cell culture. *Nature Protocols*, *2*, 1782–1788. http://doi.org/10.1038/nprot.2007.256

Palmer, R. M., Ferrige, a G., & Moncada, S. (1987). Nitric oxide release accounts for the biological activity of endothelium-derived relaxing factor. *Nature*, *327*(6122), 524–526. http://doi.org/10.1038/327524a0

Pearson, J. D. (1999). Endothelial cell function and thrombosis. *Baillière's Best Practice & Research. Clinical Haematology*, *12*(3), 329–41. http://doi.org/10.1053/beha.1999.0028

Pohl, J., Ring, A., Ehehalt, R., Herrmann, T., & Stremmel, W. (2004). New concepts of cellular fatty acid uptake: role of fatty acid transport proteins and of caveolae. *The Proceedings of the Nutrition Society*, *63*(2), 259–262. http://doi.org/10.1079/PNS2004341

Prabhakarpandian, B., Shen, M.-C., Nichols, J. B., Mills, I. R., Sidoryk-Wegrzynowicz, M., Aschner, M., & Pant, K. (2013). SyM-BBB: a microfluidic blood brain barrier model. *Lab on a Chip*. http://doi.org/10.1039/c2lc41208j

Ratner, B. D., Hoffman, A. S., Schoen, F. J., & Lemons, J. E. (2013). *Biomaterials Science - An Introduction to Materials in Medicine* (3rd editio). Elsevier.

Scalia, R. (2013). The microcirculation in adipose tissue inflammation. *Reviews in Endocrine & Metabolic Disorders*, *14*(1), 69–76. http://doi.org/10.1007/s11154-013-9236-x

Schnittler, H. J. (1998). Structural and functional aspects of intercellular junctions in vascular endothelium. *Basic Research in Cardiology*, *93 Suppl 3*, 30–9. Retrieved from http://www.ncbi.nlm.nih.gov/pubmed/9879442

Scott-Drechsel, D., Su, Z., Hunter, K., Li, M., Shandas, R., & Tan, W. (2012). A new flow co-culture system for studying mechanobiology effects of pulse flow waves. *Cytotechnology*, *64*(6), 649–666. http://doi.org/10.1007/s10616-012-9445-2

Shay-Salit, A., Shushy, M., Wolfovitz, E., Yahav, H., Breviario, F., Dejana, E., & Resnick, N. (2002). VEGF receptor 2 and the adherens junction as a mechanical transducer in vascular endothelial cells. *Proceedings of the National Academy of Sciences of the United States of America*, *99*(14), 9462–9467. http://doi.org/10.1073/pnas.142224299

Shi, H., Kokoeva, M. V, Inouye, K., Tzameli, I., Yin, H., & Flier, J. S. (2006). TLR4 links innate immunity and fatty acid – induced insulin resistance. *The Journal of Clinical Investigation*, *116*(11), 3015–3025. http://doi.org/10.1172/JCI28898.TLRs

Song, M. J., Kim, K. H., Yoon, J. M., & Kim, J. B. (2006). Activation of Toll-like receptor 4 is associated with insulin resistance in adipocytes. *Biochemical and Biophysical Research Communications*, *346*(3), 739–745. http://doi.org/10.1016/j.bbrc.2006.05.170

Sotornik, R., Brassard, P., Martin, E., Yale, P., Carpentier, a. C., & Ardilouze, J.-L. (2012). Update on adipose tissue blood flow regulation. *AJP: Endocrinology and Metabolism*, *302*(10), E1157–E1170. http://doi.org/10.1152/ajpendo.00351.2011

Spruell, C., & Baker, A. B. (2013). Analysis of a high-throughput cone-and-plate apparatus for the application of defined spatiotemporal flow to cultured cells. *Biotechnology and Bioengineering*, *110*(6), 1782–1793. http://doi.org/10.1002/bit.24823

Steinberg, H. O., Tarshoby, M., Monestel, R., Hook, G., Cronin, J., Johnson, A., … Baron, A. D. (1997). Elevated Circulating Free Fatty Acid Levels Impair Endothelium Dependent Vasodilation. *Journal of Clinical Investigation*, *100*(5), 1230–1239.

Stremmel, W., Pohl, L., Ring, a, & Herrmann, T. (2001). A new concept of cellular uptake and intracellular trafficking of long-chain fatty acids. *Lipids*, *36*(9), 981–989. http://doi.org/10.1007/s11745-001-0809-2

Summers, L. K. M., Samra, J. S., & Frayn, K. N. (1999). Impaired postprandial tissue regulation of blood flow in insulin resistance: A determinant of cardiovascular risk? *Atherosclerosis*, *147*(1), 11–15. http://doi.org/10.1016/S0021-9150(99)00172-0

Toda, N., & Okamura, T. (2013). Obesity impairs vasodilatation and blood flow increase mediated by endothelial nitric oxide: An overview. *Journal of Clinical Pharmacology*, *53*(12), 1228–1239. http://doi.org/10.1002/jcph.179

Tzima, E., Irani-Tehrani, M., Kiosses, W. B., DeJana, E., Schultz, D. a, Engelhardt, B., … Schwartz, M. a. (2005). A mechanosensory complex that mediates the endothelial cell response to fluid shear stress. *Nature*, *437*(7057), 426–431. http://doi.org/Doi 10.1038/Nature03952

Wang, C., Lu, H., & Schwartz, M. A. (2012). A novel in vitro flow system for changing flow direction on endothelial cells. *Journal of Biomechanics*, *29*(6), 997–1003. http://doi.org/10.1016/j.biotechadv.2011.08.021.Secreted

What is Metabolic Syndrome? (2014).

Yao, R., Zhang, R., Lin, F., & Luan, J. (2013). Biomimetic injectable HUVEC-adipocytes/collagen/alginate microsphere co-cultures for adipose tissue engineering. *Biotechnology and Bioengineering*, *110*(5), 1430–1443. http://doi.org/10.1002/bit.24784

Zervantonakis, I. K., Kothapalli, C. R., Chung, S., Sudo, R., & Kamm, R. D. (2011). Microfluidic devices for studying heterotypic cell-cell interactions and tissue sample cultures under controlled microenvironments. *Biomicrofluidics*, *5*(1), 1–14. http://doi.org/10.1063/1.3553237

Zheng, W., Jiang, B., Wang, D., Zhang, W., Wang, Z., & Jiang, X. (2012). A microfluidic flow-stretch chip for investigating blood vessel biomechanics. *Lab on a Chip*, *12*(18), 3441. http://doi.org/10.1039/c2lc40173h

Ziegler, T., Alexander, R. W., & Nerem, R. M. (1995). An endothelial cell-smooth muscle cell co-culture model for use in the investigation of flow effects on vascular biology. *Annals of Biomedical Engineering*, *23*(3), 216–25. http://doi.org/10.1007/BF02584424

Appendix

Appendix 1: Dimensioned Drawing of prototype carriage plate

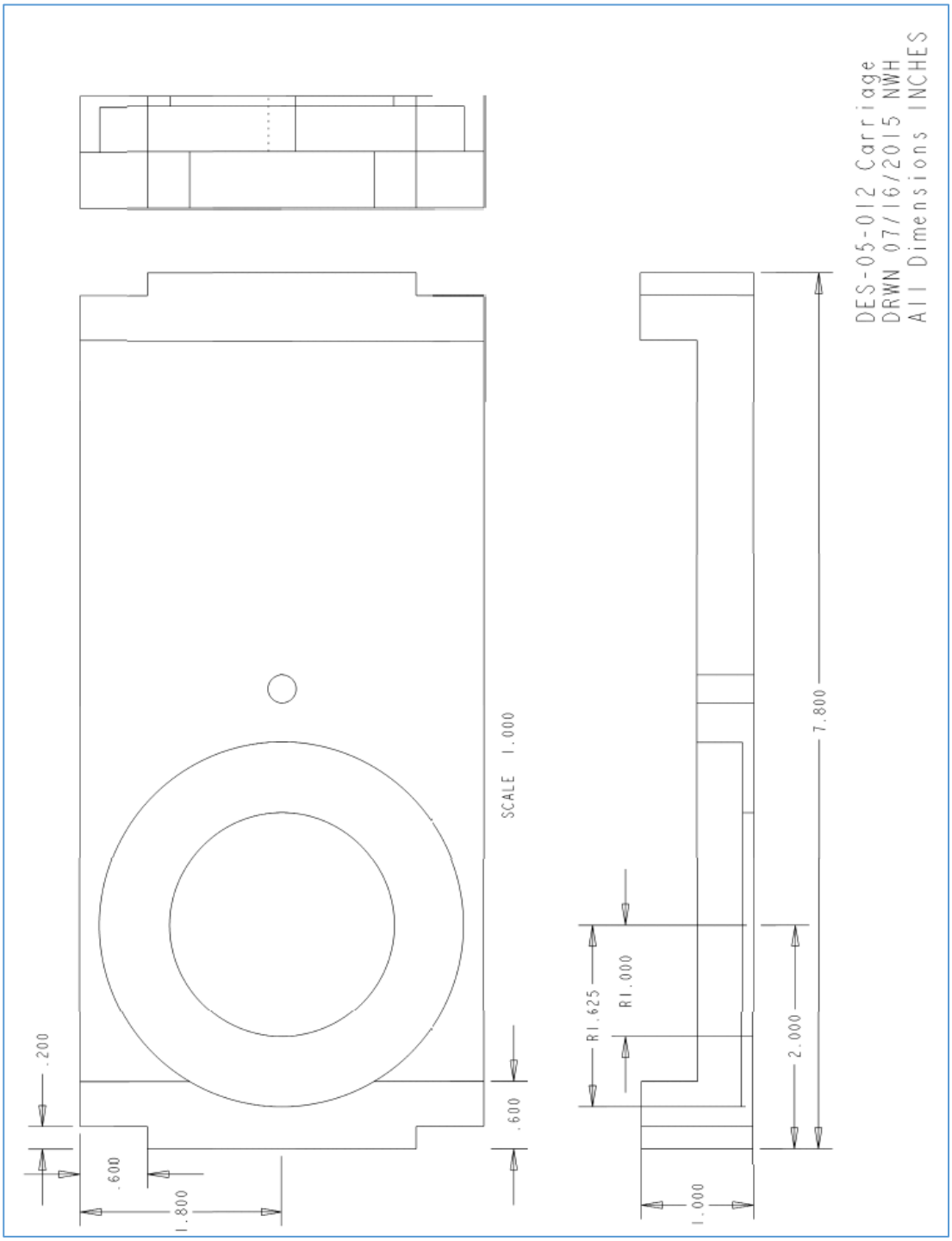

Appendix 2: Dimensioned drawing of prototype cone

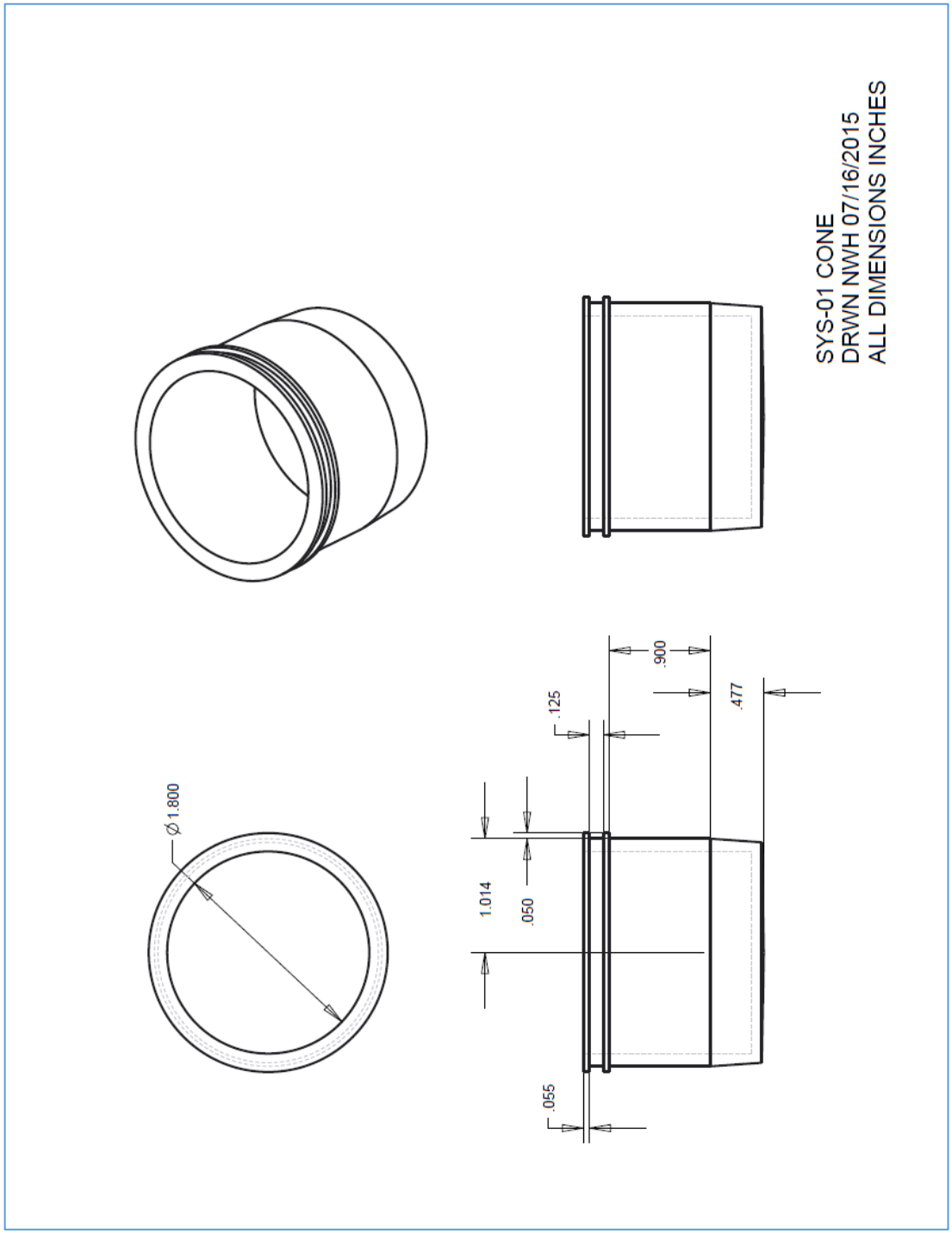

Appendix 3: Arduino Code for control of single stepper motor

```
#include <Stepper.h> // access stepper command library
#define EN1 3 // define pin numbers to names
#define EN2 11
#define DIR1 12
#define DIR2 13

Stepper stepper(200, DIR1, DIR2); // declare motor steps (constant)

unsigned PWM = 0.1;
unsigned RPM = 20;


void setup() {
 pinMode(EN1, OUTPUT); // declare all digital pins as outputs
 pinMode(EN2, OUTPUT);
 pinMode(DIR1, OUTPUT);
 pinMode(DIR2, OUTPUT);

 digitalWrite(EN1,LOW); // delcare all pins as zero value outputs to start
 digitalWrite(EN2,LOW);
 digitalWrite(DIR1,LOW);
 digitalWrite(DIR2,LOW);

 Serial.begin(9600); //from divide by 64 to divide by 8 for faster PWM freq, 7.8 kHz.
TCCR2B = _BV(CS21);


 analogWrite(EN1, PWM);  //enable PWM signal at given pin and value (PWM = 0 to 255)
 analogWrite(EN2, PWM);

 stepper.setSpeed(RPM); // declare RPM value

}

void loop() {

  if (Serial.available()) {
    switch (Serial.read()) {
      case 'q': case 'Q':
      if (PWM > 0, RPM>0) PWM = 0, RPM =0; // press 'q' for motor stop.
      Serial.print('PWM='); Serial.println(PWM);
      analogWrite(EN1,PWM);
      analogWrite(EN2,PWM);
      break;
```

```
    case '1':
    if (PWM <= 250) PWM += 20;
    Serial.print('PWM='); Serial.println(PWM);
    analogWrite(EN1,PWM);
    analogWrite(EN2,PWM);
    break;

    case '2':
    if (PWM >= 10) PWM -= 20;
    Serial.print('PWM='); Serial.println(PWM);
    analogWrite(EN1,PWM);
    analogWrite(EN2,PWM);
    break;

    case '3':
    if (RPM<500) RPM += 20;
    Serial.print('RPM='); Serial.println(RPM);
    stepper.setSpeed(RPM);
    break;

    case '4':
    if (RPM>=20) RPM -= 20;
    Serial.print('RPM='); Serial.println(RPM);
    stepper.setSpeed(RPM);
    break;

    case 'a': //19-21 dynes/cm2
    PWM = 130; // INPUT DESIRED VALUE TO HARDCODE START, STOP
    Serial.print('PWM='); Serial.println(PWM);
    analogWrite(EN1,PWM);
    analogWrite(EN2,PWM);
    RPM = 420;
    Serial.print('RPM='); Serial.println(RPM);
    stepper.setSpeed(RPM);
   }
  }
  stepper.step(1);
}
```

Appendix 4: Arduino program for control of 3 stepper motors

```
#include <Stepper.h> // access stepper command library

#define EN1 3 // define pin numbers to names

#define EN2 11

#define DIR1 12
```

```
#define DIR2 13

#define EN1_2 5
#define EN2_2 10

#define EN1_3 6
#define EN2_3 9 // use digital output pins (~)

Stepper stepper(200, DIR1, DIR2); // declare motor steps (constant)

unsigned PWM = 0.1;
unsigned RPM = 20;



void setup() {
 pinMode(EN1, OUTPUT); // declare all digital pins as outputs
 pinMode(EN2, OUTPUT);
 pinMode(DIR1, OUTPUT);
 pinMode(DIR2, OUTPUT);
 pinMode(EN1_2,OUTPUT);
 pinMode(EN2_2,OUTPUT);
 pinMode(EN1_3,OUTPUT);
 pinMode(EN2_3,OUTPUT);

 digitalWrite(EN1,LOW); // delcare all pins as zero value outputs to start
 digitalWrite(EN2,LOW);
 digitalWrite(EN1_2,LOW);
 digitalWrite(EN2_2,LOW);
 digitalWrite(EN1_3,LOW);
 digitalWrite(EN2_3,LOW);
```

```
 digitalWrite(DIR1,LOW);
 digitalWrite(DIR2,LOW);


 Serial.begin(9600); //from divide by 64 to divide by 8 for faster PWM freq, 7.8 kHz.
TCCR2B = _BV(CS21);


 analogWrite(EN1, PWM);  //enable PWM signal at given pin and value (PWM = 0 to 255)
 analogWrite(EN2, PWM);
 analogWrite(EN1_2,PWM);
 analogWrite(EN2_2,PWM);
 analogWrite(EN1_3,PWM);
 analogWrite(EN2_3,PWM);

 stepper.setSpeed(RPM); // declare RPM value

}

void loop() {

  if (Serial.available()) {
    switch (Serial.read()) {
      case 'q': case 'Q':
      if (PWM > 0, RPM>0) PWM = 0, RPM =0; // press 'q' for motor stop.
      Serial.print('PWM='); Serial.println(PWM);
      analogWrite(EN1,PWM);
      analogWrite(EN2,PWM);
      analogWrite(EN1_2,PWM);
      analogWrite(EN2_2,PWM);
```

```
analogWrite(EN1_3,PWM);
analogWrite(EN2_3,PWM);
break;

case '1':
if (PWM <= 250) PWM += 20;
Serial.print('PWM='); Serial.println(PWM);
analogWrite(EN1,PWM);
analogWrite(EN2,PWM);
analogWrite(EN1_2,PWM);
analogWrite(EN2_2,PWM);
analogWrite(EN1_3,PWM);
analogWrite(EN2_3,PWM);
break;

case '2':
if (PWM >= 10) PWM -= 20;
Serial.print('PWM='); Serial.println(PWM);
analogWrite(EN1,PWM);
analogWrite(EN2,PWM);
analogWrite(EN1_2,PWM);
analogWrite(EN2_2,PWM);
analogWrite(EN1_3,PWM);
analogWrite(EN2_3,PWM);
break;

case '3':
if (RPM<500) RPM += 20;
Serial.print('RPM='); Serial.println(RPM);
stepper.setSpeed(RPM);
```

```
break;

case '4':
if (RPM>=20) RPM -= 20;
Serial.print('RPM='); Serial.println(RPM);
stepper.setSpeed(RPM);
break;

case 'a':
PWM = 100; // INPUT DESIRED VALUE TO HARDCODE START, STOP
Serial.print('PWM='); Serial.println(PWM);
analogWrite(EN1,PWM);
analogWrite(EN2,PWM);
RPM = 100;
Serial.print('RPM='); Serial.println(RPM);
stepper.setSpeed(RPM);

case 's':
PWM = 150;
Serial.print('PWM=');Serial.println(PWM);
analogWrite(EN1,PWM);
analogWrite(EN2,PWM);
analogWrite(EN1_2,PWM);
analogWrite(EN2_2,PWM);
RPM = 200;
Serial.print('RPM=');Serial.println(RPM);
stepper.setSpeed(RPM);
break;
```

```
      case 'd':
      PWM = 150;
      Serial.print('PWM=');Serial.println(PWM);
      analogWrite(EN1,PWM);
      analogWrite(EN2,PWM);
      analogWrite(EN1_2,PWM);
      analogWrite(EN2_2,PWM);
      analogWrite(EN1_3,PWM);
      analogWrite(EN2_3,PWM);
      RPM = 50;
      Serial.print('RPM=');Serial.println(RPM);
      stepper.setSpeed(RPM);
      break;

    }
  }
  stepper.step(1);
}
```

Appendix 5: Dimensioned Drawing of Cone and Plate System Cone

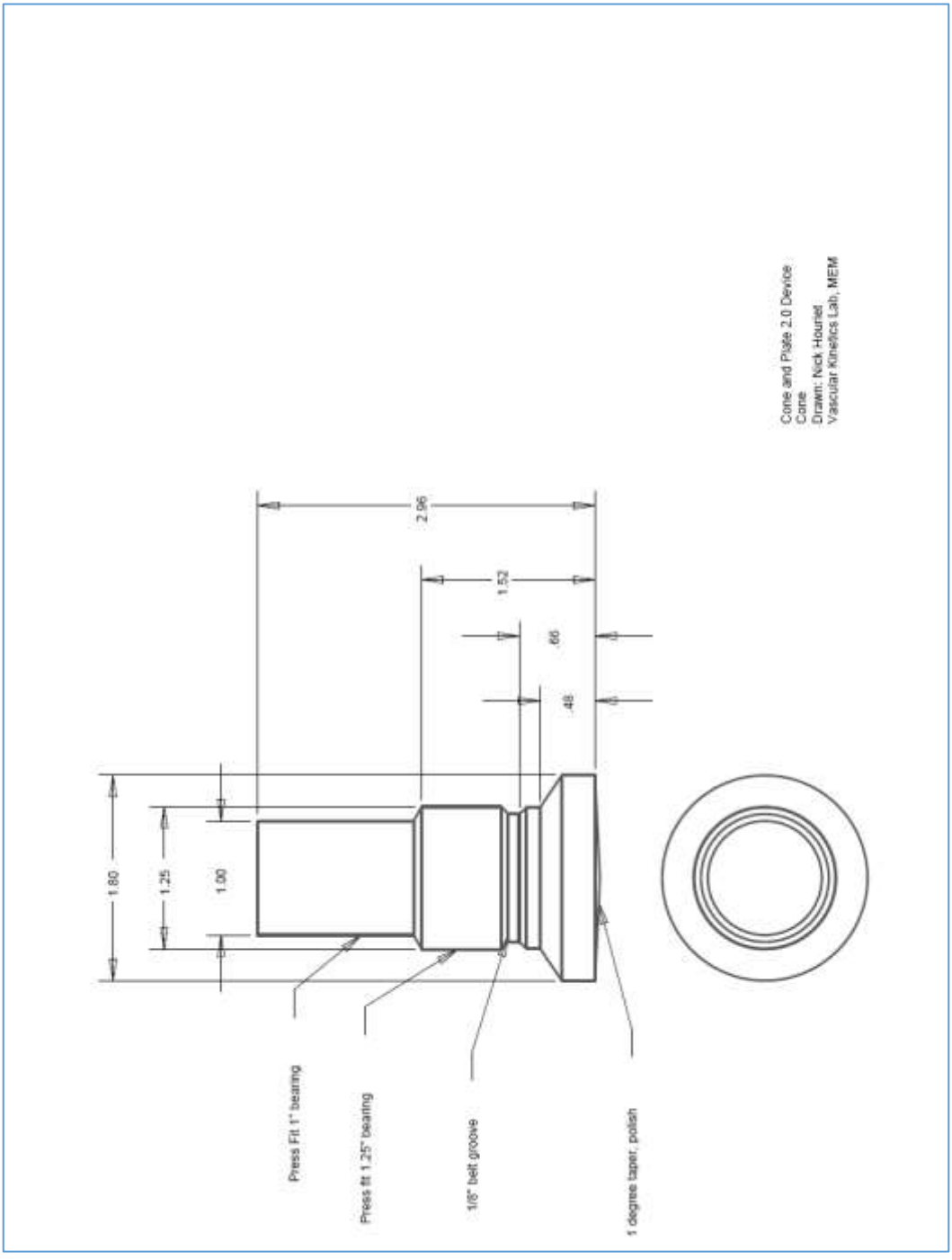

Appendix 6: Dimensioned drawing of Cone and Plate system carriage plate

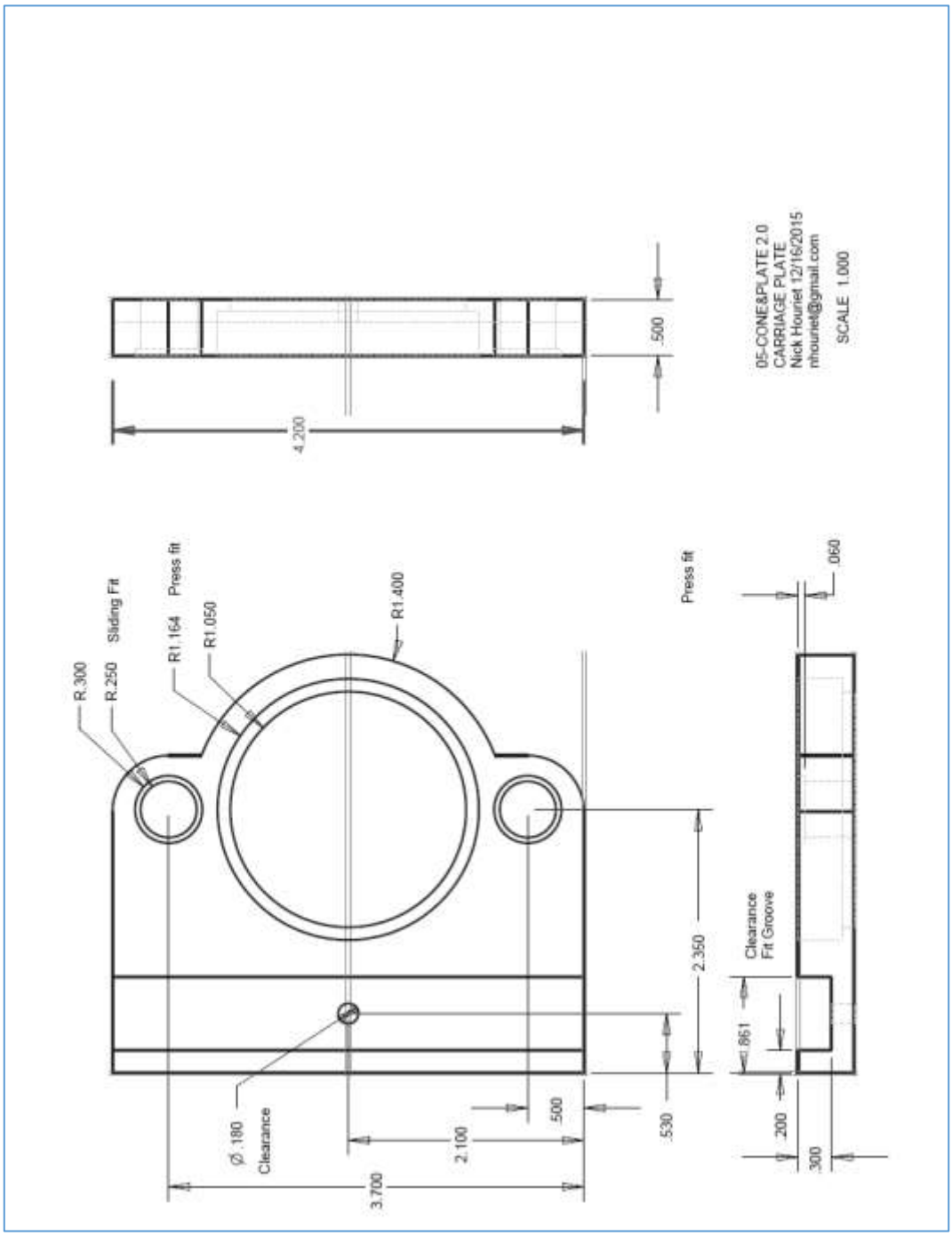

Appendix 7: Dimensioned Drawing of cap plate

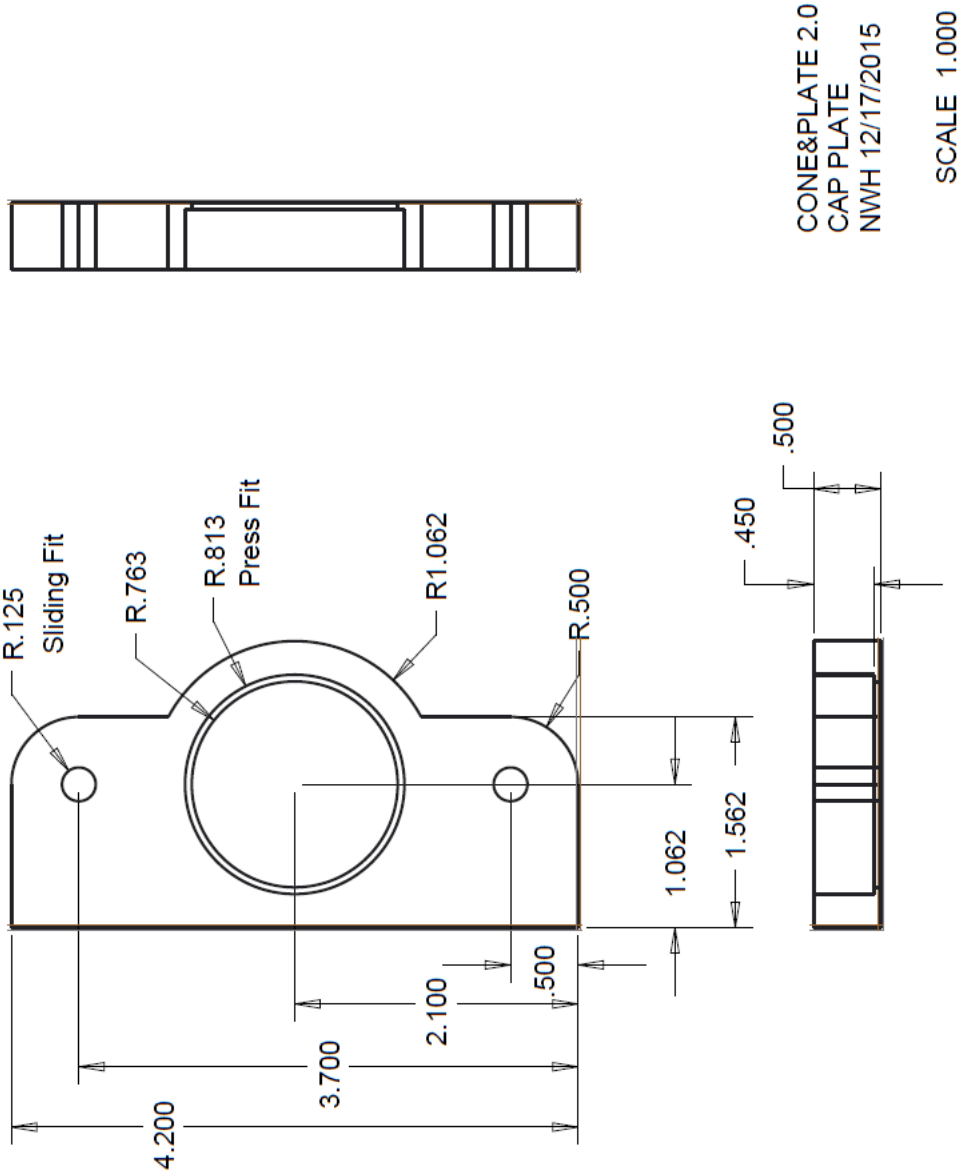
CONE&PLATE 2.0
CAP PLATE
NWH 12/17/2015
SCALE 1.000
R.125
Sliding Fit
R.763
R.813
Press Fit
R1.062
R.500
.500
.450
1.062
1.562
.500
2.100
3.700
4.200

Appendix 8: Dimensioned drawings of Cone and Plate system force sensor plate/ dish cradle

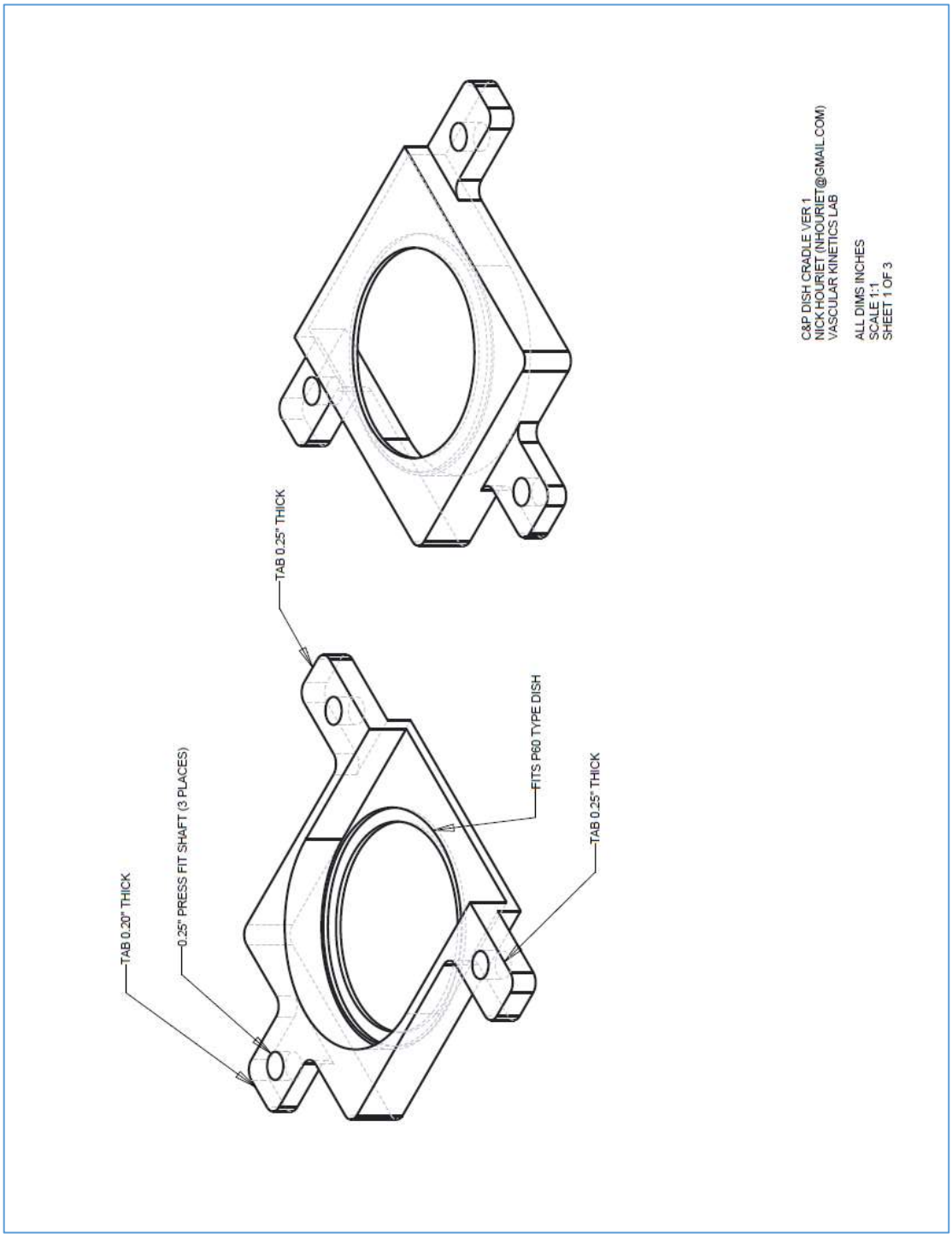

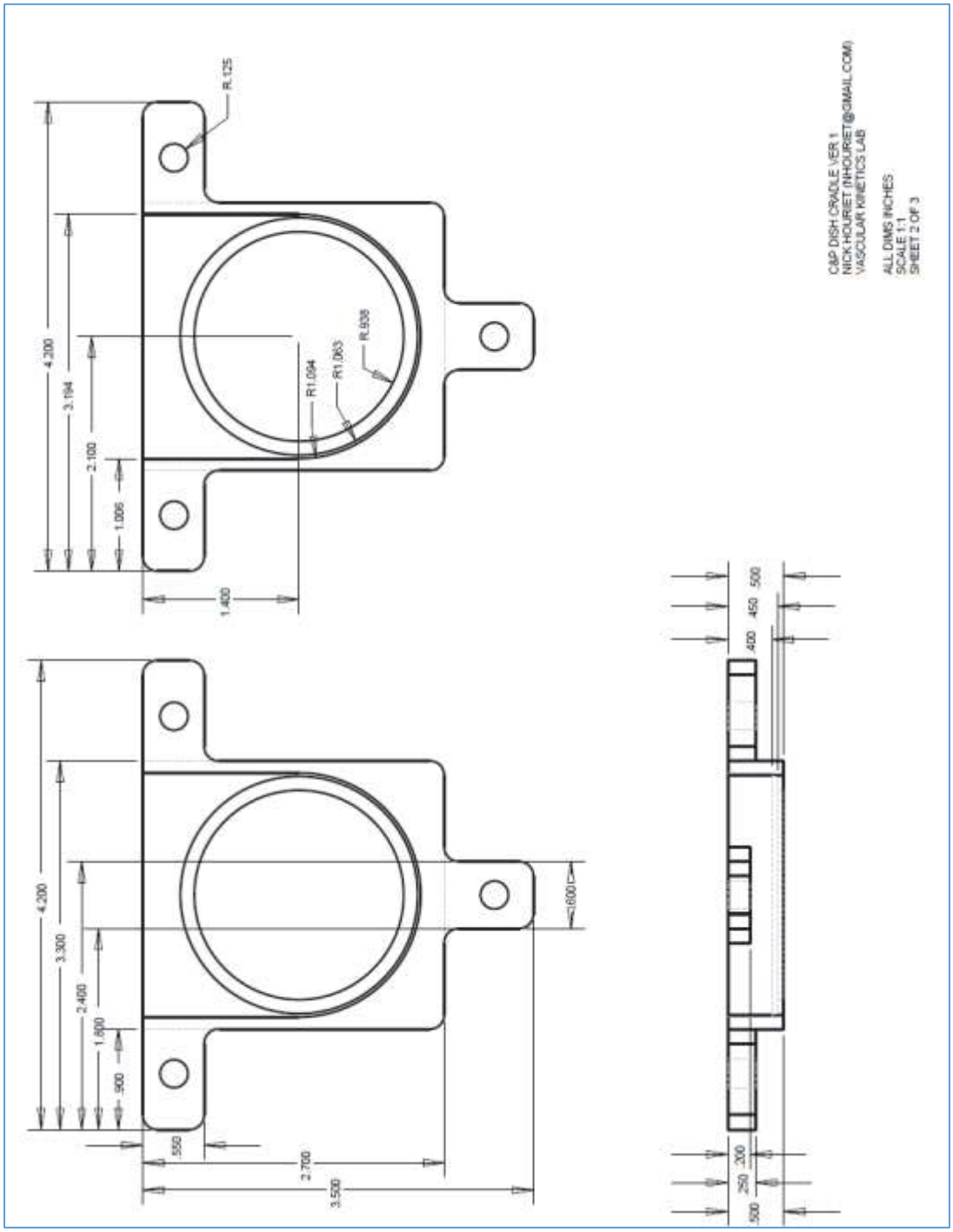
C&P DISH CRADLE VER 1
NICK HOURIET (NHOURIET@GMAIL.COM)
VASCULAR KINETICS LAB
ALL DIMS INCHES
SCALE 1:1
SHEET 2 OF 3
R.125
R.938
R1.063
R1.094
4.200
3.194
2.100
1.006
1.400
4.200
3.300
2.400
1.800
.900
.550
2.700
3.500
.600
.500
.450
.400
.200
.250
.500

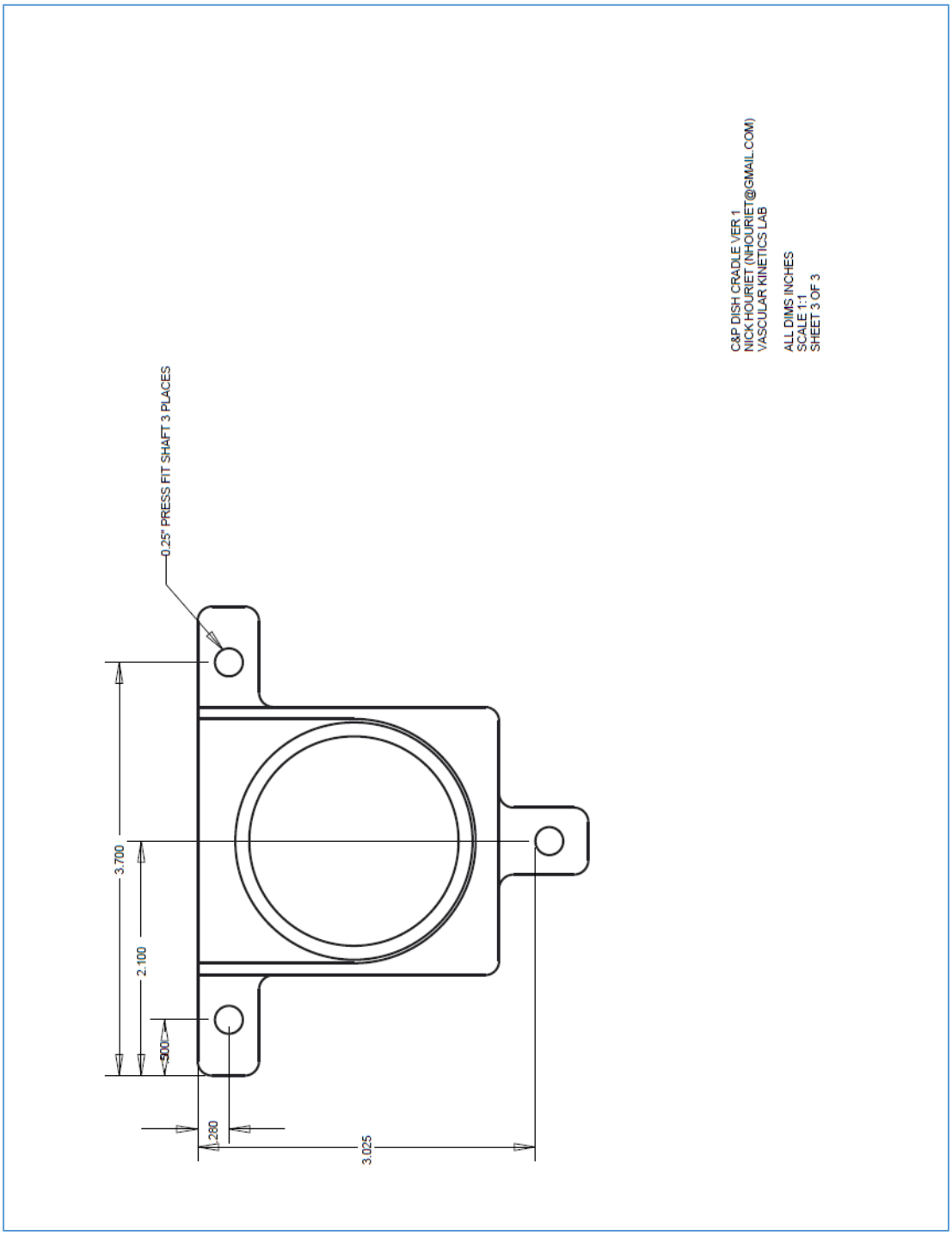
C&P DISH CRADLE VER 1
NICK HOURIET (NHOURIET@GMAIL.COM)
VASCULAR KINETICS LAB
ALL DIMS INCHES
SCALE 1:1
SHEET 3 OF 3
0.25" PRESS FIT SHAFT 3 PLACES
3.700
2.100
.900
.280
3.025

Appendix 9: Dimensioned Drawings of Cone and Plate System baseplate

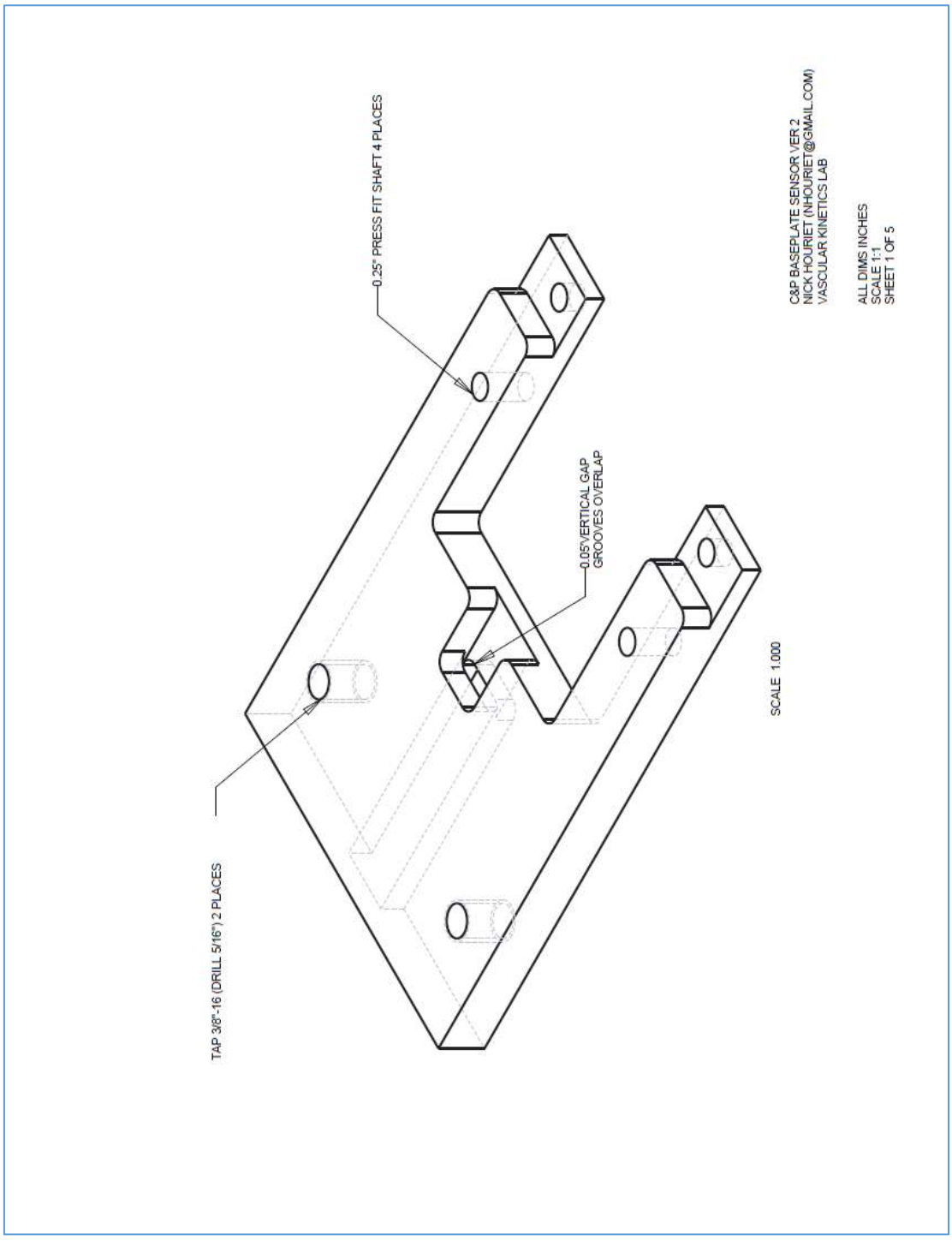

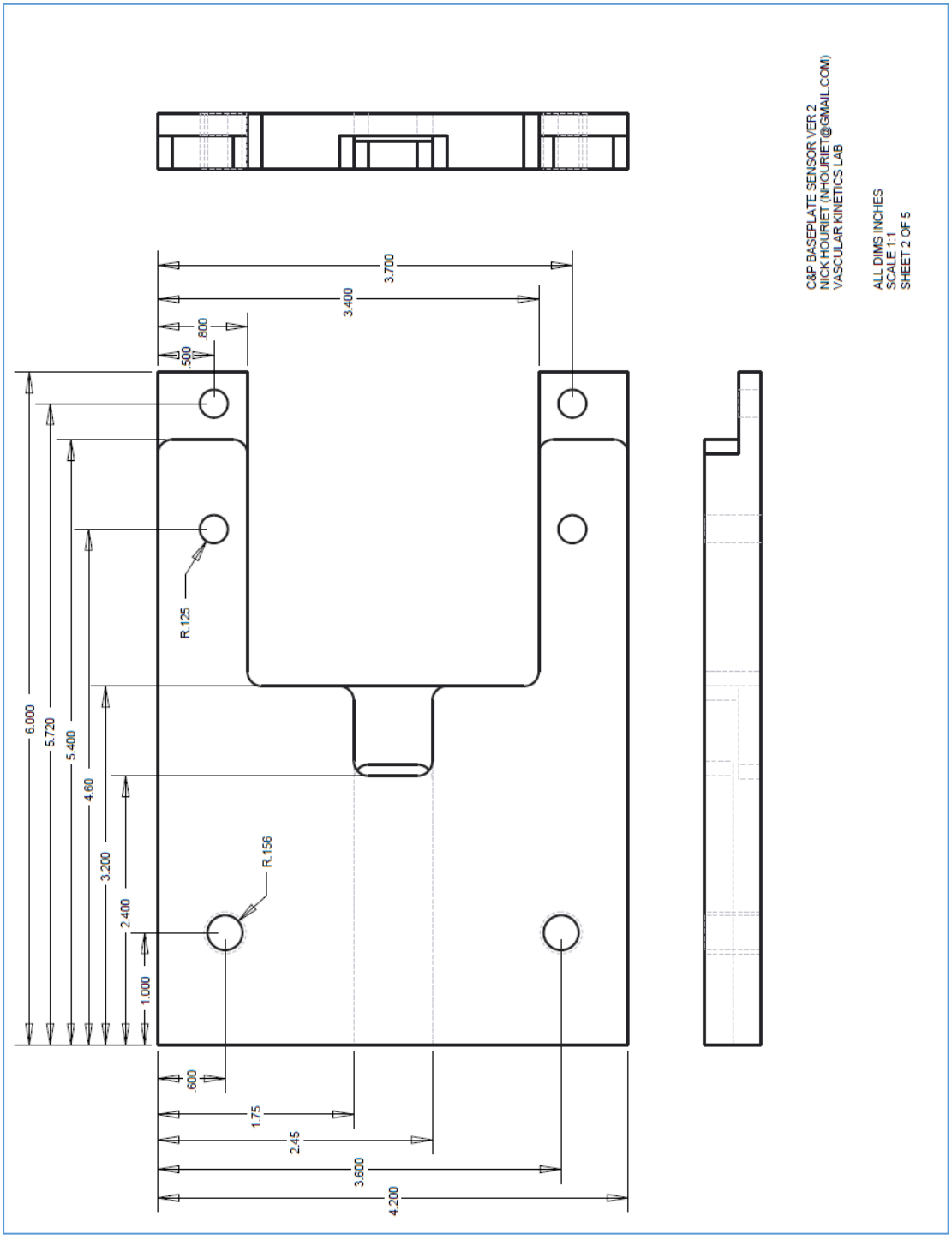
C&P BASEPLATE SENSOR VER 2
NICK HOURIET (NHOURIET@GMAIL.COM)
VASCULAR KINETICS LAB
ALL DIMS INCHES
SCALE 1:1
SHEET 2 OF 5
3.700
3.400
.800
.500
R.125
6.000
5.720
5.400
4.60
3.200
2.400
1.000
R.156
.600
1.75
2.45
3.600
4.200

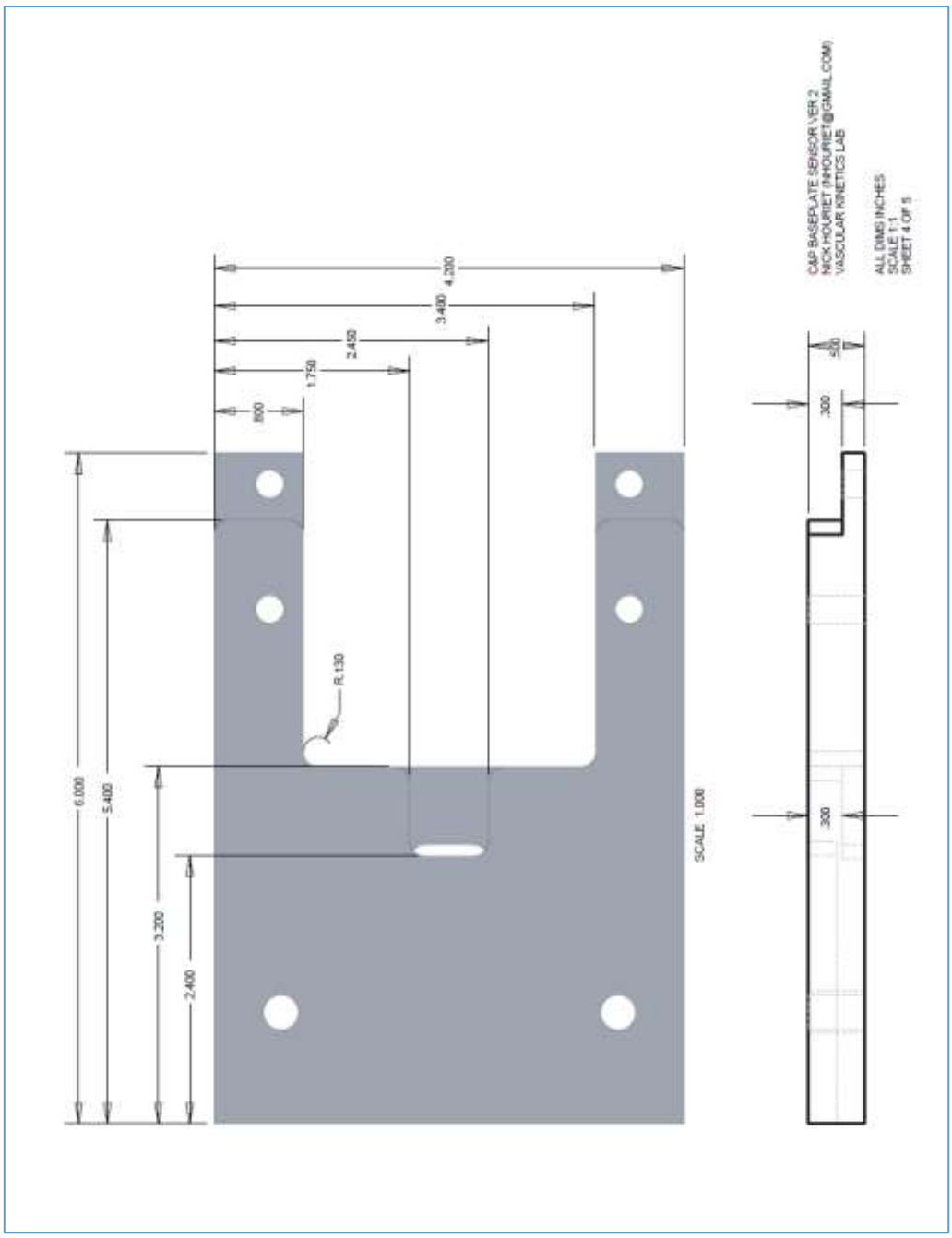
C&P BASEPLATE SENSOR VER 2
NICK HOURIET (NHOURIET@GMAIL.COM)
VASCULAR KINETICS LAB
ALL DIMS INCHES
SCALE 1:1
SHEET 4 OF 5
4.200
3.400
2.450
1.750
800
R.130
6.000
5.400
3.200
2.400
SCALE 1.000
300
300